UNIVERSITÀ DEGLI STUDI DI ROMA "LA SAPIENZA"

FACOLTÀ DI SCIENZE MATEMATICHE, FISICHE E NATURALI

# Neutrino production of charmed particles in the CHORUS experiment

Francesca Romana Spada

PH.D. IN PHYSICS
DOTTORATO DI RICERCA IN FISICA
XIV Ciclo – AA. AA. 1998-2001

| Supervisor: | Ph.D. Coordinator: |
|---|---|
| *Prof. Pier Ferruccio Loverre* | *Prof. Guido Martinelli* |

# Table of Contents

# List of Figures

# List of Tables

# Introduction

The CHORUS experiment was originally designed to study $\nu_\mu \longrightarrow \nu_\tau$ oscillations, a phenomenon that can take place only if neutrino rest mass is non zero. To observe oscillations then means to prove that neutrinos are massive particles, which is a feature predicted by many extensions of the Standard Model of electroweak interactions.

The method that CHORUS uses to detect the appearance of a $\nu_\tau$ created in the oscillation of a $\nu_\mu$ of the beam, is the direct observation of the charged current interaction $\nu_\tau\, N \rightarrow \tau^-\, X$, an the subsequent $\tau$ lepton decay after a short flight. To do this, CHORUS uses 800 Kg of nuclear emulsions as a target that also acts as a tracker, providing one micron of spatial resolution. Nuclear emulsions thus allow the detection of the 1 mm long track left by the $\tau$ lepton, together with that of the charged decay product, that can be a muon or a hadron. The setup of the experiment is *hybrid*: kinematic reconstruction of the event is given by electronic detectors following the target, that provide track reconstruction, and measurement of momenta and energies of the particles produced.

The CHORUS detector is also suitable for the study of neutrino production of hadrons containing a charm quark, because charmed hadrons have lifetimes similar to that of the $\tau$, and can then be detected with the same procedure used for the latter.

The study of charm production in neutrino interactions is relevant for the determination of several quantities related to the quark physics, such as the element $V_{cd}$ of the Cabibbo-Kobayashi-Maskawa matrix, the charm quark mass, the strange content of the sea, the nucleon structure functions, the parameters entering in the quark fragmentation.

To charm studies is also related the subject of this thesis.

Charm production by neutrino has been extensively investigated by experiments belonging to two groups characterized by different features: counter experiments, in which the detectors, roughly, consist in large, massive tracking calorimeters, and experiments in which the target is composed of nuclear emulsion, as in CHORUS. Also bubble chamber experiments have observed charm production in neutrino interactions.

Because of the small neutrino interaction cross section, a high statistics can only be obtained in counter experiments, which are characterized by masses up to $10^3$ tons. They can detect "dimuon" events, i.e. events in which the charmed hadron decays semileptonically giving a $\mu^+$ so that the final state contains two opposite charge muons (the negative one coming from the primary vertex). Thus only one decay mode can be studied, and the information on the kind of hadron actually produced is rather poor. Moreover, a large background due to decays of non charmed hadrons such as pions and kaons is present.

Dimuon experiments usually give their result in terms of the dimuon production cross section: to extract from this the total charm production cross section, the relative fractions of charmed hadrons (i.e. $D^0$, $D^+$, $D_s^+$ and $\Lambda_c$) produced in the neutrino interaction must be known, since different $c$ hadrons have different branching ratios into muon. But if at present the quark fragmentation is well modelized separately for each hadron, the theoretical description of the relative hadron fractions into which the quark hadronizes is not as reliable. In fact, dimuon experiments all use one among the available standard fragmentation function parametrizations, but for the relative hadron fractions, assume measured quantities.

The best measurement presently available comes from E531, an emulsion experiment which had, as CHORUS, a hybrid setup, and was able to identify directly the kind of charmed hadron produced in the interaction by its invariant mass. The fractions measured by E531 with an error of about 10% in 1987 are adopted by the counter experiment in their simulations and are used to extract the fundamental parameters.

Generally, emulsion experiments are able to observe directly the charmed hadron decay, whatever be the decay channel, because of their very high spatial resoution. This is true also for CHORUS, and in this thesis a new measurement of the fractions of charmed hadrons in neutrino interactions will be presented, which was done using the CHORUS events.

The handicap of emulsion experiments with respect to counter experiments has always been the fact that the statistics is much lower. The main reason for this is the huge scanning work that would be needed: in fact, the traditional analysis of emulsions is performed manually by an operator at a microscope, who searches for dark grains having dimensions of the order of the micron, in a cube millimeter volume in order to identify the tracks. CHORUS was the first experiment that developed a fully automatic scanning system based on a video image processor interfaced to the microscope through a CCD camera, called Track Selector. During the years, the scanning speed was increased of a factor $10^4$, and we are now at the fourth automatic scanning hardware generation.

Then, as mentioned before, CHORUS has characteristics suitable to study charm physics. The step forward is that it has the chance to become the first emulsion high statistics experiment for neutrino charm physics, thanks to its large mass (the emulsion target is one order of magnitude larger than previous emulsion experiments), and to the surprising increase of fast automatic scanning capability of the experiment with time.

CHORUS has just finished a first phase of oscillation analysis, in which several improved versions of the Track Selector were used. The technique consisted in the selection of a track of the event (the muon in the case of charged current interactions, one or more hadrons for neutral current interactions), which was followed from the electronic detector up to the emulsion target, and then in emulsion by the Track Selector itself, until the vertex was located, and at that point the decay search started. If the event was supposed to contain a kink, only at that point was manually checked by a human operator to confirm the decay.

A second phase of analysis has then started, and is now in progress, which will be characterized by a new method of fast emulsion scanning and decay search that was possible to develope thanks to the high scanning power reached. The new method is called *netscan* and consists in the automatic scanning of a whole 15 $\text{mm}^3$ volume of emulsion around the located vertex: all track segments in this volume are picked up. This allows to automatically get the complete information on the interaction vertex (and on the decay vertex, if present). Of course, this is valid both for $\tau$ and for charm decays.

Netscan is already running, and the software for event reconstruction in continuous developement. Also work is in progress on the software which has to select, among netscan events, those containing a charm decay. Some selections were already developed and applied to a part of the currently available netscan sample. This allowed to reconstruct a few hundreds of charm events. These make up the sample that was used for the analysis described here.

Several analyses are also in progress, such as the measurement of the $D^0$ production rate, the measurement of charged charmed hadron fractions described here, and the measurement of the associated charm production both in neutral current (where a measurement was already performed by E531) and in charged current, where no previous measurement exists.

The work that will be described in this thesis consisted in the study of the netscan technique and in the interpretation of the measurements coming from the new scanning method, and then in the preliminary measurement of charged "stable" charmed hadron fractions produced in neutrino charged current interactions. With "stable" we mean the charmed hadrons that undergo weak decay with $c\tau \sim 1$ mm, then detectable in emulsion, i.e. $D^+$, $D_s^+$ and $\Lambda_c$.

The available statistics consists in 167 confirmed charged decays, i.e. twice the statistics of E531, which collected a sample of 121 charmed particles out of 3,800 neutrino interactions, 57 being neutrals. With respect to CHORUS, the E531 detector had the advantage to be capable to measure the charmed hadron momentum (while this was not possible in CHORUS for several reasons that will be explained in the following), thus identifiying the decaying hadrons event by event. In our measurement, the determination of the fractions is instead obtained on a statistical basis, and in this respect our sample is actually not so large. However, we expect to have, at the end of phase 2, more than 10 times the current statistics.

The event by event identification of charmed hadrons was not possible because of the scarce efficiency and resolution on the hadron momentum measured by the hadron spectrometer. A dedicated study was done, which is discussed in detail in chapter 3, and it was concluded that the available momentum measurement was not useful for this analysis (while it is used in the oscillation search).

The thesis is then structured as follows:

chapter 1 discusses the theoretical framework for charm production studies, i.e. the neutrino interactions with matter, via deep inelastic scattering and other minor production mechanisms, and some aspects of the underlying quark physics, such as how a charm quark can be produced in a neutrino scattering and how, from a bare quark, we get to observe hadrons. Then the current experimental status is reported;

chapter 2 describes the CHORUS electronic detector and its emulsion target. Also the study of the resolution on the momentum of hadrons measured by the hadron spectrometer, mentioned above, is presented here;

chapter 3 contains the description of the netscan method that allows the experiment to extract a much larger amount of informations from its emulsion target/detector than in the past;

chapter 4 gives the details of the analysis which is the main subject of this thesis: how the charm data sample used was built up, the Monte Carlo simulation and finally the fit of the production fractions are described. The result is then compared to the exiting one.

Then the conclusions follow.

## Chapter 1

# Neutrino interactions and charm production

Neutrino made its first appearance on the particle physics scene when, in 1930, Wolfgang Pauli proposed his solution to the spectrum problem in nuclear $\beta$ decay. The puzzle had arised by the observation (Chadwick, 1914) of the fact that $\beta$ rays show a continuous spectrum: the emitted electrons do not have a fixed energy and the observed decay products do not emerge back to back as should be in a two body decay. It then seemed that the process violated conservation laws.

In a letter addressed to the "Radioactive Ladies and Gentlemen" participating to a congress in Tübingen, Pauli claimed that the missing energy and angular momentum could be carried by a non observed, neutral particle of spin 1/2.

Actually, the newcomer owes its name to Enrico Fermi, who in 1933 named the new particle "neutrino" and formulated a theory for the simultaneous emission of an electron and a neutrino by a nucleus [1, 2], thus initiating the description of weak interactions. Fermi and Pauli were awarded the Nobel prize in 1938 and 1945 respectively.

It was soon evident that neutrino experimental detection was a difficult task to achieve, since these particles could travel several light years in ordinary matter before interacting with it: the inverse $\beta$ decay cross section amounted to $10^{-43}$ cm$^2$ for an antineutrino of a few MeV (Bethe and Peierls, 1934). The first direct evidence of neutrino existence came only in 1955 from an experiment performed by Reines and Cowan at a nuclear reactor in Savannah River (South Carolina), which used a target composed by a solution of 40 Kg of $CdCl_2$ in 200 Kg of water, and could observe the inverse $\beta$ decay reaction initiated by antineutrinos [3].

Since these times, a huge amount of work was spent to try and work out the properties of neutrinos. The discovery of pion (Powell, 1947) led to the observation that $\beta$ decay is not the only source of neutrinos: these are produced in the pion weak decay as well. After several years, in 1962, Lederman, Steinberger and Schwartz [4] demonstrated that the neutrino produced in pion decay is different from the one produced in $\beta$ decay: the former interacts to create a muon, while the latter gives an electron. Neutrinos were then distinguished in $\nu_e$ and $\nu_\mu$. Later, with the discovery of the $\tau$ lepton in 1975 [5], the existence of a third neutrino was inferred (and the $\nu_\tau$ was actually observed in very recent times by the Donut experiment at Fermilab [6]).

From the theoretical point of view, all the so far observed neutrino interactions are very accurately described within the Standard Model frame. Nevertheless, not all the questions arised before its final formulation found an answer in this context. For example, in the minimal Standard Model neutrinos are described as massless particles, but it must be stressed that there is no fundamental principle stating that neutrinos must have vanishing mass, and in fact many extensions of the Standard Model predict massive neutrinos. Also cosmological open questions, such as the dark matter existence, strengthen this hypothesis. Unfortunately, direct measurements only allowed till now to put upper limits on the masses, and have little hope to give much more stringent results.

In 1957 Bruno Pontecorvo suggested an indirect method to decide once and forever on the subject: if the mass term is present, "mass eigenstates" can be defined, of which the electroweak eigenstates will be a superposition. This gives rise to the phenomenon of oscillations: neutrinos have a non zero probability to change flavour some time after their creation. If oscillations are observed, one can indirectly deduce that neutrinos are massive. Since then, many experiments aiming to detect oscillations were realized, and some very soon observed a signal. Even if the matter is still somehow controversed, the scientific community seems inclined to believe the existence of neutrino oscillations, mostly in the light of recent results coming from the Super Kamiomande [7] and SNO [8] experiments.

Even though the Standard Model is generally believed to fully describe neutrino interactions, the extreme smallness of cross sections makes it quite hard to get large statistics, high precision measurements, and several processes are indeed unmeasured yet. The theoretical predictions of cross sections of processes involving hadrons are made (at least at high energies) in the framework of the so called Quark Parton Model. A set of experiments [9, 10, 11] held at the Stanford Linear Accelerator during the sixties, with a 20 GeV electron beam on various targets, demonstrated that the scattering actually happened on pointlike objects contained in the nuclei, that were called partons. Due to the very high energy, electrons had reached the inner structure of the hadrons: reactions of this kind are called "deep inelastic". The partons were then identified with the quarks introduced by Gell-Mann and Zweig [12, 13] to explain the hadronic spectroscopy.

The Parton Model is of interest here since charm production in neutrino deep inelastic interactions can be described in this framework too. The following sections give a brief description of the main features of neutrino interactions, with a particular attention to the seminclusive production of a charm quark in deep inelastic scattering. Then the fragmentation process (i.e., how quarks dress themselves with other quarks to form hadrons) is described. After that, other mechanisms of charm production that exist on top of deep inelastic scattering are recalled. Finally, our present experimental knowledge of some aspects of charm physics is reviewd.

## 1.1 Neutrino description in the Standard Model

In the 60's Glashow, Weinberg and Salam started a theoretical work pointing to the description of weak and electromagnetic interactions in a unified way [14, 15, 16]. They independently succeded to reach their aim, and in 1979 shared the Nobel prize. The result of their work was then known as the Standard Model of electroweak interactions.

### 1.1.1 Basic concepts

The Standard Model is a gauge theory with matter fermions, based on the local gauge group $SU(2)_L \times U(1)_Y$ generated by weak isospin and weak hypercharge, in which (a subset of) gauge bosons and matter fermions acquire mass through the mechanism of spontaneous breaking of the local gauge symmetry. This is induced by the nonvanishing vacuum expectation value of scalar fields (Higgs mechanism) [17, 18].

To completely describe the model we have to specify the representation of the gauge group on the fermions (lepton and quarks) and on the scalars (Higgs particles). The left-handed components of each generation of leptons and quarks are doublets under $SU(2)_L$, while right-handed components are singlets (colour indices are omitted):

$$\begin{array}{ccccc}
\begin{pmatrix}\nu_e\\ e^-\end{pmatrix}_L & \begin{pmatrix}u\\ d'\end{pmatrix}_L & e^-_R & u_R & d'_R\\
\begin{pmatrix}\nu_\mu\\ \mu^-\end{pmatrix}_L & \begin{pmatrix}c\\ s'\end{pmatrix}_L & \mu^-_R & c_R & s'_R\\
\begin{pmatrix}\nu_\tau\\ \tau^-\end{pmatrix}_L & \begin{pmatrix}t\\ b'\end{pmatrix}_L & \tau^-_R & t_R & b'_R
\end{array}$$

The prime denotes the fact that quarks eigenstates of weak interactions are in principle not equal to mass eigenstates $d$, $s$, $b$, the two groups being related by the unitary Cabibbo-Kobayashi-Maskawa mixing matrix [19, 20]:

$$\begin{pmatrix}d'\\ s'\\ b'\end{pmatrix} = \begin{pmatrix}V_{ud} & V_{us} & V_{ub}\\ V_{cd} & V_{cs} & V_{cb}\\ V_{td} & V_{ts} & V_{tb}\end{pmatrix}\begin{pmatrix}d\\ s\\ b\end{pmatrix}$$

This is a consequence of the quark mass generation through the Higgs mechanism, and does not apply to leptons as far as right-handed neutrinos are omitted.

The fact that the CKM matrix is different from the identity is responsible for the flavour changing terms in charged weak currents (e.g. inducing flavour changing hadronic $\beta$ decays as $u \to s\, e^+\, \nu_e$) and for direct CP violation (as in $K_L \to \pi\,\pi$).

The $U(1)_Y$ representations are fixed by their hypercharge $Y$, which is related to the electric charge through $Q = T_3 + Y$, where $T_3$ is the third generator of $SU(2)_L$. This completely defines the hypercharges: the left-handed lepton doublets have $Y = -1/2$ and the right-handed lepton singlets have $Y = -1$, while quark doublets have $Y = 1/6$, and right-handed up and down quarks have $Y = 2/3$ and $Y = -1/3$ respectively. Right-handed neutrinos were not introduced since they do not participate in weak interactions: they would be $SU(2)_L \times U(1)_Y$ singlets, thus without coupling to the gauge bosons. Table 1.1 summarizes the main features of leptons and quarks of the Standard Model.

Finally, the Higgs scalars must be introduced. The minimal possibility is that of a scalar $SU(2)_L$ doublet, $\Phi = (\Phi^+ \quad \Phi^0)$ with $Y = 1/2$, with a symmetry breaking potential

$$V(\Phi) = \mu^2\Phi^\dagger\Phi + \lambda(\Phi^\dagger\Phi)^2 \qquad \lambda > 0,\ \mu^2 < 0 \tag{1.1}$$

| | | Leptons | | | | | |
|---|---|---|---|---|---|---|---|
| | | $\boldsymbol{\nu_e}$ | $\boldsymbol{e^-}$ | $\boldsymbol{\nu_\mu}$ | $\boldsymbol{\mu^-}$ | $\boldsymbol{\nu_\tau}$ | $\boldsymbol{\tau^-}$ |
| Mass [MeV] | | $< 15 \cdot 10^{-3}$ | $0.511$ | $< 0.17$ | $105.7$ | $< 18.2$ | $1.8 \cdot 10^3$ |
| Charge | | $0$ | $-1$ | $0$ | $-1$ | $0$ | $-1$ |
| Hypercharge | *L* doublets | $-\frac{1}{2}$ | $-\frac{1}{2}$ | $-\frac{1}{2}$ | $-\frac{1}{2}$ | $-\frac{1}{2}$ | $-\frac{1}{2}$ |
| | *R* singlets | | $-1$ | | $-1$ | | $-1$ |

| | | Quarks | | | | | |
|---|---|---|---|---|---|---|---|
| | | $\boldsymbol{u}$ | $\boldsymbol{d}$ | $\boldsymbol{c}$ | $\boldsymbol{s}$ | $\boldsymbol{t}$ | $\boldsymbol{b}$ |
| Mass [MeV] | | $1.5 \div 5$ | $3 \div 9$ | $(1.1 \div 1.4) \cdot 10^3$ | $60 \div 170$ | $174 \cdot 10^3$ | $(4.1 \div 4.4) \cdot 10^3$ |
| Charge | | $+\frac{2}{3}$ | $-\frac{1}{3}$ | $+\frac{2}{3}$ | $-\frac{1}{3}$ | $+\frac{2}{3}$ | $-\frac{1}{3}$ |
| Hypercharge | *L* doublets | $+\frac{1}{6}$ | $+\frac{1}{6}$ | $+\frac{1}{6}$ | $+\frac{1}{6}$ | $+\frac{1}{6}$ | $+\frac{1}{6}$ |
| | *R* singlets | $+\frac{2}{3}$ | $-\frac{1}{3}$ | $+\frac{2}{3}$ | $-\frac{1}{3}$ | $+\frac{2}{3}$ | $-\frac{1}{3}$ |

Table 1.1 – Standard Model leptons and quarks. Masses are taken from [21].

which in the *unitary gauge* takes the form

$$\Phi = \begin{pmatrix} 0 \\ v + \sigma(x)/\sqrt{2} \end{pmatrix} \qquad v = \sqrt{\frac{-\mu^2}{2\lambda}} \tag{1.2}$$

where $\sigma$ is a scalar neutral field (of the Higgs boson) of vanishing vacuum expectation value.

### 1.1.2 Neutrino mass terms

In the case just considered in which only a Higgs doublet is present, the most general lepton-Higgs Yukawa term in the electroweak lagrangian is

$$\mathcal{L}_{HL} = \sum_{l=e,\mu,\tau} g_l \, \bar{L}_l \, l_R \, \Phi + \text{h.c.} \tag{1.3}$$

where $L_l$ is the leptonic doublet, and through spontaneous symmetry breaking this gives rise to Dirac mass terms for charged leptons alone. Insisting not to introduce right-handed neutrinos, with just one Higgs doublet there is no possibility of gauge invariant mass terms for neutrinos, which then remain exactly massless. If instead right-handed *sterile* neutrinos are introduced, the non diagonal Yukawa coupling can be written:

$$\mathcal{L}_{H\nu} = \sum_{l,l'} g^{\nu}_{ll'} \, \bar{L}_l \, \hat{\Phi} \, \nu^R_{l'} + \text{h.c.} \tag{1.4}$$

where $\hat{\Phi} = i\tau^2 \, \Phi^\dagger$ is the charge conjugate of $\Phi$ (which has $Y = -1/2$). Thus, diagonalizing the matrix $vg^\nu$ after spontaneous symmetry breaking, through appropriate unitary transformations on neutrino generations we get a Dirac mass term:

$$\mathcal{L}^{\text{mass}}_{\nu} = \sum_{k=1}^{3} m_k \, \bar{\nu}^L_k \, \nu^R_k + \text{h.c.} \tag{1.5}$$

where neutrino mass eigenstates $\nu^L_k$, $\nu^R_k$, $k = 1, 2, 3$, and weak interaction eigenstates $\nu^L_l$, $\nu^R_l$, $l = e, \mu, \tau$, are related by unitary matrices. Then if the first of these matrices (i.e. the one which transforms $\nu^L_l$ in $\nu^L_k$) is different from the identity - and there is no physical principle which can exclude that this is really the case - we have neutrino flavour mixing, and hence lepton flavour conservation is broken, and only the total lepton number is conserved.

There is also the possibility that neutrinos are Majorana fermions, i.e. they coincide with their own antiparticles. In this case, also the total lepton number is not conserved.

This opens up the possibility of writing mass terms using only the left-handed neutrino field $\nu_l^L$ and its charge conjugate. However, to be able to derive such a term from spontaneous symmetry breaking, it is necessary to introduce a triplet of Higgs fields [22], and experimental results seem to rule out this possibility.

### 1.1.3 Neutrinos and quarks

For what concerns quark mass terms, the situation is completely analogous to the one just described for leptons, apart from the fact that down type right-handed quarks are there from the beginning and their mixing matrix is not the identity, and quarks, being charged, cannot be Majorana particles. Here, we are mostly concerned with neutrino interactions with hadrons, in which a charm quark is produced. In the Standard Model, neutrinos interact with quarks through the coupling of leptonic and hadronic currents to the gauge bosons:

$$\mathcal{L}_\nu^{\text{int}} = \frac{g}{\sqrt{2}}\left(W_\mu J^\mu\right) + \text{h.c.} + \frac{g}{\cos\theta_W} J^{3\mu} Z_\mu \tag{1.6}$$

where, for instance,

$$J^\mu = \sum_{l=e,\mu,\tau} \bar{l}_L \gamma^\mu \nu_{Ll} + \sum_{\substack{f=u,c,t \\ f'=d',s',b'}} \bar{f}_L \gamma^\mu f'_L \tag{1.7}$$

is the sum of leptonic and hadronic charged currents, and where $W_\mu$ and $Z_\mu$ are the gauge fields describing charged $W^\pm$ and neutral $Z^0$ bosons respectively. So, typical diagrams of interactions of neutrinos with quarks are of the type shown in figure 1.1. The first one is said to be a *charged current* (CC) interaction, while the second a *neutral current* (NC) one. It is worth noticing that, since the $d'$, $s'$, $b'$ quarks enter in the charged currents (but not in the neutral ones, where instead the unprimed quarks $d, s, b$ appear, due to the unitarity of the CKM matrix), CC interaction cross sections generally depend on the elements of the mixing matrix.

However, quarks have never been observed to propagate freely, i.e. they never appear in initial and final states of reactions. Quarks are confined in *white* (i.e., colour neutral) hadrons, like protons, neutrons and so on. To be able to compare results of calculations with results of experiments, one then has to use hadrons as initial and final states. Since the basic dynamics is instead described in terms of quark fields, this poses a twofold problem: on one side, to describe how hadrons in initial states, such as nucleons, are composed in terms of quarks, and their interactions; on the other hand, to describe how

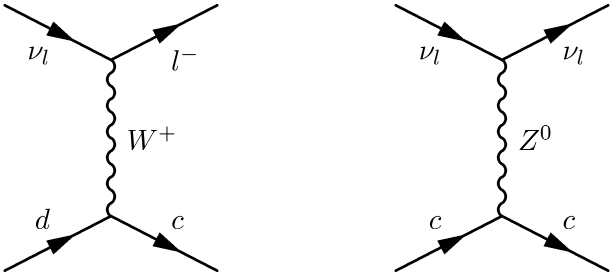

FIGURE 1.1 – Diagrams for neutrino scattering on quarks. Left, charged current interaction mediated by a $W^+$; right, meutral current interaction mediated by a $Z^0$ boson.

quarks produced in the interactions "dress" themselves to give rise to white hadrons in final states (quark *hadronization* or *fragmentation*).

We then see that real neutrino induced charm production is a rather complicate process: as we are going to explain, it mainly happens through deep inelastic scattering (DIS) of neutrinos on nucleons, but there are also other mechanisms involved, as quasielastic and diffractive production. We shall address these issues in the following sections.

## 1.2 Charm production in neutrino deep inelastic scattering

The dynamics of quarks is described by a non abelian gauge theory, the Quantum Chromodynamics (QCD) [23, 24]. As such, it has the remarkable property of *asymptotic ultraviolet freedom* [25, 26, 27], i.e., the running coupling costant, which is of order 0.1 at typical electroweak energies ($\sim M_W$), decreases with increasing energies. As a consequence, quarks (and gluons, the QCD gauge bosons) behave as free particles in the limit of large energies, or small distances.

This suggests that the problem mentioned above, of the description of the composition of hadrons in terms of quarks, can be greatly simplified: at least in the limit of high energy scattering, the hadron can be regarded as a compound of free particles. Such a description of hadrons is the content of the Quark Parton Model [28], which we are going to discuss together with its application to neutrino induced charm production through neutrino-nucleon deep inelastic scattering.

### 1.2.1 Inclusive deep inelastic scattering

The scattering of a neutrino off a nucleon ($n$ or $p$) can happen either through charged current interactions (CC) or through neutral current interactions (NC). In the first case, as we have seen, the interaction is mediated by a $W^{\pm}$ boson exchange, while in the latter by a $Z^0$.

Since we are ultimately interested in charm production by $\nu_\mu$ CC interactions, we shall consider the first one, and we shall restrict to muon neutrinos.

To begin with, we discuss inclusive scattering. Later on, we will add the request that a charm quark is present in the final state of the interaction.

#### Kinematics

We first consider the inclusive reaction

$$\nu_\mu(k)\; N(p) \to \mu(k')\; X(p') \tag{1.8}$$

whose Feynman diagram is represented in figure 1.2.

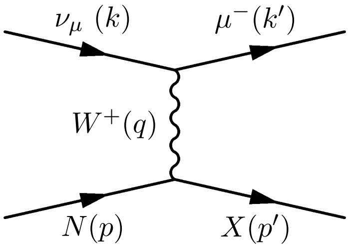

FIGURE 1.2 – Feynman diagram for $\nu_\mu$ scattering on a nucleon.

$N$ is the nucleon and $X$ is the (inclusive) hadronic final state. In brackets are the four-momenta, $p'$ being the sum of four-momenta of all the final hadrons. Usually Lorentz invariant quantities are used to describe the kinematics, such as

$$Q^2 = -q^2 = -\left(k - k'\right)^2 \qquad \text{four-momentum transfer (square)} \tag{1.9}$$

$$\nu = \frac{p \cdot q}{\sqrt{p \cdot p}} = E_\nu - E_\mu \qquad \text{energy transfer in the laboratory reference frame} \tag{1.10}$$

$$W^2 = p'^2 = M^2 - Q^2 + 2M\nu \qquad \text{hadronic final state invariant mass (square)} \tag{1.11}$$

$$x = \frac{Q^2}{2p \cdot q} = \frac{Q^2}{2M\nu} \qquad \text{Bjorken scaling variable} \tag{1.12}$$

$$y = \frac{p \cdot q}{p \cdot k} = \frac{E_h}{E_\nu} - \frac{M}{E_\nu} \qquad \text{inelasticity} \tag{1.13}$$

where $M$ is the nucleon mass and $E_h$ is the energy of the hadronic final state $X$. As we shall see below, in the Parton Model, the Bjorken $x$ will be interpreted as the target nucleon longitudinal momentum that was carried by the struck quark (or, equivalently, the fraction of nucleon momentum carried by the struck quark in that reference frame in which nucleon has infinite momentum, so that nucleon mass $M$ and transverse momentum are negligible).

In elastic scattering, one has $x = 1$. In fact, in that case, $p^2 = p'^2 = M^2$ and hence, from equation 1.11, $Q^2 = 2M\nu$ and $x = Q^2/2M\nu = 1$. Instead, if the scattering is inelastic, in general $W^2 \geq M^2$, thus $x$ can assume every value between 0 and 1. The deep inelastic region is defined by $\sqrt{Q^2}, \nu \gg M \sim 1$ GeV, $x$ fixed.

### Dynamics

In the expression of the cross section for the process $\nu_\mu N \to \mu^- X$ appears the matrix element of the hadronic charged current between the initial and final hadronic states (and at the end one has to sum over all possible hadronic final states, since we are considering an inclusive reaction). Unlike the case of quarks, which are elementary, nucleons are composite objects, so that the matrix element cannot be calculated directly. Instead, it can be expressed by means of certains *structure functions* $F_i^N(x, Q^2)$, $i = 1, 2, 3$, $N = n, p$, which subsume the information about internal structure and dynamics of the nucleon, relevant for the scattering process.

In terms of structure functions, the differential cross section, neglecting lepton masses, and for $Q^2 \ll M_W^2$, can be written as [29]

$$\frac{d^2\sigma^{\nu_\mu N}}{dx\,dy} = \frac{G_F^2\,M\,E_\nu}{\pi}\left[\frac{y^2}{2}2xF_1^N + \left(1 - y - \frac{Mxy}{2E_\nu}\right)F_2^N + y\left(1 - \frac{y}{2}\right)xF_3^N\right] \tag{1.14}$$

As anticipated theoretically by Bjorken [30] and confirmed by SLAC experiments [10, 11] in the case of electron-proton deep inelastic scattering, the $F_i^N$ should be independent of $Q^2$ in the limit of high energy transfer (Bjorken scaling). Roughly, this is because at high $Q^2$ the $W^+$ boson exchanged between the lepton and the nucleon probes the internal structure of the nucleon itself (at a length scale $\sim 1/\sqrt{Q^2} \ll 1/M$) and ultimately resolves its elementary constituents (partons). The cross section will then be given essentially by the scattering of the virtual boson on a parton in the nucleon. If we now assume that these objects are "pointlike", the scattering can only be elastic and then, since the structure functions for elastic scattering only depend on a single dimensionless invariant, the same holds for the $F_i^N$'s in the limit of high $Q^2$.

It must be stressed that in the above argument it is essential that the strong interaction between partons can be neglected during collision time, i.e. that strong interactions are described as an asymptotically free theory.

The Parton Model was proposed by Feynman to explain Bjorken scaling.

### Parton Model

In the spectroscopic model of hadrons by Gell-Mann [12] the nucleons are represented in terms of quarks as

$$p = u\,u\,d \qquad\qquad n = u\,d\,d$$

However, virtual quark pairs are continuously produced inside the nucleon through strong interactions of real quarks, and the electroweak boson exchanged can also interact with virtual quarks of the *sea* as does with the *valence* quarks. It is expected that virtual heavy quarks like $s$, $c$ will be rare inside nucleons, compared to the valence quarks.

In the Parton Model one then assumes that the nucleons can be described by a cloud of spin 1/2 pointlike partons of different flavours $u$, $d$, $c$, $s$ (the only active ones at typical neutrino energies of deep inelastic scattering experiments). The distribution of the parton of flavour $q$ in the nucleon $N$ is given by a function $q_N(\xi)$ such that $q_N(\xi)\,d\xi$ represents the number of $q$ partons having a fraction between $\xi$ and $\xi + d\xi$ of the nucleon longitudinal momentum, in the frame in which the nucleon has infinite momentum along the $W^+$ direction (Breit frame), where we can treat partons as collinear with the nucleon. So, neglecting partons and nucleon masses, the parton four-momentum is $\hat{p} = \xi p$ and

$$\hat{x} = \frac{Q^2}{2\hat{p}\cdot q} = \frac{x}{\xi} \tag{1.15}$$

$$\hat{y} = \frac{q\cdot\hat{p}}{k\cdot\hat{p}} = y \tag{1.16}$$

The cross sections for $\nu q$ and $\nu\bar{q}$ elastic scattering are [29]

$$\frac{d^2\sigma^{\nu q\to lq'}}{d\hat{x}\,d\hat{y}} = \delta(\hat{x}-1)\,\frac{d\sigma^{\nu q\to lq'}}{dy} = \delta\!\left(\frac{x}{\xi}-1\right)\frac{G_F^2 s\xi}{\pi}\,|V_{qq'}|^2 \qquad \begin{pmatrix}\nu_l\, d \to l^- u,\, l^- c\\ \nu_l\, s \to l^- u,\, l^- c\end{pmatrix} \tag{1.17}$$

$$\frac{d^2\sigma^{\nu\bar{q}\to l\bar{q}'}}{d\hat{x}\,d\hat{y}} = \delta(\hat{x}-1)\,\frac{d\sigma^{\nu\bar{q}\to l\bar{q}'}}{dy} = \delta\!\left(\frac{x}{\xi}-1\right)\frac{G_F^2 s\xi}{\pi}\,(1-y)^2\,|V_{qq'}|^2 \qquad \begin{pmatrix}\nu_l\, \bar{u} \to l^- \bar{d},\, l^- \bar{s}\\ \nu_l\, \bar{c} \to l^- \bar{d},\, l^- \bar{s}\end{pmatrix} \tag{1.18}$$

Here $\nu_l$ scattering on up type quarks ($u$ and $c$) does not appear because of charge conservation: the initial state would have charge 2/3 and it is impossible to have this same charge in the final state with a negative lepton and a quark.

Since, in the CM frame, $y = (1-\cos\theta)/2$, where $\theta$ is the scattering angle, the different $y$ dependencies of the two cross sections are consequence of the different total spin in the two reactions: as only left-handed quarks and neutrinos and right-handed quarks enter in charged currents, the $\nu\, q$ system has 0 total spin, and hence the first cross section is isotropic, while the $\nu\,\bar{q}$ system has total spin 1, whence the $\theta$ dependence of the cross section. Because of the $\delta$ functions in the cross sections, we see that, as anticipated, $x = \xi$ assumes the meaning of the fraction of nucleon four-momentum carried by the struck quark.

The $\nu_\mu N \to \mu^- X$ cross section is obtained by incoherently adding the cross sections for the individual $\nu q$ or $\nu\bar{q}$ scattering, weighted by the distribution functions $q_N$, $\bar{q}_N$. The final result is

$$\frac{d^2\sigma^{\nu_\mu N}}{dx\,dy} = \frac{G_F^2 s x}{\pi}\left[d_N(x) + s_N(x) + \big(\bar{u}_N(x) + \bar{c}_N(x)\big)(1-y)^2\right] \qquad N = n,\, p \tag{1.19}$$

Comparing this to equation 1.14, one obtains

$$F_1^N(x) = d_N(x) + s_N(x) + \bar{u}_N(x) + \bar{c}_N(x) \tag{1.20}$$

$$F_2^N(x) = 2x\,[d_N(x) + s_N(x) + \bar{u}_N(x) + \bar{c}_N(x)] \tag{1.21}$$

$$F_3^N(x) = 2\left[d_N(x) + s_N(x) - \big(\bar{u}_N(x) + \bar{c}_N(x)\big)\right] \tag{1.22}$$

satisfying in fact the Bjorken scaling. Also, the Callan-Gross relation

$$F_2^N = 2xF_1^N \tag{1.23}$$

holds, which is a consequence only of the fact that partons have spin 1/2.

Making the further assumption that strong isospin invariance holds, i.e.

$$\begin{aligned} d &:= d_p = u_n & u &:= u_p = d_n \\ \bar{d} &:= \bar{d}_p = \bar{u}_n & \bar{u} &:= \bar{u}_p = \bar{d}_n \\ s &:= s_p = s_n & c &:= c_p = c_n \\ \bar{s} &:= \bar{s}_p = \bar{s}_n & \bar{c} &:= \bar{c}_p = \bar{c}_n \end{aligned}$$

and that $s = \bar{s}$ and $c = \bar{c}$ (sea quarks are created in quark-antiquark pairs), then the scaling structure functions for scattering off an isoscalar target – i.e. an hypotetical nucleon which is an equal admixture of neutrons and protons – $F_i := \frac{1}{2}(F_i^P + F_i^N)$, $i = 1, 2, 3$, take the form

$$F_1(x) = \tfrac{1}{2}\big(u + \bar{u} + d + \bar{d} + s + \bar{s} + c + \bar{c}\big) \tag{1.24}$$

$$F_2(x) = 2xF_1(x) \tag{1.25}$$

$$F_3(x) = \big[u - \bar{u} + d - \bar{d} + c - \bar{c} + s - \bar{s} + 2(s - c)\big] \tag{1.26}$$

Experimentally, scaling holds only appoximatively, and logarithmic corrections show up at finite $Q^2$. These corrections can be calculated using QCD perturbation theory and asymptotic freedom. The result is that, at leading order, the parton model formulas for the structure functions remain unchanged, but parton distribution functions become dependent from $Q^2$ [31, 32, 33, 34], i.e. the composition of the nucleon in terms of quarks depends on the scale at which the nucleon itself is probed. Figure 1.3 shows the $x$ dependence of quark density functions of valence and sea quarks, for two different values of $Q^2$ and for two standard parametrizations, CTEQ [35] and GRV94LO [36, 37]. The sea is dominant at low $x$, while the valence quark abundance is peaked at $x \sim 0.2$, and the peak slightly moves backward at increasing $Q^2$.

### 1.2.2 Seminclusive charm production in deep inelastic scattering

Let us now go to the case in which a charm quark is produced in the scattering, i.e. we consider the seminclusive process

$$\nu_\mu N \longrightarrow \mu^- c X$$

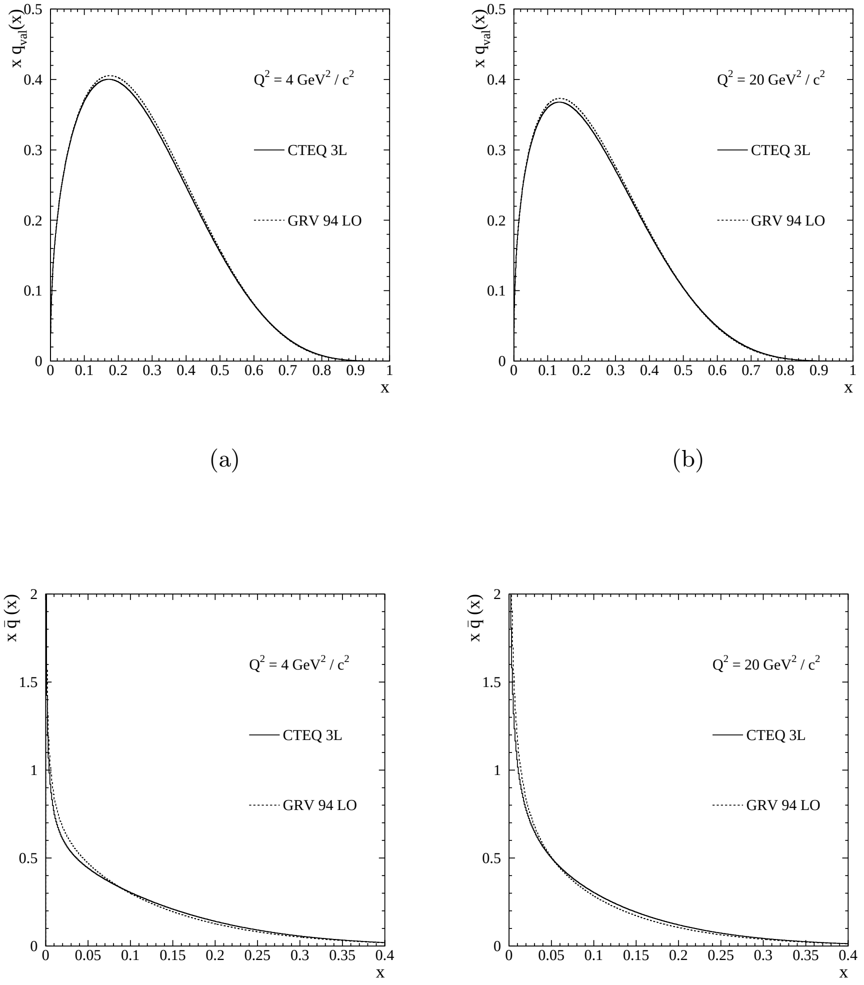

(a) (b)

(c) (d)

Figure 1.3 – Parton density functions for an isoscalar target for valence quarks – (a) and (b) – and for antiquarks – (c) and (d) – at two different values of $Q^2$ following two different parametrizations: CTEQ and GRV94LO.

where $X$ is a hadronic final state, and for the moment we neglect the hadronization of the final $c$ quark.

At partonic level, the relevant processes for $c$ production are [29]

$$\nu_\mu\, d \longrightarrow \mu^- c \qquad \frac{d\sigma^{\nu_\mu d\to\mu^- c}}{dy} = \frac{G_F^2 \hat{s}}{\pi}\left(1-\frac{m_c^2}{\hat{s}}\right)|V_{cd}|^2 \tag{1.27}$$

$$\nu_\mu\, s \longrightarrow \mu^- c \qquad \frac{d\sigma^{\nu_\mu s\to\mu^- c}}{dy} = \frac{G_F^2 \hat{s}}{\pi}\left(1-\frac{m_c^2}{\hat{s}}\right)|V_{cs}|^2 \tag{1.28}$$

where, as above, we distinguish with an hat the kinematical quantities referring to the $\nu\, q$ scattering process. It is then evident that production of $c$ quark through $\nu_\mu\, d$ scattering is Cabibbo suppressed ($|V_{cd}|^2 \sim \sin^2\theta_C \simeq 0.04$), while we expect that production through $\nu_\mu\, s$ scattering, for which $|V_{cs}|^2 \sim \cos^2\theta_C \simeq 0.96$, is instead suppressed by the low abundance of $s$ quarks in the sea.

Furthermore, there is the phase space suppression factor $(1-m_c^2/\hat{s})$, and for instance at $E_\nu = 20$ GeV,

$$\frac{m_c^2}{\hat{s}} = \frac{m_c^2}{m_s^2 + 2m_s E_\nu} \simeq \frac{m_c^2}{2m_s E_\nu} \simeq 0.4$$

for scattering against an $s$ quark ($m_s \simeq 150$ MeV, $m_c \simeq 1.3$ GeV). We thus expect $\nu$ induced charm production to be quite a rare process with respect to all $\nu$ deep inelastic interactions.

If again $\hat{p} = \xi p$ is the parton four-momentum, if a $c$ quark is produced in the final state, and neglecting the initial parton mass ($m_d$, $m_s \ll m_c$), we have

$$m_c^2 = (\hat{p}+q)^2 = -Q^2 + 2\xi p\cdot q = -Q^2 + \frac{\xi Q^2}{x} \tag{1.29}$$

Hence, at variance with the formulas of the above section 1.2.1, where we neglected both initial and final parton's masses, the parton distribution will be probed at

$$\xi = x\left(1+\frac{m_c^2}{Q^2}\right) \tag{1.30}$$

which is called the *slow rescaling* variable [38, 39], and takes into account the kinetic energy needed to excite a $c$ quark to the mass shell.

The cross section for charm production induced by neutrino scattering off an isoscalar target $T$ then reads

$$\frac{d^2\sigma^{\nu_\mu T\to\mu^- cX}}{dx\,dy} = \frac{G_F^2 s\xi}{2\pi}\left[(u(\xi)+d(\xi))\,|V_{cd}|^2 + 2s(\xi)|V_{cs}|^2\right]\left(1-\frac{m_c^2}{s\xi}\right)\theta\left(\xi-\frac{m_c^2}{s}\right) \tag{1.31}$$

To get a rough estimate of the relative abundance of charm producing $\nu$ interactions, since $\hat{s} = (\xi p + k)^2 \simeq \xi s$, we can replace the kinematic factor $(1 - m_c^2/s\xi)$ in 1.31, with $(1 - m_c^2/\hat{s}) \simeq 0.6$, and taking into account the results of section 1.2.1 and the further assumption $s(x) = \bar{s}(x) = c(x) = \bar{c}(x)$, we get

$$\frac{\sigma^{\nu_\mu T \to \mu^- cX}}{\sigma^{\nu_\mu T \to \mu^- X}} \simeq \frac{\big(U + D\big)|V_{cd}|^2 + 2S|V_{cs}|^2}{U + D + 2S + \frac{1}{3}\big(\bar{U} + \bar{D} + 2\bar{S}\big)} \left(1 - \frac{m_c^2}{\hat{s}}\right) \tag{1.32}$$

where

$$Q = \int_0^1 x\, q(x)\, dx, \quad Q = U,\, D,\, S \tag{1.33}$$

is the fraction of nucleon's momentum carried by $q$ quarks, and analogous for $\bar{Q}$.

Using the world averages, we assume

$$\eta_s := \frac{2S}{U + D} = 0.061 \pm 0.004$$
$$\kappa := \frac{2\bar{S}}{\bar{U} + \bar{D}} = 0.40 \pm 0.05$$

($\kappa$ is the strangeness content of the sea). Then, for $E_\nu = 20$ GeV, we obtain

$$\frac{\sigma^{\nu_\mu T \to \mu^- cX}}{\sigma^{\nu_\mu T \to \mu^- X}} \simeq \frac{6}{10} \frac{\frac{1}{\eta_s}|V_{cd}|^2 + |V_{cs}|^2}{\frac{1}{\eta_s} + 1 + \frac{1}{3}\left(\frac{1}{\kappa} + 1\right)} \simeq 0.056 \pm 0.008 \tag{1.34}$$

i.e., that about 6% of all charged current interactions have a charm quark in the final state. The actual ratio is likely to be lower, since we neglected threshold effects, modeled by the $\theta$ function in 1.31. In fact, an experimental result coming from E531 [41], quoted an average cross section ratio $\sigma^{\nu_\mu T \to \mu^- cX}/\sigma^{\nu_\mu T \to \mu^- X} = (4.9^{+0.7}_{-0.6})\%$.

### 1.2.3 Charm quark hadronization for deep inelastic scattering

The process $\nu_\mu\, N \longrightarrow \mu^- c\, X$ is not directly accessible by an experiment, since only colour neutral hadrons can be observed. In principle, this should not be a problem, if one is interested only in the total charm production cross section: the strong interactions, which dress the charm quark converting it into a white hadron, are flavour conserving, so if a $c$ quark is produced at partonic level, necessarily there will be a charmed hadron in the final (observable) state. Thus, the observed rate of production of all final states containing a charmed hadron, will coincide with the rate of production of a $c$ quark. This argument, however, is invalidated by the fact that experimental efficiencies and acceptances – which have to be taken into account in the evaluation of observed rates – depend on the kinematic variables of the observed hadrons, not of quarks. It is then necessary, in order to parametrize the cross sections in terms of observable kinematic variables, to understand their relations with the corresponding partonic ones.

The various charmed hadrons produced in neutrino interactions, which include excited states decaying via strong or electromagnetic interactions, eventually reduce to the four particles $D^0$, $D^+$, $D_s^+$, $\Lambda_c$. These particles, whose main properties are summarized in table 1.2, then decay to non-charmed states via the electroweak interaction, with decay paths of the order of 1 mm at our energies. Their decays can then be indentified in the emulsions, although the topology of the event only allows to distinguish neutral from charged charmed particles. Here we briefly discuss the known characteristics of the hadronization process, which, starting from the $c$ quark momentum, describes the momentum distribution of the eventually observed charmed particle. The determination from the CHORUS data of the relative fractions of the three charged charmed particles is then the main goal of the analysis discussed in chapter 4.

| Hadron | Valence quarks | Mass [MeV] | Lifetime [s·$10^{13}$] |
|---|---|---|---|
| $D^0$ | $c\bar{u}$ | $1864.6 \pm 0.5$ | $4.126 \pm 0.028$ |
| $D^+$ | $c\bar{d}$ | $1869.3 \pm 0.5$ | $10.51 \pm 0.13$ |
| $D_s^+$ | $c\bar{s}$ | $1968.0 \pm 0.6$ | $4.96 \pm 0.10$ |
| $\Lambda_c$ | $udc$ | $2284.9 \pm 0.6$ | $1.88 \pm 0.07$ |

Table 1.2 – Main properties of charmed hadrons from [21].

The hadronization (or fragmentation) process, in which a quark is converted to a hadron through its binding to virtual quarks or antiquarks, mediated by gluon exchange, typically involves relatively low energies – of the order of hadron masses, and is then not calculable in QCD perturbation theory.

However, the hadronization process has been carefully studied in many different reactions, and it has been found that a satisfying description can be achieved in terms of the so called *fragmentation functions*. A fragmentation function $D_{H/q}(z, p_\perp)$ is the suitably normalized probability density for a quark $q$ to fragment into a hadron $H$ having longitudinal momentum $zp_H^{max}$ and transverse momentum $p_\perp$ with respect to the quark's momentum in the final hadronic system centre of mass frame, where $p_H^{max}$ is the maximum momentum that $H$ can have. In the limit of high energies, $p_H^{max} \simeq p_q$.

$D_{H/q}$ is normalized in such a way that

$$f_{H/q} = \int_0^1 dz \int_0^{+\infty} dp_\perp D_{H/q}(z, p_\perp) \tag{1.35}$$

is the fraction of $H$ hadrons produced in the fragmentation, and

$$\sum_H f_{H/q} = 1 \tag{1.36}$$

Hence, assuming factorization of charm production and charm fragmentation, the cross section of the production of a stable charmed hadron $C$ in deep inelastic scattering off an isoscalar target $T$ will be

$$\frac{d^4\sigma^{\nu_\mu T \to \mu^- C\, X}}{dx\, dy\, dz\, dp_\perp} = \frac{d^2\sigma^{\nu_\mu T \to \mu^- C\, X}}{dx\, dy} \sum_C D_{C/q}(z, p_\perp) \tag{1.37}$$

Several different phenomenological parametrizations are used for the fragmentation functions, often inspired by QCD calculations or arguments, and adapted on a case by case basis. Here, we shall only mention the Lund parametrization [42], designed for light quarks, and the Peterson parametrization [43], used for heavy quarks such as $c$.

The Lund parametrization is

$$D_{H/q}(z, p_\perp) \propto \frac{1}{z}(1-z)^a \, \mathrm{e}^{-b m_\perp / z} \, \mathrm{e}^{-\beta p_\perp^2} \tag{1.38}$$

where $m_\perp = \sqrt{m_H^2 + p_\perp^2}$ is the hadron transverse mass, and $a$, $b$ and $\beta$ are parameters extracted from experiments.

The Peterson parametrization, which is based on the observation that at high energies a heavy quark is only slightly decelerated by an attaching quark, so that $z$ has to be peaked at 1, is

$$D_{H/q}(z, p_\perp) \propto \frac{1}{z}\left(1 - \frac{1}{z} - \frac{\varepsilon_P}{1-z}\right)^{-2} \mathrm{e}^{-\beta p_\perp^2} \tag{1.39}$$

where again $\varepsilon_P$ and $\beta$ are free parameters. Figure 1.4 shows $D_{H/c}(z, 0)$ for two different values of $\varepsilon_P$, coming from two different experiments, CHARM II [44] and CCFR [45], while for $q = c$ as well, LEBC EHS measured $\beta = 1.1 \pm 0.3$, corresponding to $\langle p_\perp^2 \rangle = 0.9 \pm 0.2$ GeV$^2$ [46].

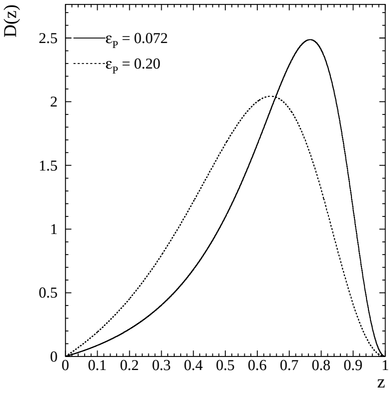

FIGURE 1.4 – The Peterson fragmentation function for $c$ quark for two values of $\varepsilon_P$, i.e. $\varepsilon_P = 0.072$ obtained by CHARM II and $\varepsilon_P = 0.20$ of CCFR.

For what concerns production fractions, there is no really reliable model yet, and they have to be taken from experiments. This is a consequence of the fact that, even if one should in principle expect that the fragmentation process is universal, actually several of its features depend on the specific reaction, e.g. through recombination: a $c$ quark, produced by a neutrino interaction on a valence $d$ quark inside a proton, will fragment differently from one produced by the same interaction inside a neutron, because the partonic final state is $c\,u\,u$ in the first case, and $c\,u\,d$ in the latter, and the three quarks will recombine with $q\,\bar{q}$ differently from each other to form hadrons.

Then, production fractions used e.g. in Monte Carlo's are usually taken from experimental results: as discussed in section 1.4 below, the relative fractions were measured by the emulsion experiment E531, and that measurement is generally used in those analyses (e.g. dimuon experiments) where the knolwedge of the fractions is needed to unfold the charm production cross section from the measured one.

## 1.3 Other production mechanisms

The partonic description of neutrino-hadron interactions reviewed in the last section, gives results in good agreement with experiments at large $Q^2$, i.e. in the deep inelastic scattering region. As we have seen, the reason for this is basically the fact that in the parton model the nucleon is described as a cloud of free particles, and this picture agrees with that given by the QCD precisely in the limit of high momentum transfer, due to the fact that QCD is an asymptotically free theory in the ultraviolet.

One then expects that at lower $Q^2$ values, where the description of nucleons as clouds of free quarks breaks down, other charm production mechanisms may become relevant. This is actually the case, and in this section such processes are going to be breifly discussed.

### 1.3.1 Quasielastic scattering

In $\nu N$ scattering at low $Q^2$ (i.e. for $Q^2 \sim 1$ GeV), the virtual $W$ probes the nucleon at large length scales and then, instead of resolving the nucleon's internal structure, the boson will see the nucleon as a pointlike target. This does not break up, and in the final state there will be a single baryon (besides a lepton). Such a process is called *quasielastic scattering.*

For what concerns charm production, the most relevant quasielastic process is

$$\nu_\mu \, n \longrightarrow \mu^- \Lambda_c \tag{1.40}$$

The cross section for this process can be calculated by relating it through quark symmetries to the well studied process

$$\nu_\mu \, n \longrightarrow \mu^- p \tag{1.41}$$

In fact, according to the $SU(4)$ classification of hadrons, one has

$$n = u\,d\,d \qquad\qquad p = u\,u\,d \qquad\qquad \Lambda_c = u\,d\,c$$

thus the matrix element of the hadronic charged current between the states $|n\rangle$ and $|\Lambda_c\rangle$, which appears in the cross section for the process 1.40, can be related through $SU(4)$ symmetry to the matrix element of the same current between $|n\rangle$ and $|p\rangle$, which enters in the cross section for the process 1.41. Though, the $SU(4)$ symmetry is rather badly broken by the quark mass differences.

The matrix element for $\nu_\mu \, n \to \mu^- p$ is then expressed in terms of nucleon form factors, in analogy to the deep inelastic scattering case. The result is

$$\frac{d\sigma^{\nu_\mu \, n \to \mu^- p}}{dQ^2} = \frac{G_F^2 M \cos^2\theta_C}{8\pi E_\nu^2} \left( A(Q^2) - B(Q^2)\frac{s-u}{M^2} + C(Q^2)\frac{(s-u)^2}{M^4} \right) \tag{1.42}$$

where $s - u = 4ME_\nu - Q^2 - m_\mu^2$ and $A$, $B$, $C$ are functions of $Q^2$, of nucleon and lepton masses and of neucleon form factors. In the high energy limit, when $E_\nu \gg M$, this reduces to

$$\frac{d\sigma^{\nu_\mu\, n\to\mu^- p}}{dQ^2} \simeq \frac{2G_F \cos^2\theta_C}{\pi}\, C(Q^2) \tag{1.43}$$

i.e. the cross section is independent from neutrino energy. As form factors decrease rapidly with $Q^2$, the total cross section

$$\sigma^{\nu_\mu\, n\to\mu^- \Lambda_c} = \int_0^{+\infty} \frac{d\sigma}{dQ^2}\, dQ^2 \tag{1.44}$$

is finite and independent of $E_\nu$.

Using these results, and $SU(4)$ flavour symmetry, Shrock and Lee calculated $\sigma^{\nu_\mu\, n\to\mu^-\Lambda_c} = 2.4$ fb for $E_\nu > 20$ GeV. The E531 experiment, through the observation of 3 quasielastic events with $\Lambda_c$ production out of a total of about 3,000 neutrino CC interactions, quoted $\sigma^{\nu_\mu\, n\to\mu^-\Lambda_c}/\sigma^{\nu_\mu\, n\to\mu^- X} = 0.37^{+0.37}_{-0.23}$ [41]. Making the assumption that the cross section is independent of neutrino energy, and translating the E531 result in an upper limit [47], limits on quasielastic charm production with respect to overall charm production cross section can be quoted for various neutrino energies, as shown in table 1.3.

| $E_\nu$ [GeV] | 10 | 20 | 30 | 50 | 100 |
|---|---|---|---|---|---|
| QE [%] | 88 | 24 | 13 | 6 | 2.5 |

TABLE 1.3 – Upper limits at 90% C.L. on fractions of charm produced in quasielastic $\nu_\mu$ interactions with respect to the overall neutrino charm production, assuming that the quasielastic cross section is independent from neutrino energy.

### 1.3.2 Diffractive production

The diffractive production of a charmed meson can occur when the virtual $W^+$ boson, emitted by the neutrino, transforms into a $c\bar{s}$ or $c\bar{d}$ pair, which hadronically scatters off a nucleon (or even off the nucleus) transforming into an on shell $D_s^+$, $D_s^{*+}$ or $D^+$, $D^{*+}$ meson. Figure 1.5 represents the lowest order Feynman diagram for the process, in which the interaction of the $c\bar{s}$ pair with the nucleon is schematized by the exchange of a Pomeron object (which carries vacuum quantum numbers).

The first half of the process, up to $W^+ \to c\bar{s}$, is the time reversed of the decay $D_s^{*+} \to \bar{\nu}_\mu\, \mu^-$, so that, according to vector meson dominance (VMD), the cross section

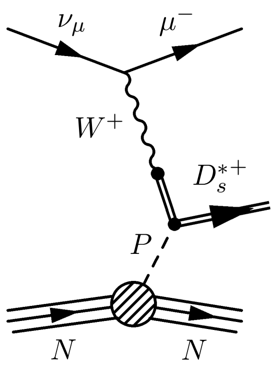

FIGURE 1.5 – Feynman diagram for the diffractive production of the $D_s^{*+}$ resonance.

can be written as the product of two factors: one for such decay, and the other for the elastic scattering of the meson and the nucleon. Then the rate for this latter process can be calculated again by $SU(4)$ symmetry [48].

However, uncertainities on parameters entering the calculation propagate exponentially, resulting in quite large errors on the cross section [49]. Therefore, theoretically, only a semiquantitative treatment is possible.

The diffractive production of a $D^{*+}$ meson, which is a $c\bar{d}$ state, is Cabibbo suppressed with respect to that of $D_s^{*+}$, by a factor $|V_{cd}/V_{cs}|^2 \simeq \sin^2\theta_C/\cos^2\theta_C \sim 4\cdot 10^{-2}$ (otherwise it would be of the same order).

Also the diffractive production of pseudoscalar mesons $D^+$ and $D_s^+$ is suppressed in the CHORUS kinematic range [50], so that mostly $D_s^{*+}$ vector mesons are produced diffractively.

This kind of reaction has been observed first in bubble chamber and emulsion experiments [51], then in dense target ones [52]. One candidate event, consistent with the above predictions, has been observed by CHORUS in a dedicated search [53]. Recently the NuTeV collaboration found evidence of diffractive charm production in $\nu_\mu\, Fe$ scattering [52], with a relative cross section of

$$\frac{\sigma_{\rm diff}^{D_s^+ + D_s^{*+}}}{\sigma^{\nu_\mu\, n\to\mu^- c\, X}} \simeq 3.5\%$$

at $E_\nu = 130$ GeV. Note that this energy is much higher than the CHORUS average neutrino energy.

## 1.4 Current experimental status

The experimental study of charm production in neutrino interactions is characterized by two requirements which are somehow difficult to fulfil at a time. The first one is related to the smallness of neutrino cross section, and consists in the fact that very massive detectors are needed. The second requirement is to be able to detect the short living charmed hadrons, but this is in most cases awkward, since large detectors can be too coarse.

Traditional experiments, essentially consisting in large tracking calorimeters, are then sensitive only to semimuonic charm decays, i.e. to the process

$$\begin{array}{l} \nu_\mu \, N \longrightarrow \mu^- \, C \;\; X \\ \qquad\qquad\quad \downarrow \\ \qquad\qquad\quad \mu^+ \, \nu_\mu \, X' \end{array}$$

where $C$ can be $D^0$, $D^+$, $D_s^+$ or $\Lambda_c$. These are often referred to as opposite sign dimuon events. The muonic branching ratios of charmed hadrons are 6.6% for $D^0$, 17.2% for $D^+$, 5.0% for $D_s^+$ and 4.5% for $\Lambda_c$. The background is usually quite important (around $15\% \div 20\%$) and comes from muonic decays of secondary kaons and pions.

Among the experiments that gave relevant results using this kind of analysis are CDHS, CHARM II, NOMAD at CERN, CCFR and NuTeV at Fermilab.

These provided masurements of the charm mass, of the strange sea properties, of the charm production rate, of the parameters of fragmentation functions. What is relevant for us is that counter experiments are not able to measure the relative fractions of charmed hadrons, and, on the contrary, need to take them from external measurements because they are needed to pass from dimuon to absolute charm rates.

E531 at Fermilab was the only experiment before CHORUS that could measure the relative fractions, because it could directly observe the charmed hadron decays: in fact, it also used nuclear emulsions as a target, and was optimized to perform particle identification, being able to measure both decay length and momentum of the decaying hadrons.

### 1.4.1 Dimuon experiments

Here we give a brief description of some experiments that studied dimuon events, and a summary of their statistics and results in charm physics obtained in QCD leading order analyses. These are compared in table 1.4.

CDHS [54] was exposed in the early eighties to the Wide Band and to the Narrow Band neutrino beams at CERN, for an average neutrino energy of 20 GeV. The detector consisted in a calorimeter made of magnetized iron plates interleaved to scintillator planes and drift chambers. The hadronic energy resolution slightly depended on the vertex position, and was $\sigma(E)/E = (58 \div 70)\%/\sqrt{E}$ ($E$ in GeV). The resolution on muon momentum was $\sigma(p)/p = 9\%$. CDHS, having a total mass of 1,250 tons, collected the largest dimuon statistics available up to now.

CCFR [55, 45] took data in the eighties at the Wide Band neutrino beam at Fermilab. It had the highest average neutrino energy, $E_\nu \simeq 140$ GeV. The detector consisted of a 690 tons target calorimeter of iron plates, scintillators and drift chambers with resolution $\sigma(E)/E = 89\%/\sqrt{E}$, followed by a toroidal muon spectrometer of 420 tons mass with resolution $\sigma(p)/p = 11\%$.

CHARM II [44] was exposed from 1987 to 1991 to the Wide Band neutrino beam at CERN. The average energy of the incident neutrinos was about 24 GeV. The target/tracker was composed of glass plates interleaved to streamer tubes and scintillating counters, with a hadronic energy resolution $\sigma(E)/E = 52\%/\sqrt{E} + 2\%$. The muon spectrometer followed, with resolution $\sigma(p)/p = 13\%$. The target mass amounted to 700 tons.

NOMAD [40] was originally designed to study neutrino oscillations, and provided the most recent measurements of $m_c$, $\kappa$ and $B_\mu$. It was exposed, together with CHORUS, from 1994 to 1997 to the Wide Band neutrino beam at CERN, and neutrinos reaching the detector had an average energy of about 24 GeV.

The detector for dimuon studies, having a total mass of 18 tons, consists of a front iron-scintillator calorimeter with a resolution $\sigma(E)/E = 100\%/\sqrt{E}$, drift chambers for tracking, an electromagnetic calorimeter having resolution $\sigma(E)/E = 3.2\%/\sqrt{E} + 1\%$. These, with other subdetectors, are located inside a 0.4 T magnetic field. Outside there is a hadronic calorimeter ($\sigma(E)/E = 100\%/\sqrt{E}$) and drift chambers for muon tracking. The resolution on muon momentum is $\sigma(p)/p = 3\%$ below 20 GeV.

For the analysis, opposite sign dimuon events are selected, and the background is evaluated from the like sign dimuon events observed plus a Monte Carlo simulation to correct for different acceptances and leading charge effects. The backgroud distributions are then subtracted bin by bin from the dimuon ones. Then, $m_c$, $\kappa$, $B_\mu$ are evaluated by fitting the corrected kinematic distributions. In the Monte Carlo, the relative fractions of charmed hadrons are fixed parameters, and the values of E531 are used.

| | $\langle E_\nu \rangle$ (GeV) | $N_{\text{di-}\mu}$ from $\nu$ | $N_{\text{di-}\mu}$ from $\bar{\nu}$ | $m_c$ (GeV) | $\kappa$ | $B_\mu$ (%) |
|---|---|---|---|---|---|---|
| CDHS | 20 | 9922 | 2123 | — | $0.47 \pm 0.08$ | $8.4 \pm 1.5$ |
| CCFR | 140 | 4503 | 632 | $1.3 \pm 0.2$ | $0.37 \pm 0.05$ | $10.9 \pm 0.8$ |
| CHARM II | 24 | 3100 | 700 | $1.8 \pm 0.4$ | $0.39 \pm 0.09$ | $9.1 \pm 0.9$ |
| NOMAD | 24 | 2714 | 115 | $1.3 \pm 0.4$ | $0.48 \pm 0.16$ | $9.5 \pm 1.5$ |

TABLE 1.4 – Statistics and results of dimuon experiments on $m_c$, $\kappa$, $B_\mu$. Systematic and statistical errors are summed in quadrature and symmetrized. The number of dimuon events is background subtracted. In CDHS, the charm mass was kept fixed at the value $m_c = 1.5$ GeV. The measurement of $\kappa$ by CCFR comes from the leading order analysis. Also a next-to-leading order analysis was performed, giving $\kappa = 0.48 \pm 0.06$.

Table 1.4 compares the results of the above experiments on $m_c$, $\kappa$, $B_\mu$.

### 1.4.2 The E531 experiment

The FNAL E531 experiment was exposed in the period 1978–1981 to the wide band neutrino beam at Fermilab, providing an average neutrino energy of 22 GeV. For the detector, a hybrid setup was adopted: the target was composed of 23 liters of nuclear emulsion. An emulsion experiment overtakes the resolution problems of conventional detectors, since the spatial resolution of nuclear emulsion allows the observation of the charmed hadron decay path.

The experiment was specifically designed to have full kinematic reconstruction of the event and particle identification, in order to determine the type of charmed hadron produced on an event by event basis, by reconstructing its invariant mass. The electronic part of the detector consisted in a drift chamber spectrometr, a time of flight system, a lead-glass plus an iron calorimeter and an end system to identify muons. It was possible to determine the momentum of the charged decay tracks with a resolution $\sigma(p)/p = \sqrt{0.014^2 + (0.04 \cdot p)^2}$.

The total event sample consisted in 3,855 neutrino interactions, 3,601 coming from $\nu_\mu$ CC and NC interactions, 192 from $\bar{\nu}_\mu$ CC and NC interactions, and 60 coming from $\nu_e$ and $\bar{\nu}_e$ interactions. In the total sample, 121 events were labelled as containing a charm decay. The expected background consisted of 0.2 events for decays of neutral particles, and 3.6 events for decays of charged particles.

As mentioned, the identification of the decaying hadron was possible event by event, thus E531 was able to determine the relative fraction of charmed hadrons in the sample, extending the analysis to all the decay channels. The result is summarized in table 1.5.

| Hadron | $D^0$ | $D^+$ | $D_s^+$ | $\Lambda_c$ |
|---|---|---|---|---|
| Fraction (%) | $46^{+6}_{-5}$ | $33^{+6}_{-8}$ | $5^{+4}_{-2}$ | $16^{+8}_{-4}$ |

Table 1.5 – Charmed hadron fractions measured by E531.

## CHAPTER 2

# The CHORUS detector

CHORUS was designed to search for $\nu_\mu \rightarrow \nu_\tau$ oscillations via the direct observation of the decay of the $\tau$ lepton produced in the interaction $\nu_\tau\, N \rightarrow \tau^- X$ and the subsequent $\tau$ decay in muon or in a negative hadron. The direct observation of the short $\tau$ track (about 1 mm at the CHORUS typical energies) and of the "kink" that follows, requires a very good resolution at vertex, both in angle and in position. The resolution needed is that typical of nuclear emulsion films.

For CHORUS, a "hybrid" approach was adopted [56], with a target/tracker of nuclear emulsions, which guarantees the desired resolution, followed by electronic detectors that measure the kinematics of the event, i.e. momenta of hadrons and muons, electromgnetic and hadronic energy of the event. The full detector structure is showed in figure 2.1.

We are first going to describe the wide band neutrino beam (WBB) of the CERN SPS, to which CHORUS was exposed from 1994 to 1997, then the emulsion target and the electronic detector: the target trackers, the hadron spectrometer, the calorimeter, the muon spectrometer and the trigger.

## 2.1 Wide Band Beam

The West Area neutrino facility [57] of the CERN Super Proton Synchrotron (SPS) provides a $\nu_\mu$ beam with energy well above the $\nu_\tau$ charged current interaction threshold. In the SPS, protons from the Proton Synchrotron (PS) are accelerated up to 450 GeV with a cycle of 14.4 s.

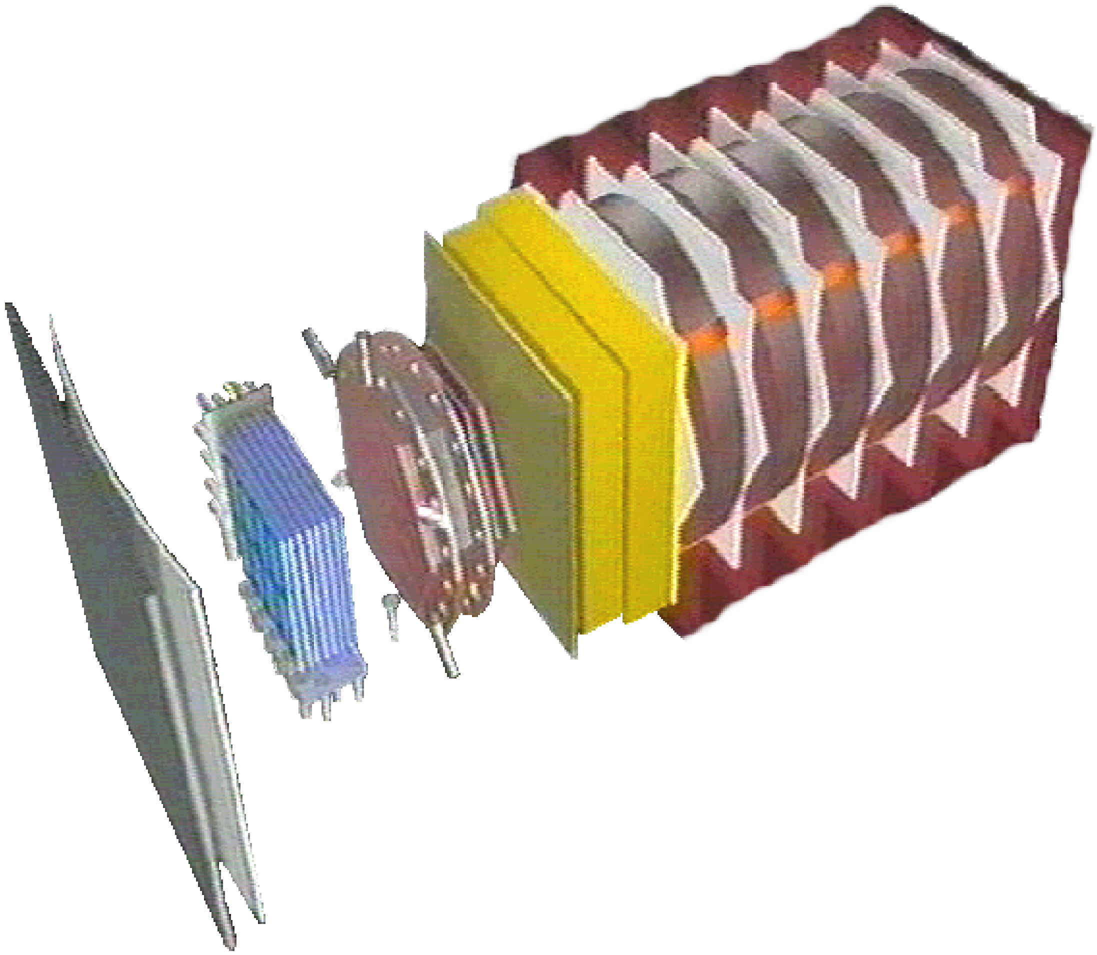

Figure 2.1 – The full view of the CHORUS detector. From left to right: veto planes, target region with emulsion stacks and fibre tracker planes, hadron spectrometer, calorimeter, muon spectrometer.

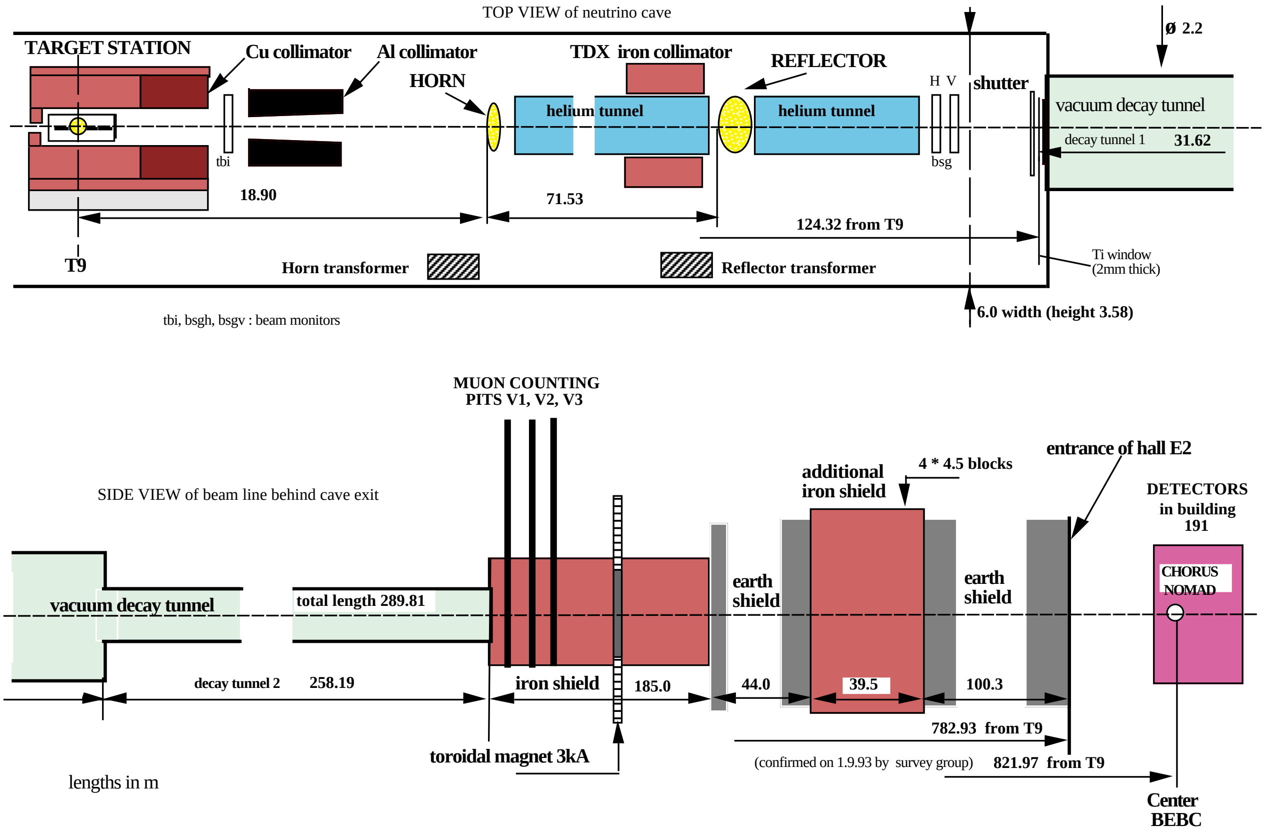

FIGURE 2.2 – The Wide Band Beam setup.

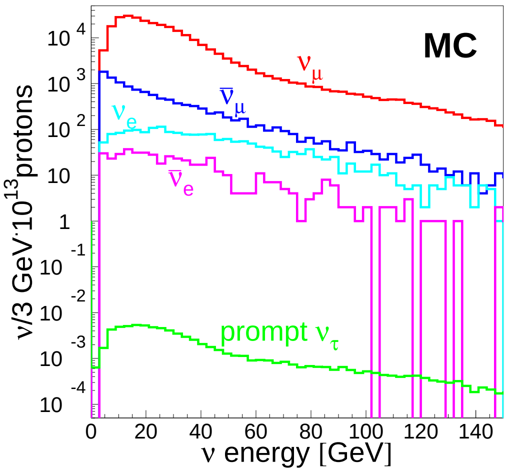

FIGURE 2.3 – The Wide Band Beam spectrum at the CHORUS detector.

Up to $1.8 \cdot 10^{13}$ protons are extracted in two 6 ms long spills separated by 2.7 s and sent to a beryllium target [58]. This is composed by six bars (3 mm of diameter, 10 cm long), spaced by 9 cm: the particular structure of the target avoids the reabsorbtion of the interaction products in the material.

The target is followed on the beam line by two focusing magnets, *horn* and *reflector*, after 20 and 90 m respectivley. The magnets select the charge of the mesons produced in the proton interaction, focusing the positive one in order to have a neutrino beam, and defocusing the negative ones. Nevertheless, a small contamination of antineutrinos from negative parent particles is present in the beam.

Downstream the magnet is a 290 m long decay tunnel, followed by a shield which absorbs hadrons not decayed and muons produced with neutrinos. The beam line has an upward slope of 42 mrad, and axis of the CHORUS detector is inclined correspondingly. The beam setup is showed in figure 2.2.

The dominant component of the beam is $\nu_\mu$, with a 4% contamination of $\bar{\nu}_\mu$, due to negative hadrons not defocused by the magnets, and a 1% of $\nu_e$ and $\bar{\nu}_e$, mainly coming from three body decays of kaons. The prompt $\nu_\tau$ component, coming from $D_s^+$ decays in $\tau$, is estimated to $3.3 \cdot 10^{-6}$ charged current interactions every $\nu_\mu$ charged current interaction [59], thus not affecting the sensitivity to oscillations. The energy spectra of the components is shown in figure 2.3 while the relative abundances are summarized in table 2.1.

| Component | Relative abundance | Average energy (GeV) |
|---|---|---|
| $\nu_\mu$ | 1 | $2.9 \pm 0.5$ |
| $\bar{\nu}_\mu$ | $0.056 \pm 0.004$ | $21.7 \pm 1.0$ |
| $\nu_e$ | $0.0070 \pm 0.0013$ | $47.9 \pm 2.2$ |
| $\bar{\nu}_e$ | $0.0017 \pm 0.0003$ | $35.3 \pm 1.7$ |

Table 2.1 – Track selector efficiency for different ranges of angle.

## 2.2 The target

The CHORUS target is composed of nuclear emulsion stacks interleaved to planes of scintillating fibre trackers. The fibre planes are used for tracking in the target area and vertex reconstruction, and provide the correlation of emulsion tracks to a given event recorded by the electronic detector: vertex and tracks reconstructed in the electronic detector are used as a prediction, to guide the location of the event first on interface emulsion sheets where the prediction is refined, and then in emulsion . The emulsion analysis is described in detail in chapter 3.

### 2.2.1 Emulsion target

Nuclear emulsions provide the tridimensional reconstruction of a track with a resolution of the order of 1 $\mu$m, being ideal for the study of interactions involving short lived particles, as $\tau$ leptons or charmed hadrons, characterized by $c\tau$ of about 1 mm. If the decay is identified directly, the information on the hadron produced is much richer. The best results up to now were obtained by E531, that used a 23 liters target.

CHORUS emulsions are made of microcrystals of silver halides (namely AgBr) disperesed in a gelatine layer. The crystals are the sensitive agent in which the latent image produced by a charged particle is formed. The grain size ranges from 0.2 to 0.5 $\mu$m, and there are on average 300 grains per mm of track length.

Neutrino experiments need massive targets: CHORUS uses 206 l of emulsion (i.e. 770 Kg), which then had to be set in suitable way to keep the big mass of emulsion in a stable structure. The target is divided in four stacks, each corresponding to 1 radiation

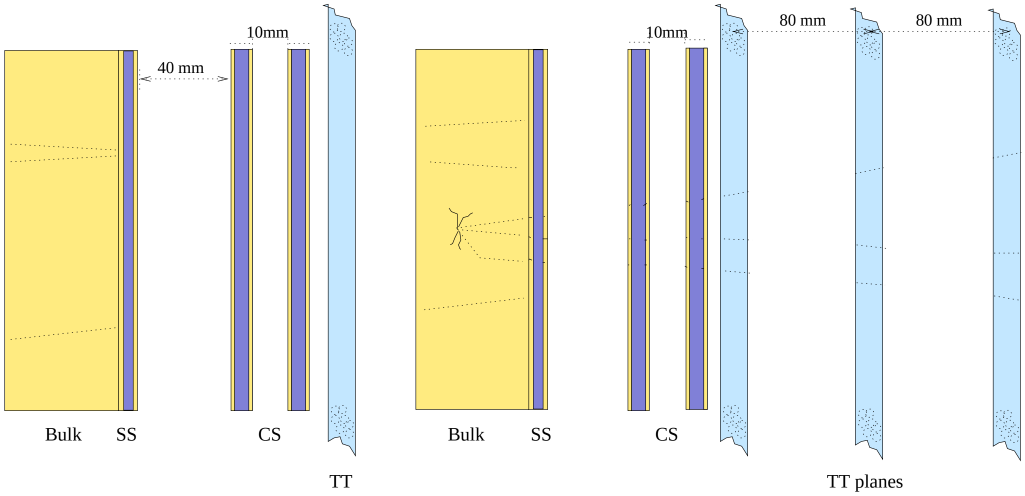

Figure 2.4 – Emulsion stacks and scintillating fibre tracker planes. This structure is repeated twice.

length and to 0.08 interaction lengths[1]. The stacks have a surface of 1.42 × 1.44 $m^2$, and a thickness of 2.8 cm. Each stack is then subdivided in 8 sectors of 0.71 × 0.36 $m^2$, and is formed by 36 plates.

The plates consist of 350 $\mu$m of emulsion gel poured onto the two of the faces of a 90 $\mu$m foil of tri-acetate cellulose. After drying, the plates were piled up and packed in a thin envelope of aluminized paper to form a sector.

Each stack is completed by three sets of interface emulsion thin sheets having the same transverse dimensions, consisting of 100 $\mu$m of gel held by a 0.8 mm thick acrylic plate. They were inserted in order to make predictions on track location in emulsion, so the first sheet, called *special* is immediately after the emulsion stack, while the remainimg two, called *changeable*, are positioned in front of the first tracker plane downstream the stack, in order to minimize the error on extrapolation of the tracks from target tracker. The target layout is shown in figure 2.4. The relative alignment of the interface sheets is realized with X-ray guns that create a pattern of fiducial marks, while the relative alignment of the stacks is given by passing through muons.

---

[1] In emulsion, $X_0 \simeq 29$ mm and $\lambda \simeq 35$ cm.

Since nuclear emulsions suffer of *fading*, i.e. the degradation of the latent image produced by the charged particle passing, they can be left undeveloped only for a limited period: the bulk stacks have been changed once, after two years of data taking, while the changeable sheets have been changed more frequently in order to keep the background level low (and the real track visibility high). However, to slow down the fading, the target, together with the target trackers and the magnetic spectrometer, are kept inside a cool box at the constant temperature of 5°C and humidity of 60%.

In the four years of exposure, the CHORUS emulsions have recorded about 800,000 neutrino charged current interactions.

## 2.3 Scintillating fibre tracker

The scintillating fibre tracker [60, 61, 62] provides tracking and vertex reconstruction, with the accuracy needed for the extrapolation of tracks to the upstream interface sheet. When a charged particle crosses a scintillating fibre, photons are emitted in the fibre, which are collected and sent to photomultipliers and then to an optoelectronic chain capable to read the signal.

The target tracker is composed by eight modules, the first one positioned downstream the first emulsion stack, and the following three modules downstream the second stack. The structure, as shown in figure 2.4, is then repeated for the remaining four planes. The 40 mm distance of a stack from the downstream tracker plane optimizes the upward extrapolation, yet mantaining a good track separation. Every module is furter composed of four planes, oriented in the $x$, $z$, $x^{\pm}$, $z^{\pm}$ projections, the latters being rotated of $\pm 8°$, to eliminte ambiguities on the tridimentional track reconstruction.

A plane is made of seven staggered layers of scintillating fibres, each fibre having a diameter of 500 $\mu$m for a total thickness of 3.2 mm. The fibres are glued with a $TiO_2$ based paint which also reduces cross talk.

The readout of the half million of fibres is made coupling ribbons of fibres to image intenifiers read by CCD cameras, that compose the optoelectronic readout system which translates the light signal into an electric one.

An overall resolution of 150 $\mu$m in position and of 2.5 mrad in angle is reached on the prediction to changeable sheets.

## 2.4 Magnetic spectrometer

Downstream the target area is the magnetic spectrometer, which measures charge and momentum of particles up to 20 GeV before they reach the calorimeter. After its hexagonal shape, the hadron spectrometer is also called diamond tracker (DT).

The setup of the hadron spectrometer consists of an air core magnet, preceded and followed by tracking elements in order to reconstruct the curvature of the track induced by the magnetic field. Upstream the magnet are scintillating fibre planes, while downstream again fibre planes and another tracking module, which consisted in streamer tube planes in 1994-1995, and was replaced in 1996 by three honeycomb tracker chambers.

The setup is studied to avoid interactions of the magnetic parts of the detector with the optoelectronic chains that read the fibres, to let hadrons cross the smallest amount of material as possible before they reach the calorimeter, and finally to mantain the best geometrical acceptance of calorimeter and muon spectrometer. An air core hexagonal magnet [63] is used, showed in figure 2.5, composed of six triangular elements with edges of 1.5 m and 0.75 m deep. The edges of the triangles are covered by aluminium coils in which current is pulsed with the same time structure as for the beam, creating a magnetic field of 0.12 T, parallel to the external edge and independent on the distance from the centre. The material is in total equivalent to less than 4% of a radiation length, but the six spokes of the magnet represent a dead area for the momentum reconstruction, which concerns about the 15% of the tracks reaching the magnet.

The track reconstruction is done in three modules of scintillating fibres equal to those composing the target tracker. The modules have the same hexagonal shape of the magnet, and the first one is positioned upstream the magnet while the remaining two are downstream. Each module is composed of two planes, formed by three rhombi of fibres oriented with a difference of 120°, and the two planes are rotated by 60° with respect to each other, to always allow the measurement of a coordinate and of its complementary. A module is shown in figures 2.5.a and 2.5.b.

In the original setup, modules of streamer tubes followed the last fibre planes. In 1996 they were replaced by three honeycomb chamber planes [64], mounted at 60°, 0° and 120° respectively, consisting of six planes staggered to minimize the inefficiency due to the dead area between the cells.

For the discussion of the hadron spectrometer resolution, see section 2.8.

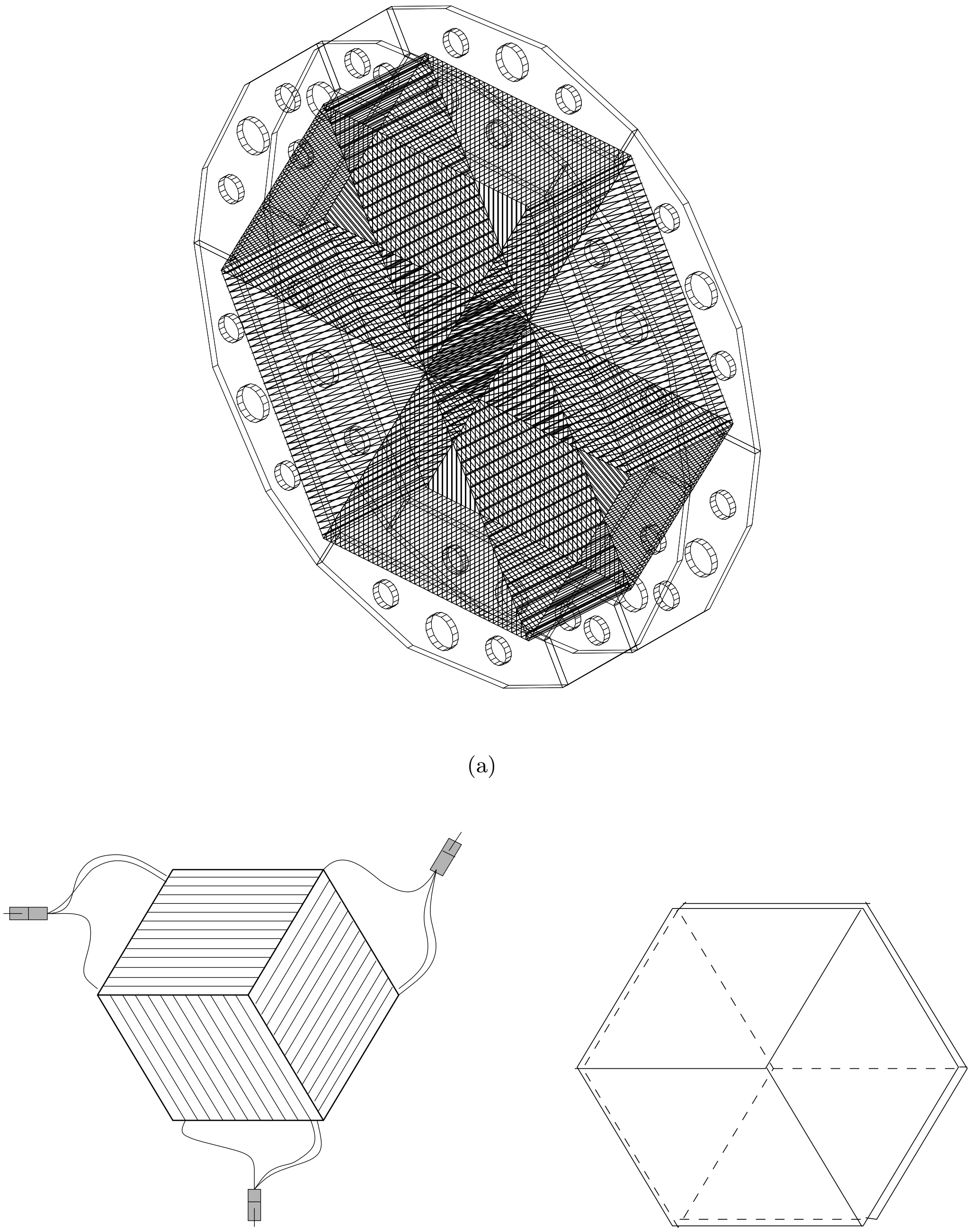

(a)

(b)

(c)

Figure 2.5 – (a) the magnet of the hadron spectrometer; (b) one module of the hadron spectrometer; (c) the disposition of the two planes in the module.

## 2.5 Calorimeter

The calorimeter [65] is designed to have a high resolution on angle and energy of hadronic showers and to be able to track muons. This is achieved with planes of lead and scintillator modules with high segmentation (the width of a module must be smaller than the average extention of a hadronic shower) interleaved with streamer tubes that provide the desired tracking capability. A module is a bar of lead and scintillator with a lead to fibre ratio 4 : 1 to have compensation and hence good resolution on hadronic shower, with scintillators read at both sides by photomultipliers.

The calorimeter is divided in three sections, of decreasing granularity, called EM, HAD1 and HAD2. The total depth corresponds to 144 radiation lengths and 5.2 interaction lengths, thus 99% of a shower from a 5 GeV pion is contained. A side view of the calorimeter is in figure 2.6.

EM and HAD1 are built with the "spaghetti" technique developed by the LAA-SPACAL collaboration [66], i.e. with the scintillating fibres positioned in the grooves of an extruded layer of lead. The diameter of the groove is 1.1 mm and the thickness of the layer is 1.9 mm. The planes are alternatively oriented in the two direction ortogonal to the beam direction, to provide angular meaurement of the showers.

EM is made by four planes of 31 modules each, and contains in total 740 fibres. Each module is composed by 21 layers with a longitudinal dimension of 2.62 m and a thickness of 82.4 mm. The total thickness of the EM section corresponds to about 20 radiation lengths, sufficient to contain the longitudinal extention of an electromagnetic shower. HAD1 is composed of five planes, each containing 40 modules, 3.35 m long. There are in total 1,554 fibres. HAD2 is also composed by five planes, each formed by 19 modules 3.69 m long. A module contains five 200 × 16 mm$^2$ lead layers, alterned to scintillator planes with transverse dimensions 200 × 4 mm$^2$.

The intrinsic performance of the calorimeter was determined with various test beams of electrons and pions of well defined energy, ranging from 2.5 to 10 GeV for electrons and from 3 to 20 GeV for pions [67]. The energy resolution for electrons is

$$\frac{\sigma(E)}{E} = \frac{(13.8 \pm 0.9)\%}{\sqrt{E(\mathrm{GeV})}} + (-0.2 \pm 0.4)\% \tag{2.1}$$

while for pions

$$\frac{\sigma(E)}{E} = \frac{(32.3 \pm 2.4)\%}{\sqrt{E(\mathrm{GeV})}} + (1.4 \pm 0.7)\% \tag{2.2}$$

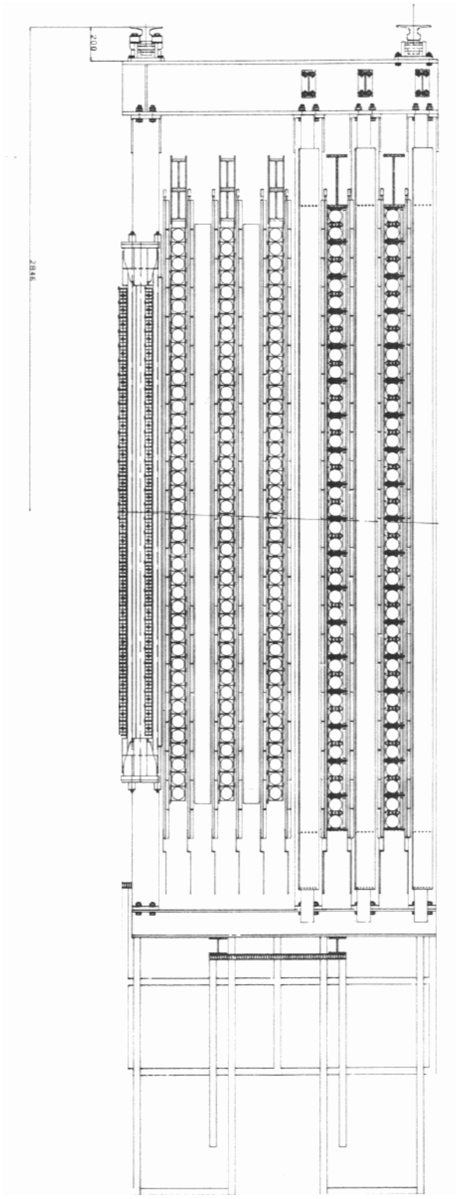

Figure 2.6 – Side view of the calorimeter.

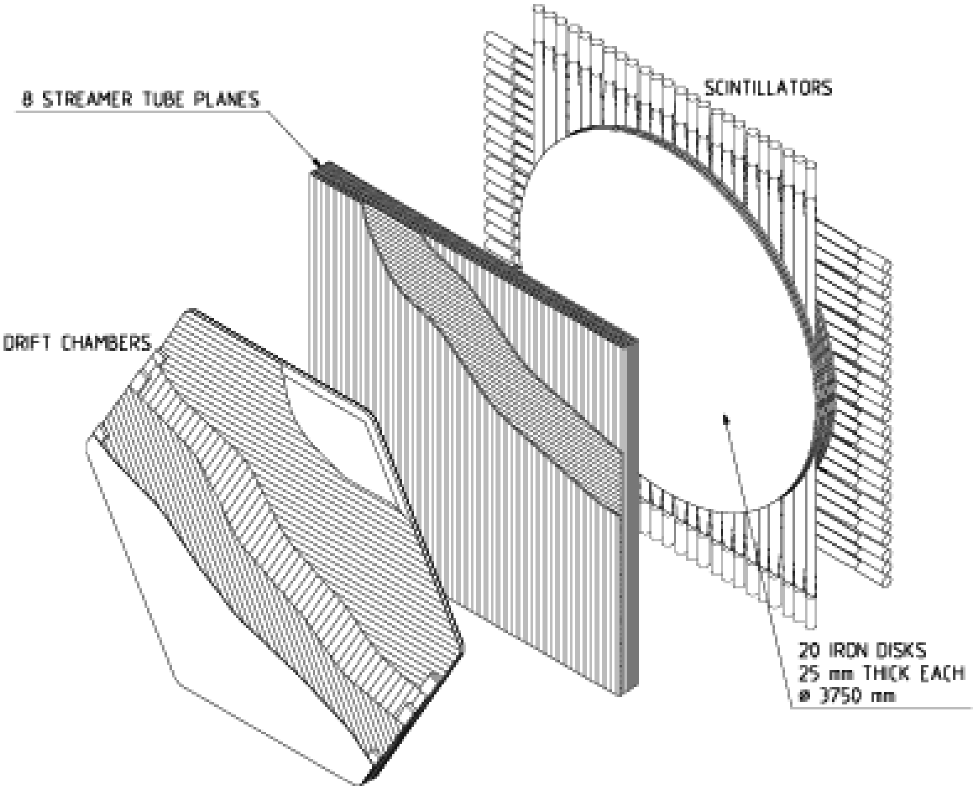

Figure 2.7 – Components of the muon spectrometer.

## 2.6 Muon spectrometer

The “end system” is a muon spectrometer, which identifies muons and determines their charge and momentum. Other particles from neutrino interactions are in general filtered by the calorimeter.

The spectrometer was inherited from CDHS, and is composed by seven tracking modules formed of drift chambers and streamer tubes, interleaved to six toroidal modules of magnetized iron that yield the change of trajectory of charged particles. The components are shown in figure 2.7.

The seven drift chambers consist of three hexagonal drift planes oriented at 60° with respect to each other. The chambers are filled with a 60% Argon - 40% Ethane mixture.

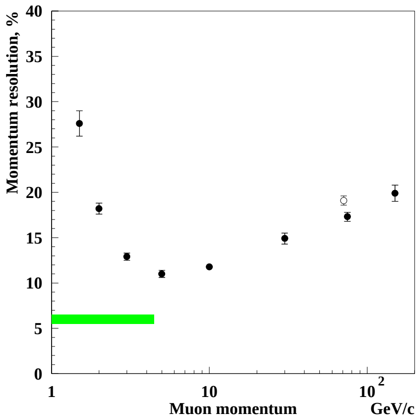

Figure 2.8 – Momentum resolution of the muon spectrometer. The empty dot represents the 71 GeV test beam result. The black dots come from the Monte Carlo simulation.

Each plane contains 62 parallel 3.57 m long wires having a diameter of 40 $\mu$m, separated by 6 cm and interleaved with cathode wires. The drift chamber resolution on a hit is about 1 mm, the efficiency per plane being better than 99%.

Downstream the drift chambers are stacks of eight limited streamer tube planes, which measure track segments in the gaps and eliminate the 20% of unresolved right-left ambiguities left by the drift chambers. The planes consist of 352 streamer tubes and have an active area of 3.76 × 3.76 $m^2$.

The magnets, weighting about 43 tons each, are composed by twenty iron disks of 2.5 cm thickness, having an outer diameter of 3.75 m. The disks are interleaved to 0.5 cm thick scintillator planes which are inserted in the 0.6 cm gaps. Each disk has a hole in the centre to allow the rolling of the coil that magnetize the iron. The resulting field is symmetric for azymuthal angle and amounts to about 2 T.

The momentum resolution was measured with a test beam for muons of 72 GeV and is about 19%, while at lower energies it was derived by means of a Monte Carlo simulation, and is about 15% for 20 GeV muons. The resolution curve is shown in figure 2.8.

## 2.7 Trigger system

The trigger is obtained by combining the signal of plastic scintillator bars surrounding the emulsion target. The hodoscopes composing the trigger [68] are labelled as E, T, H, V, A,

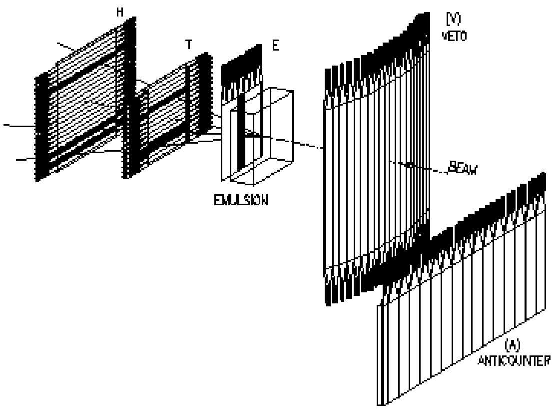

Figure 2.9 – Layout of the trigger.

as shown in figure 2.9, and are used to select the events in which a neutrino interaction took place and reject the background of cosmic rays and passing through muons coming from the beam.

The main trigger is for neutrino interactions in emulsion, and is defined by a cohincidence of signals in E, T, H compatible with a trajectory at an angle smaller than 180 mrad with respect to the beam line, together with the presence of energy release in calorimeter and/or spectrometer, and the absence of a veto signal. The latter consists in a combination of signals in V, A, T with a time structure optimized to avoid the rejection of neutrino events with back scattering.

The trigger efficiency is about 90% for neutral current interactions, i.e. when no muon is present, and raises to 99% for charged current events. About 50% of events labelled by an emulsion trigger actually originates in emulsion: the remaining fraction consists in interactions in the other massive parts of the target area, such as the scintillating fibre planes, or in the surrounding material like floor, walls, etc. These events are of course excluded from the sample.

## 2.8 Resolution on hadron momentum

The hadron spectrometer (DT), whose setup was described in section 2.4, measures momenta of charged hadrons before their absorbtion in the calorimeter.

Basically, the momentum measurement is done comparing the slope of a track measured in the fibre tracker planes upstream the magnet with the slope measured in the planes downstream. However, for the alignment of the subdetector and for identification of tracks also the information coming from the upstream target tracker planes is used, as well as that of the set of wire chambers positioned downstream (this consisted in streamer tubes in 1994 and 1995, and in honeycomb chambers in 1996 ad 1997).

From design, the momentum resolution was quoted as [69]

$$\frac{\sigma(p)}{p} = \sqrt{0.21^2 + (0.033 \cdot p)^2} \tag{2.3}$$

but this is just a nominal resolution, which holds only in the hypothesis of perfectly reconstructed tracks and no deterioration of the measurement coming from a non perfect alignment.

The actual DT resolution is in fact poorer, and we have studied it separating the samples of the different years of data taking, because of the changements in the setup of the sudetector and because different periods refer to different alignments.

The hadron spectrometer resolution can be measured from data, considering muon tracks and comparing the momentum measured by the DT with that measured by the muon spectrometer. We applied this method to four samples of neutrino triggers taken in the years that go from 1994 to 1997.

The resolution was measured comparing the DT reconstructed momentum $p_{\mathrm{DT}}$ with $p_{\mathrm{SPEC}}$, where $p_{\mathrm{SPEC}}$ denotes the track's spectrometer momentum corrected for the energy loss in calorimeter (1.7 GeV on average); the spectrometer resolution was assumed to be 16% [70] and was unfolded from the DT one.

Events having vertex inside the emulsion stacks and one $\mu^{\pm}$ track in the spectrometer were selected, provided that the spectrometer track was matched with a DT track not crossing any iron spoke of the air core magnet, in order to avoid uncontrolled multiple scattering corruption of the momentum measurement. Some purity and reliability cuts were applied on the tracks:

the number of combinations of hits among which the muon matching DT track was chosen must be less than 20. This reflects in the fact that a reasonable number of hits was recorded in the fibre tracker planes, i.e. that the event is sufficiently clean;

the fit probability for the selected DT track must be greater than 0.5%, in order to limit the analysis only to reliable tracks;

at least 5 paddles must be crossed out of a maximum of six. This is again to be sure that the DT track that we want to compare with the muon spectrometer one is not a fake track.

Table 2.2 contains the number of events surviving the selection described, together with the final efficiency $\varepsilon_{\mathrm{DT}}$, defined as the number of tracks surviving all the cuts over the total number of $\mu$ tracks with vertex in emulsion.

| **Year** | **1994** | **1995** | **1996** | **1997** |
|---|---|---|---|---|
| **Original sample:** | | | | |
| 1 $\mu$ track + vertex in emulsion | 24,112 | 24,523 | 30,404 | 31,487 |
| **Track selection:** | | | | |
| 1 end system matched $\mu$ + no spoke crossed | 12,907 | 14,987 | 16,528 | 16,573 |
| $N_{comb} < 20$ | 10,034 | 11,083 | 12,151 | 12,128 |
| $P_{fit} > 0.005$ | 9,703 | 10,802 | 11,772 | 11,041 |
| at least 5 paddles hit | 7,353 | 8,607 | 9,318 | 6,207 |
| $\varepsilon_{\mathrm{DT}}$ | **30%** | **35%** | **31%** | **20%** |

TABLE 2.2 – Details of efficiencies of the hadron spectrometer in the four years of data taking. The numbers reported refer to the events that survive each cut. The efficiency $\varepsilon_{\mathrm{DT}}$ is obtained normalizing the final number of events after all cuts to the number of events with vertex in emulsion and one $\mu$ track present.

This "efficiency" actually is the product of the hadron spectrometer's acceptance times the efficiency of the selections on tracks described above. This number is around 32% with our selections which are quite severe, because for our study we need a clean sample of tracks. The 1997 data showed up to have a problem, since $\varepsilon_{\mathrm{DT}}$ decreases down to 20%.

Figure 2.10 then shows the distributions of the $\chi^2$ associated to the fit of the track parameters. The shapes of the first three $\chi^2$ probability distributions, which show a peak

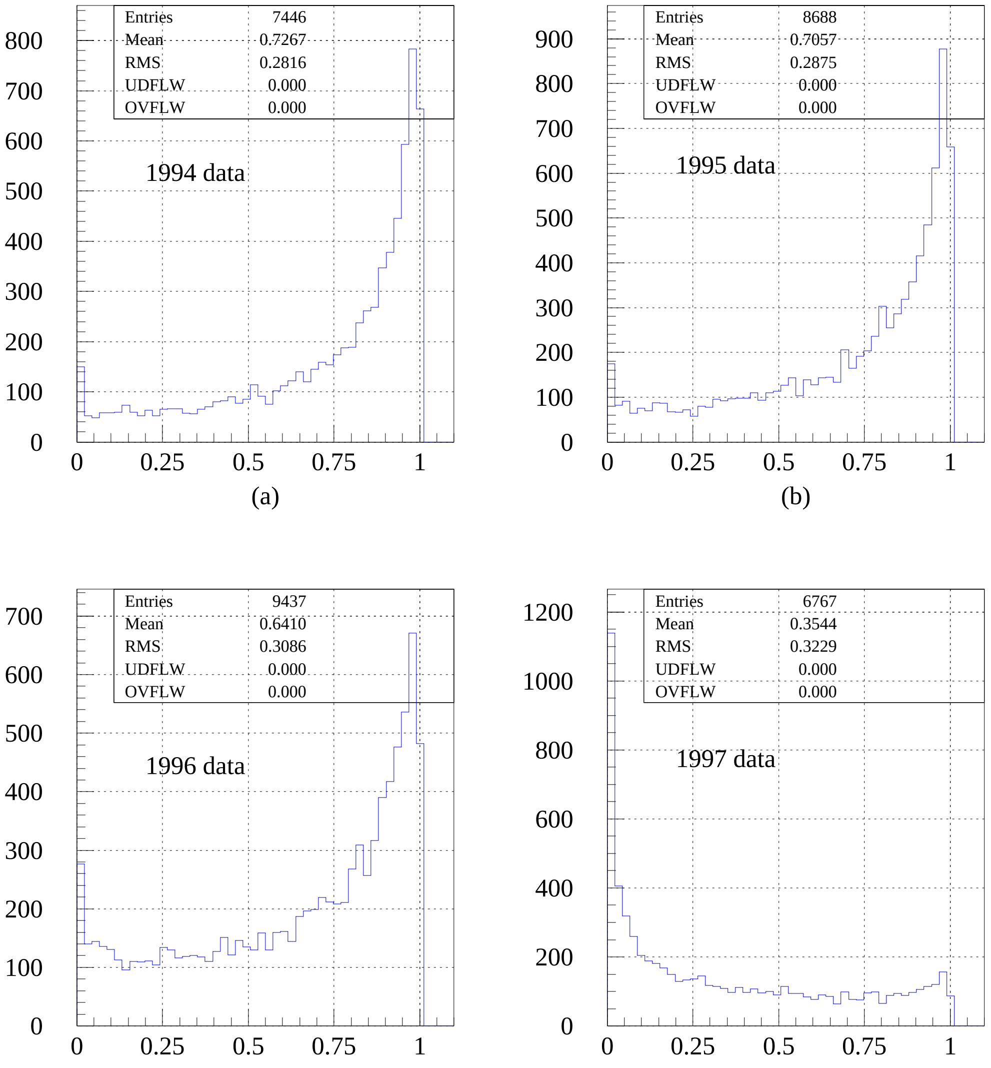

(a) (b)

(c) (d)

FIGURE 2.10 – $\chi^2$ probability for the selected tracks in the four years (a) 1994, (b) 1995, (c) 1996 and (d) 1997.

close to 1, can indicate a general overestimation of the errors. However, these distribustions are reasonably flat far from 1, so that it is possible in any case to distinguish the peak at 0, and to evaluate the number of wrong associations, which is always reasonably small.

The distribution for 1997 data looks again different. The fact that the peak at 1 is not present any more, together with the degradation of the resolution, suggests the existence of an alignment problem in some part of the detector, which could artificially enhance the measurement errors, partially absorbing the overestimation. The large peak near 0 (see plot 2.10.d) also goes in this direction.

Finally, we computed the momentum resolution performing a gaussian fit to the distributions of $(1/p_{\mathrm{DT}} - 1/p_{\mathrm{SPEC}})/(1/p_{\mathrm{SPEC}})$, plotted for different intervals of $p_{\mathrm{SPEC}}$ values. In figure 2.11 we show the $\sigma$'s of the distributions as determined by the fit (the figures also show the RMS of each distirbution, to evidentiate, by the similarity between RMS and $\sigma$, that the original distributions do not have long non gaussian tails).

The $\sigma$'s represent the combined resolution of the DT and the muon spectrometer. Unfolding the spectrometer resolution and fitting the $\sigma$'s with the function

$$\sigma(p)/p = \sqrt{\alpha^2 + (\beta \times p)^2} \tag{2.4}$$

we get for $\alpha$ and $\beta$ the values reported in table 2.3.

| **Year** | **1994** | **1995** | **1996** | **1997** |
|---|---|---|---|---|
| $\alpha$ | $0.36 \pm 0.02$ | $0.29 \pm 0.02$ | $0.36 \pm 0.02$ | $0.40 \pm 0.04$ |
| $\beta$ | $0.032 \pm 0.002$ | $0.040 \pm 0.002$ | $0.039 \pm 0.002$ | $0.073 \pm 0.004$ |

TABLE 2.3 – Summary of resolutions ($\sigma(p)/p = \sqrt{\alpha^2 + (\beta \times p)^2}$).

The results of table 2.3 show that the resolution for the years 1994, 1995, 1996 is worse than the "ideal" value given in equation 2.3 (e.g. the error on a 5 GeV momentum is about 38% instead of 27%). This is partly expected because the ideal value does not take into account the accuracy of the detector alignment, and makes use of the nominal resolution of the tracking detectors. Even worst is the resolution for the 1997 data, which already showed the problems mentioned above.

As a consequence of these measurements, the alignment procedure used for the 1997 data was checked, and a technical problem identified and solved. Moreover, a complete

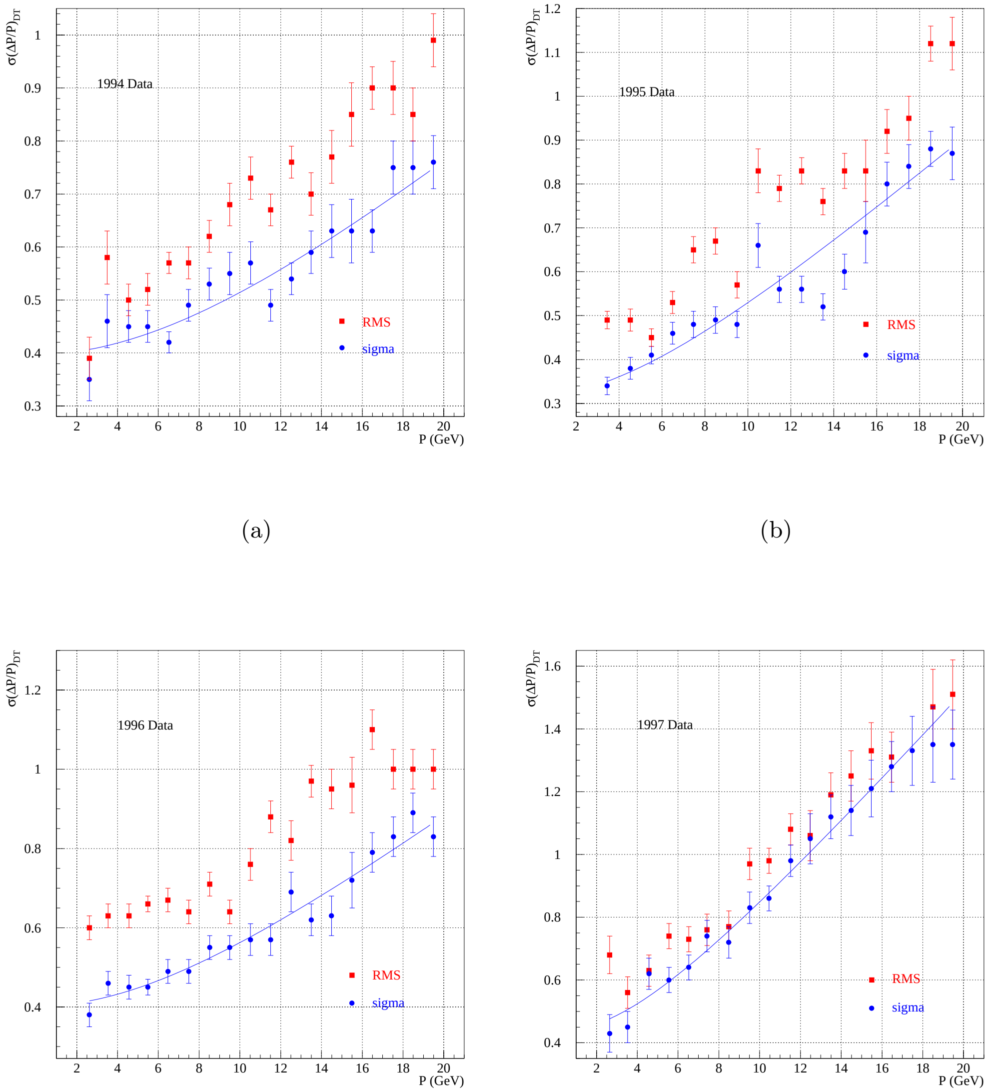

(a) (b)

(c) (d)

Figure 2.11 – DT momentum resolution for $\mu$ tracks for the four sets of data: *(a)* 1994; *(b)* 1995; *(c)* 1996; *(d)* 1997. Dots: sigma of the distribution of $(1/p_{\rm DT} - 1/p_{\rm SPEC})/(1/p_{\rm SPEC})$ in bins of $p_{\rm SPEC}$; boxes: RMS of the same distributions. The points represent the combined resolutions of DT and muon spectrometer.

revision of the alignment software has been started by the groups responsible for the various subdetectors.

The momentum resolution has definetly been improved (say, $\sigma(p)/p \sim 30\%$ at 5 Gev), although we do not quote a comprehensive result because few improvements are still being made.

As a final remark, we note that the performances of the hadron spectrometer are good enough to isolate a large sample of events with a $\pi^-$ in the $1 - 10$ GeV energy range (and no muon). This sample has been used in the oscillation search, to look for events with a $\tau \rightarrow h^- X$ decay. For charm physics however, little help is obtained from the hadron spectrometer. The chances of reconstructing the decay product of a charmed particle are affected by the limited geometrical acceptance of the spectrometer, by the difficulty of reconstructing the track before and after the magnet, and by the lack of identification and measurement of neutrals. No attempt has then been made to use the hadron spectrometer information in the analysis of the charm data discussed in this thesis.

# Chapter 3

# Netscan

Emulsion experiments have the great advantage in charm physics, with respect to dimuon experiments, that they can identify directly the charm, being able to see the decay vertex, because the micron resolution of the emulsion allows the detection of track lengths of the order of 1 mm. Thus the analysis is not limited to a particular decay channel of the $c$ quark, the information on the kind of hadron produced is much richer, and moreover the large background coming from non charmed hadron decays, which partly limits the sensitivity of non emulsion experiments, can be easily eliminated. On the other hand, the handicap has always been the huge emulsion scanning load, which translates into high expense of time and manpower, that would accompany the request of high statistics.

CHORUS has now the possibility to become the first emulsion high statistics experiment of neutrino charm physics, thanks to the very high scanning performance reached on the hardware side, and to the developement of a new method, the “netscan”, for fast emulsion scanning and decay search. This is one of the aims of the CHORUS phase 2 of analysis.

The netscan technique was developed in Nagoya University originally for the DONUT experiment at Fermilab. The main feature of netscan is that all track segments within a fixed volume centred on the vertex position are picked up. The automatic scanning technique, developed by CHORUS for the oscillation search, is based on an extremely fast automatic follow back in emulsion of a track reconstructed by the electronic detectors. In the oscillation search, the scan back track is candidate for being the decay product of the $\tau$, and it is traced back to the neutrino interaction vertex. Then, further measurements are made to search for the presence of a $\tau$ decay vertex.

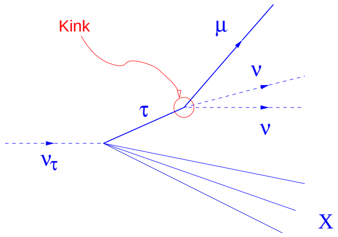

Figure 3.1 – The kink topology for a $\tau$ decay into muon.

The netscan technique extends the automatic scan to a full inspection of the emulsion volume surrounding the interaction vertex. The events which are analysed are those for which a neutrino interaction vertex has been located using the scan back track technique. A 15 $mm^3$ volume around the interaction vertex is then defined, and all track elements in that volume are electronically measured. Then, by softaware, the reconstruction of the full event topology can be performed.

In four years of data taking CHORUS has collected about 200 times the E531 statistics, by increasing both the target mass (0.8 tons of emulsion) and the integrated neutrino flux. Given the complexity of the automatic scanning technique, its overall efficiency is definitely lower than that of the manual scanning performed by E531. Nevertheless, it is expected that the final charm sample collected with the netscan technique will be more than 10 times larger than that of E531.

In this chapter, the main features of netscan are described. The chapter is organized as follows: first, the procedure that leads to the primary vertex location, needed by netscan, is described. Then the netscan procedure is described in detail, for what concerns the hardware and the data acquisition. The event reconstruction software is described in section 3.2.2. After tracking, an offline selection for charm events is applied: this is described in section 3.3. Events passing the selection are checked by eye, so this procedure is described in section 3.4. Finally, the efficiencies are estimated.

## 3.1 Event location

The netscan is performed on *located* events, i.e. events in which the primary vertex position was found. CHORUS has just finished a first phase of data analysis searching for $\nu_\mu \to \nu_\tau$

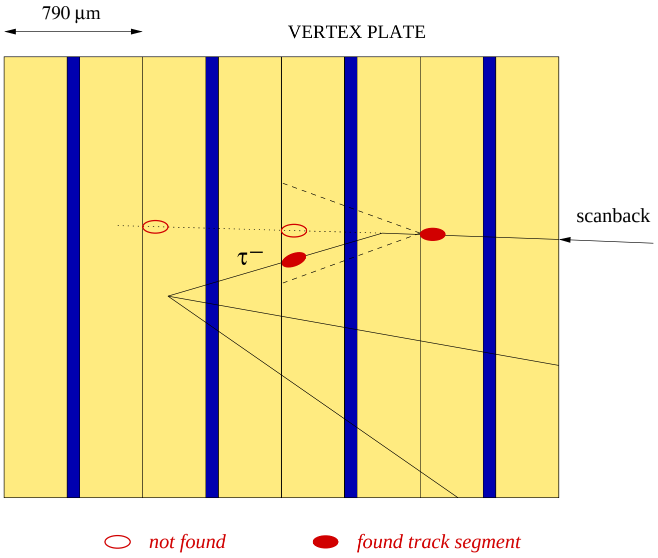

FIGURE 3.2 – The scan back procedure to search for vertex plate and kink.

oscillations (without finding any evidence). The searched signal was represented by the observation of the decay of the $\tau$ produced in a $\nu_\tau$ interaction. The characteristic topology of the $\tau$ decay in one prong is the *kink*, i.e. a change of the track direction that indicates the decay point (see figure 3.1).

The emulsion scanning was based on the selection of a track candidate which was followed up to bulk emulsion until the vertex plate, indicated by the disappearance of the track, was found (see figure 3.2). This procedure, fully automated, is called *scan back* and is performed by a hardware video image processor interfaced to a microscope through a CCD camera, the Track Selector, whose evolution, described in section 3.2.1, is now used for netscan.

The CHORUS sample is divided in two sets, according to the two decay modes that were used for the $\tau$ search: events containing a negative muon ($1\mu$) and events without muon ($0\mu$). In the $1\mu$ sample, the negative muon was selected as a scan back track, while in the $0\mu$ case, one or more negative hadrons were used. The scan back was then performed on events reconstructed by the fibre tracker with vertex predicted in bulk emulsion.

Our analysis concerns charm production in neutrino charged current interaction, thus we focus on events with a muon: a $1\mu$ event is then sent to the scan back if the $\mu^-$ has a momentum below 30 GeV, and if the angle that the muon forms with the beam direction is less than 400 mrad. The 30 GeV cut was applied to reduce the scanning load, and has the effect to reject about 30% of $\nu_\mu$ charged current interactions, but less that 15% of $\tau$ muonic decays: in fact, a muon from $\tau$ decay roughly carries one third of the $\tau$ energy and is then expected to have lower energy than muons produced in $\nu_\mu$ interactions. The effect on the oscillation sensitivity is even less important, because at high momenta the kink angle is on average small thus difficult to detect in any case. The angular cut is due to the limited efficiency of the Track Selector at higher angles.

The scan back is a very complex procedure. The automatic search of a track in the target emulsion has to be limited to very small areas ($\sim 1$ mm$^2$) and to a small angular range (a few mrad), because a huge amount of background tracks is present in the emulsion. This is essentially due to the fact that the exposure of the emulsions last for 1 or 2 years and hence all particles traversing the emulsion in that period are stored. The scan back then consists in the follow up of the selected track to changeable sheet, using the slopes measured by the scintillating fibre trackers. Then if the track is found in changeable sheet, the parameters are measured with higher precision and the track is searched for in special sheet. Again, if it is found, the track is followed up to bulk, plate by plate (only the most upstram 100 $\mu$m are scanned) until it disappears in two consecutive plates: this determines the vertex plate.

Located events have then been analysed with many different techniques, searching for $\tau$ decays. The same events are now being fully analysed with the netscan technique described in detail in the following sections. The present plan is to complete by middle 2002 the measurement of the sample of 143,742 $1\mu$ located events. In chapter 4 we shall present a preliminary analysis based on a subset of 27,073 events. Note that at the same time, the CHORUS collaboration is also maeasuring with the scan back technique a fraction of the $1\mu$ events with $p_\mu > 30$ GeV (previously discarded) and analysing with netscan the $0\mu$ located events.

## 3.2 Netscan technique

### 3.2.1 Data acquisition

The basic idea of the automatic emulsion scanning is to transform the three-dimensional information contained in the emulsion volume, into many tomographical images – given

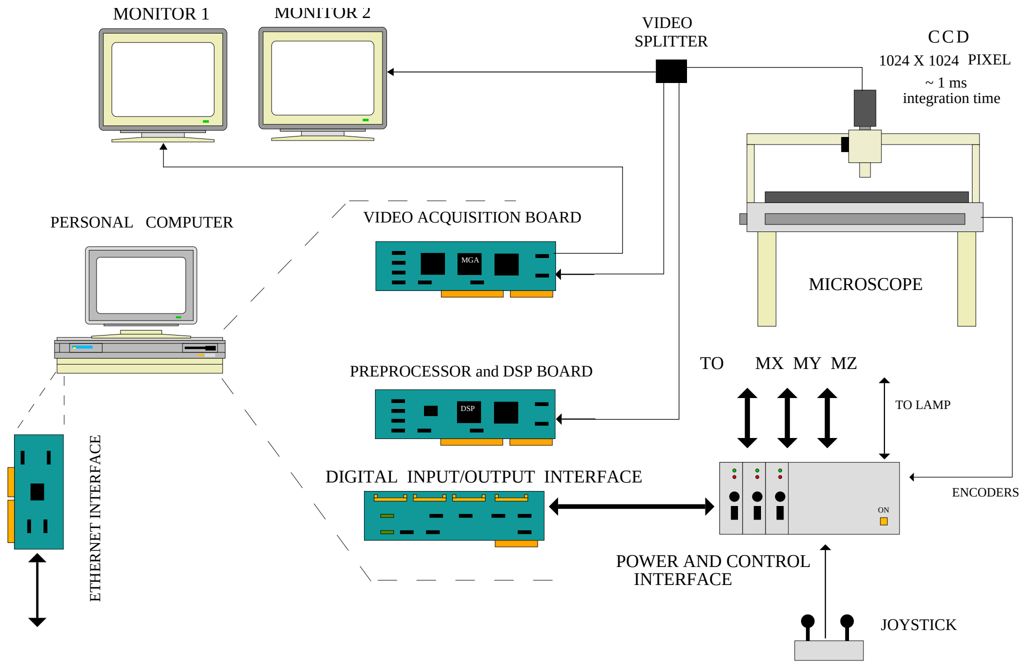

FIGURE 3.3 – Schematic view of the components of the automatic scanning system.

by the interplay of a microscope and a CCD camera – taken at different focal depths.

The automatic scanning in CHORUS is performed by a computer controlled microscope of 3 $\mu$m focal depth, whose view is sent to the Track Selector [71], a hardware video image processor composed of a Fast Programmable Gate Array, a Fast Memory and a grabber board connected to a CCD camera of 512 × 512 pixels at 120 Hz frame rate. The actual view corresponds to 150 × 150 $\mu m^2$ and is determined by the microscope's optics. The system is schematized in figure 3.3.

In the scan back data taking, the most upstream 100 $\mu$m of the plate are ideally subdivided in 16 slices, which correspond to different focal depths of the microscope. Correspondingly, 16 tomographic images are taken in the most upstream 3 $\mu$m of each slice and digitized, then shifted orizontally with respect to the first layer, according to the angle predicted by the special sheet. The track is identified as a peak in the pulse height: this can range from 1 to 16, since each frame can give 1, if a track segment over the fixed grayscale threshold is found therein, or 0 otherwise. An example is shown in figure 3.4.

A threshold at a pulse height of 12 is set to accept a track: this on one hand introduces

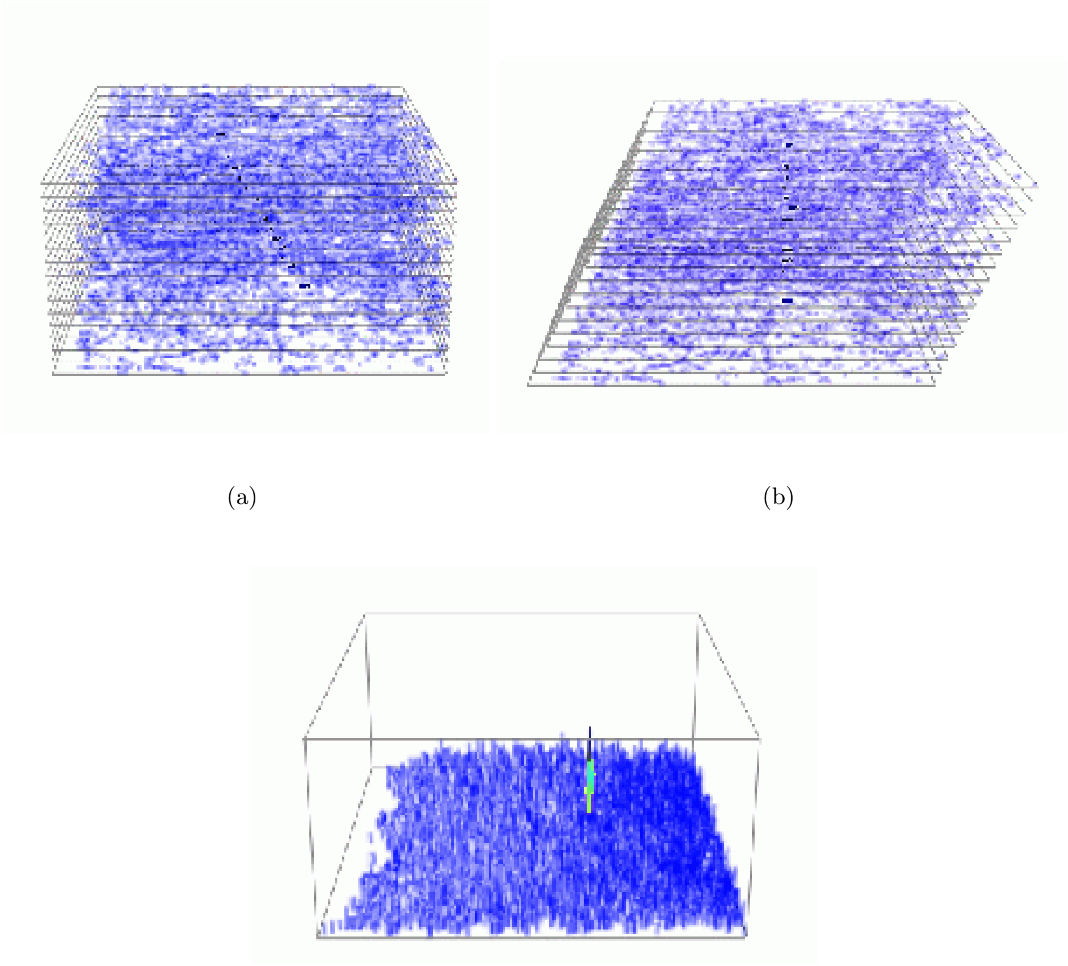

(a)

(b)

(c)

Figure 3.4 – How the Track Selector works. (a) A 100 $\mu$m thick emulsion volume is divided in 16 frames and scanned in the most upstream 3 $\mu$m of each frame. The hidden track is marked in black. (b) The 16 frames are shifted according to the predicted angle. (c) Projecting all the shifted frames, the track is found as a peak of pulse height.

an inefficiency mostly for large angle tracks, but also rejects random coincidences. Table 3.1 shows the Track Selector efficiency in various angle ranges when the pulse height threshold is set.

| Angle range [mrad] | Efficiency |
|---|---|
| 0 – 50 | $(99.7 \pm 0.1)\%$ |
| 50 – 150 | $(98.6 \pm 0.2)\%$ |
| 150 – 250 | $(90.8 \pm 0.4)\%$ |
| 250 – 350 | $(85.6 \pm 0.6)\%$ |
| 350 – 450 | $(62.9 \pm 0.9)\%$ |

TABLE 3.1 – Track selector efficiency for different ranges of angle.

The efficiences were measured considering three consecutive plates, with no track segment found in the middle one and signal in the side ones, and checking manually if the segment missed by the TS was actually present. This was repeated for sets of tracks subdiveded by angle.

There are two main reasons why the tracking efficiency decreases with increasing track angles: the first is the shift of the sixteen emulsion slices that the TS performs to identify the track, according to its predicted angle: in the extreme case of 0° angle, there is no shift at all, so that no mistake can occurr; in the opposit extreme case of 90° track, the shift would be infinite. In intermediate situations, the bigger is the track angle, the larger is the absolute error on the TS shift, which translates in a reduced visibility of the track in emulsion. Moreover, considering a “vertical” track, this will appear as a series of very dark, round grains, while a track with a non zero angle will appear as a more extended and faded object, with on average a larger fraction of track segments under greyscale threshold.

The last generation of track selectors, the UTS, allows the analysis of 1 $\text{cm}^2$/hour, and is expected to increase shortly to 10 $\text{cm}^2$/hour. This capability of very fast frame acquisition and analysis allows to use the netscan technique which is going to be described in what follows.

As mentioned, the events located with the scan back method are inherited by netscan and used as a prediction of the vertex position. The netscan data acquisition is performed by the same instrument as for scan back, but a much larger area is scanned, with a large angular acceptance, and no angular prediction from electronic detectors.

A volume of 1.5 mm × 1.5 mm × 6.32 mm is considered. The longitudinal dimension corresponds to 8 plates: in fact the vertex plate, 1 plate upstream and 6 plates downstream are scanned. The volume is optimized to search for secondary vertices of $\tau$ or charm, which both have an average decay length of 1 mm.

The scanning centre position on the vertex plate is calculated assuming that the primary vertex is in the middle of the plate: if $\left(y^{\text{last}}, z^{\text{last}}\right)$ are the coordinates of the most upstream measured point in scan back location, the centre of the netscan volume on the vertex plate is given by

$$\begin{aligned} y_{\text{C}}^{\text{vertex plate}} &= y^{\text{last}} - 440 \cdot a_y^{\text{scan back}} \\ z_{\text{C}}^{\text{vertex plate}} &= z^{\text{last}} - 440 \cdot a_z^{\text{scan back}} \end{aligned} \tag{3.1}$$

where $\left(a_y^{\text{scan back}}, a_z^{\text{scan back}}\right)$ are the slopes of the scan back track. Since the direction of the beam is $\left(\theta_y^{\text{beam}}, \theta_x^{\text{beam}}\right) = (0, 0.043)$, in the n-th plate the centre of the netscan volume is given by

$$\begin{aligned} y_{\text{C}}^{n} &= y_{\text{C}}^{\text{vertex plate}} \\ z_{\text{C}}^{n} &= z_{\text{C}}^{\text{vertex plate}} - 0.043 \cdot 790 \cdot (n - n_{\text{vertex}}) \end{aligned} \tag{3.2}$$

if $n_{\text{vertex}}$ is the ordinal number of the vertex plate. The netscan fiducial volume is shown in figure 3.5.

As for the scan back, sixteen tomographic images are taken in the most upstream 100 $\mu$m of each plate at different focal depths. The threshold on pulse height to retain a track segment is set to 10. All track segments, within the angular acceptance, in the fiducial volume are measured and stored. The angular acceptance is set to $-400 < \theta_{y,z} < 400$ mrad, where $\theta_y$ and $\theta_y$ are the angles between track and beam axis (conventinally taken as $x$) in the $\langle xy \rangle$ and $\langle xz \rangle$ planes. This is because of the decrease of efficiency of the UTS at larger angles. With the last version of the UTS, the netscanning of one event takes about 10 minutes.

### 3.2.2 Offline reconstruction

The raw data output of the UTS, corresponding to 1 event, occupy about 1.77 Mb, so that the database containing our 27,073 events has a size of about 48 Gb, and the management

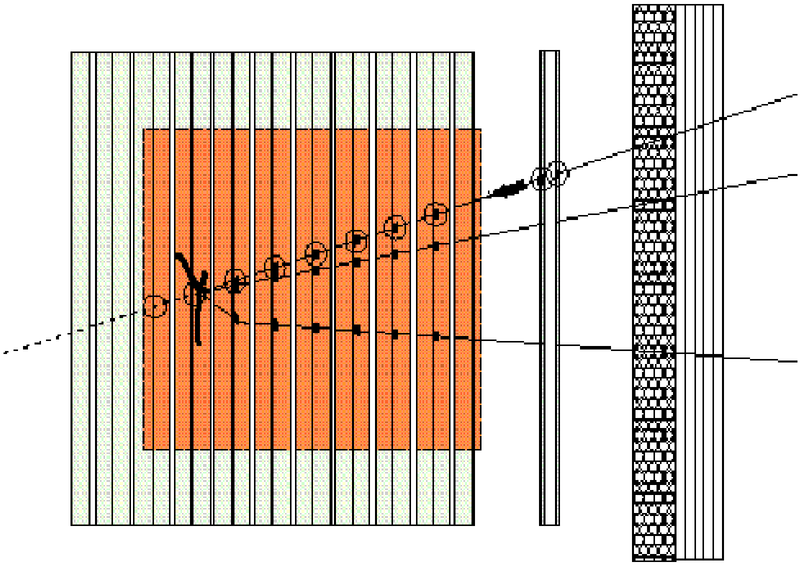

Figure 3.5 – Netscan fiducial volume (1.5 mm × 1.5 mm × 6.32 mm). The longitudinal dimension corresponds to 8 plates. The vertex plate, 1 plate upstream and 6 plates downstream are scanned.

is based on Objectivity. The raw segments undergo several operations, whose final aim is to have reconstructed tracks and vertices of the event. The offline reconstruction then consists in alignment, tracking and vertex finding. Since much of the digital information is in fact not associated to the event, also a heavy work of background rejection must be performed. The reconstruction program is written in C++ and is divided in two block: ECFSAL (Emulsion Chamber First Structure ALignment) which performs first alignment and tracking, and ECVTXA (Emulsion Chamber VeTeX Analysis) for background track rejection, fine alignment and vertex reconstruction.

### Alignment and tracking

Once the reliable track segments are selected on the basis of the pulse height cut off, “ghosts” must be rejected, i.e. copies of segments which are seen twice because they fell in the intersection zone of two microscope views. Then, if two segments having the same angle are found, whose distance is less than 5 $\mu$m, one is discarded.

After the segment selection, the recursive alignment-tracking program (ECFSAL) is run. It compares the pattern of segments in a plate to that in the following one to determine the position and rotation parameters of the plate to plate alignment.

The tracking consists in the extrapolation of the segments of the first plate to the following one, looking for a matching segment in a cone of angle dependent on the alignment residuals (20 mrad being the maximum angle), and in about 4 $\mu$m in position, corresponding to $3\sigma$ of alignment resolution. If no candidate is found, the starting segment is kept anyway, and the matching is tried in the further upstream plate. This means that gaps are allowed in the netscan tracks.

### Rejection of low momentum tracks and fine alignment

At the end of this first alignment-tracking process, on average 5,000 tracks are reconstructed in the fiducial volume (see figure 3.6 on the next page.a), but only a few of them are real event tracks. The most part are low momentum tracks coming from cosmic rays, radioactivity, low energy interactions of neutrals, accumulated during the years of emulsion exposure. It is then mandatory to eliminate as more background as possible, and then a second, *fine* alignment is performed once the event has been cleaned. This is done within the fine alignment-vertexing program (ECVTXA).

Tracks are obtained by the connection of several track segments, and the number of reconstructed tracks depends on the angular acceptance in the extrapolation from a segment to the following plate: the larger is the acceptance, the easier a segment will fall inside the solid angle. At the moment, in ECFSAL the tolerance is a floating value which depends on the plate alignment residuals: this means that low momentum tracks, that undergo large scattering, can appear splitted in track segments. Of course it would be easy to make them connected increasing the acceptance, but this can be risky because one could also attach event tracks to background tracks. It is then necessary to find a good balance between the level of misconnection introduced and the number of reconnected low momentum tracks. So, one fixes a minimum momentum $p$ and a maximum momentum $P$ for tracks to be reconnected, and the maximum misconnection $M$ that can be introduced. Given $p$, the actual misconnection $m$ is calculated randomly taking as an input the track density in the plate, and if it exceeds $M$, $p$ is increased until $m = M$, or until $m$ reaches the value for which $p = P$. At this point, the tracks which now result connected, are rejected as low momentum tracks. For our sample, the minimum momentum for tracks to be reconnected was fixed at 100 MeV.

After low momentum track rejection, a second, “fine” alignment is performed using informations from the surviving tracks, similar in procedure to the first level one. After the second alignment, the resolution is 0.5 $\mu$m in position and 2 mrad in angle.

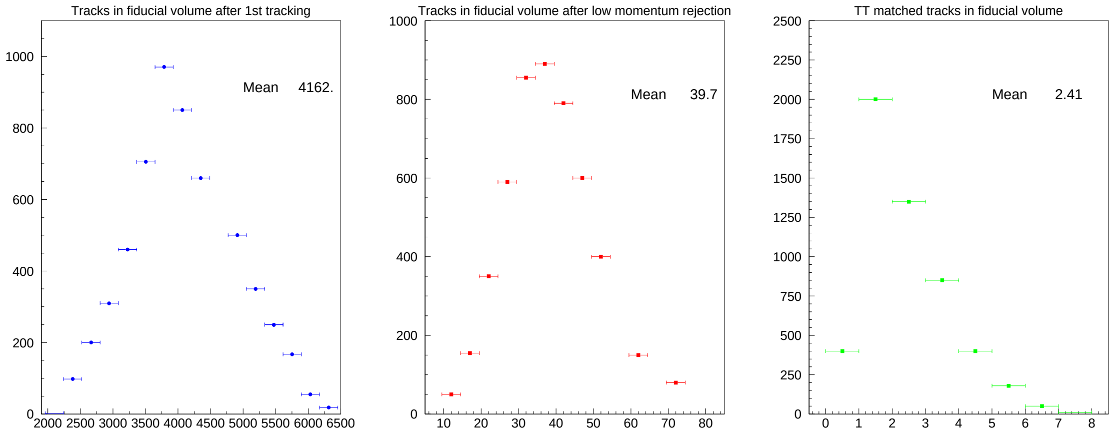

(a) (b) (c)

FIGURE 3.6 – (a) Number of tracks in fiducial volume after the first level alignment and tracking (ECFSAL). (b) At least two plate connected tracks stopping in fiducial volume after low momentum track rejection (ECVTXA). (c) TT matching tracks in fiducial volume that passed the cut on global angle.

### Vertex reconstruction

Before constructing the vertex, one must eliminate those tracks that belong to the event only because they happen to pass through the fiducial volume, but do not originate therein. These are mainly muons associated to the neutrino beam.

A track is defined to be a *stopping track* if it escapes the fiducial volume not more than once (no matter where, be it from the downstream face, or from the borders, or from the upstream face). All tracks which escape twice, are defined *passing through tracks*. After low momentum track rejection, on average 40 stopping tracks are found in the fiducial volume, as shown in figure 3.6.b for a sample of about $5,000$ events.

Most of the surviving tracks clearly are still background: in fact, they are originated from fragments of low momentum tracks that ECVTXA was not able to reconnect and eliminate. Completely isolated segments are eliminated. Still included are the fragments of low momentum tracks made of two (or more) connected segments: since the minimum number of connected segments necessary to form a standalone track is 2, that fragment of low momentum track is already considered a (stopping) track itself. One could increase the number of segments that form a track, but the price of this is a loss in tracking efficiency.

It was preferred to leave a bigger contamination but also higher efficiency, and use other methods to reject the background.

All the stopping tracks are used for construction of the vertices. First, tracks are considered two by two and two track vertices are constructed. The requirement for two tracks to form a vertex is that their distance is less than 20 $\mu$m. Also single segments can be reincluded, provided thay are matched at less than 30 mrad with a target tracker track, but at least one of the two tracks building the vertex must be connected in two plates. Two track vertices are then clusterized to form a real vertex, requesting that the distance between two tracks that form the two track vertices is less than 10 $\mu$m.

On average 3.9 vertices are reconstructed per event. At this level, no hypothesis is done on the reliability of the vertices. In the following we shall see that the validation of the target tracker is needed to discard fake vertices.

The output of ECFSAL and ECVTXA consists of segments, reconstructed tracks and vertices, and are again stored in the Objectivity database, in which an event occupies about 50 Kb.

## 3.3 Charm selection

The starting point for the charm search is the output of the reconstruction programs. The reconstruction steps described so far allow to reject 99% of background tracks in the event. Nevertheless, about 40 tracks survive on average, and most of them are still passing through or low momentum tracks, even if still not recognized as such. To define a good selection for charm events is a fundamental step for the study, and is still in evolution. Studies are under way to improve the purity of the selection (i.e. how many events among the selected ones actually contain a charm decay) together with the efficiency (i.e. how many of the produced charm are included in the selection). The selection that lead to the sample used in our analysis is described in what follows, and purity and efficiency are discussed. Nevertheless, possible improvements are under study, one of the aims being to have a purity high enough to avoid the manual check step, which, as we shall see, is still necessary up to now.

As mentioned, just looking at the results of the reconstruction programs, one cannot determine unambiguously the actual event topology. Thus, to perform the charm search avoiding the manual scanning of a huge amount of events, more stringent conditions must be applied in order to separate the “reliable” events from those in which fake tracks lead to the construction of fake vertices. Then, the characteristics topologies of charm decays

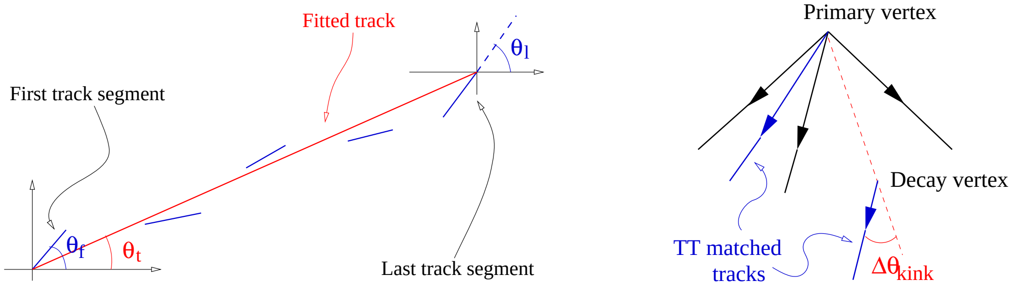

(a) (b)

FIGURE 3.7 – (a) Angles entering in the definition of $\theta_{\text{glob}}$. It is given by the difference between the angle of the fitted track $\theta_{\text{t}}$ and the square root of the sum of first ($\theta_{\text{f}}$) and last ($\theta_{\text{l}}$) segment's angles squared. (b) Definition of kink angle with respect to the line that links primary to decay vertex.

can be isolated.

### 3.3.1 An impact parameter based selection

A way to validate a netscan track is to check whether there is a correspondence with a track of the target tracker, i.e. the electronic detector downstream the emulsions. Also, more severe quality cuts can be applied, in order to further reject background tracks. Then it must be considered that in a charm event two vertices must be present, i.e. the neutrino interaction vertex and the charm decay vertex. Thus, the fundamental request of the selection is that two netscan TT matched tracks go to two distinct reconstructed vertices, provided that the tracks passed some quality cuts. In detail:

to eliminate the residual low momentum tracks it is requested that

$$\Delta\theta_{\text{glob}} < 2.31\sqrt{(0.00367)^2 + (0.0236 \cdot \theta_{\text{t}})^2} \quad \text{rad} \tag{3.3}$$

where $\Delta\theta_{\text{glob}}$ is the difference between the angle of the fitted track $\theta_{\text{t}}$ and the square root of the sum of first and last segment's angles squared (see figure 3.7.a). $\Delta\theta_{\text{glob}}$ is a measure of the multiple scattering, and for a 100 mrad track the threshold in equation 3.3 corresponds to about 10 mrad;

the event must contain at least two TT matched tracks, which have to be two plate connected, going to two distinct vertices (one can be just stopping, not associated to any vertex). The condition for TT matching is

$$\Delta\theta_{\mathrm{TT}} < 3.44\sqrt{(0.00546)^2 + (0.0194 \cdot \theta_{\mathrm{t}})^2} \quad \mathrm{rad} \tag{3.4}$$

This validates the primary vertex and assures that a second vertex (or a kink at least) is present. Again, for a 100 mrad track this corresponds to about 20 mrad;

the impact parameter of the stopping track and the non associated vertex must satisfy the angle dependent condition

$$IP > \sqrt{3^2 + (2\,\sigma_\theta \cdot \Delta x)^2} \;\; \mu\mathrm{m} \tag{3.5}$$

where $\sigma_\theta = \sqrt{(0.00305)^2 + (0.0194 \cdot \theta_{\mathrm{t}})^2}$ is the parametrization of the angular error, the first term in the square root in equation 3.5 taking into account the minimum sensitivity of the instrument. On average, the minimum impact parameter corresponds to about 10 $\mu$m. $\Delta x$ is the distance of the vertex from the most upstream emulsion surface (hereafter indicated as “vertex depth”).

finally, it must be taken into account that $\pi^0$'s are produced in neutrino interaction, which then convert in $\gamma$ pairs, which again convert in electron positron pairs. These tracks are both almost collinear with the photon direction because their transverse momentum is negligible, and, since the photons from pion decay point to the neutrino interaction vertex, the electron pair's tracks are both pointing to the interaction vertex. Thus, to reject events with electron pairs in which possibly only one of the two tracks is matched, a cut on the minimum kink angle is applied, i.e. $\theta_{\mathrm{kink}} > 10$ mrad. The kink angle is defined with respect to the line that links primary to decay vertex (see the sketch in figure 3.7.b).

For events passing the selections described so far, the average number of TT matched tracks is reduced to 2.4, as shown in figure 3.6.c on page 63.

One can have a feeling of what happened looking at figure 3.8, in which two images taken from the event display are shown. The left picture shows the event as it appears after the first level tracking, i.e. with about 4,000 tracks in fiducial volume. The right picture then shows the event after fine alignment, low momentum tracks rejection, and after the charm selection. A “vee” topology, i.e. a decay in two prongs of a neutral charmed hadron, has been isolated.

With the described algorithm, two stopping tracks with a distance smaller than 20 $\mu$m are supposed to build a common vertex. This means that the method is not suitable to

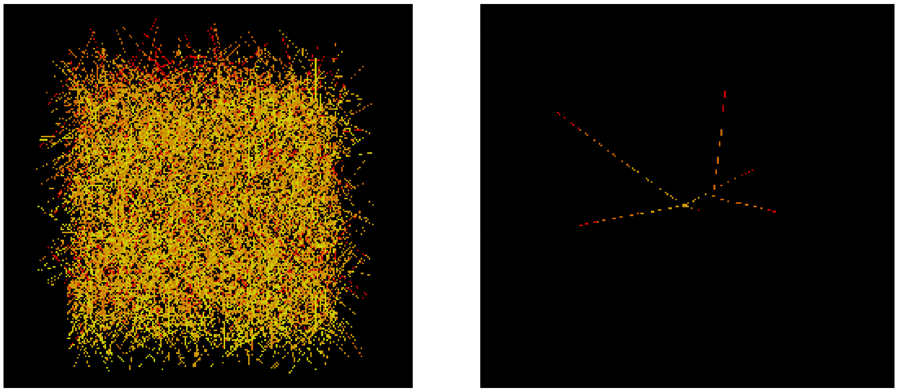

(a) (b)

FIGURE 3.8 – (a) The netscan fiducial volume containing all the track segments. (b) After low momentum and passing through tracks rejection, about 40 stopping tracks remain in the fiducial volume. Here, after the selection for charm search, a "vee" topology (i.e. a decay of a $D^0$ in two prongs) has been isolated. The decay vertex appears on the right; on the left is the interaction vertex.

detect decay paths shorter than 20 $\mu$m. However, applying more stringent conditions, a partial recovery of short decays, down to a few microns, is possible. The dedicated code is presently applied to events where the muon and the candidate decay track are both particularly well reconstructed.

### 3.3.2 Upgrades

The original netscan reconstruction code (ECFSAL + ECVTXA) was developed by the Nagoya group in parallel with the scanning technique. In the initial period of netscan, raw data, reconstruction code and reconstructed emulsion data were stored in a database which was physically located in Japan. When the necessity for a larger number of users to access the code and the data arose, it was decided to export the code to a central repository on CERN machines. At the same time, some structural optimizations, mainly aiming to improve the code portability, were implemented. As mentioned, the analyses are based on both the emulsion and the electronic data. Originally, these two sets of data were stored in two different databases (Objectivity-based for emulsion data, and Oracle-based for electronic data). The electronic reconstructed quantities contained in the original Oracle Nagoya database had been determined with the reconstruction program

(CHORAL) version used for the location of each particular event, which varied during the years. On the contrary, for the central version it was decided to always use the results of the latest CHORAL version – in order to allow upgrades and bug fixing – and to store all kinds of data in a single Objectivity database – to facilitate the cross talk between emulsion and counter data.

The old Nagoya code had already been used in charm searches (for example, the events used in our analysis have been selected with that version of the code, and then scanned manually). In the future analyses, the new version is going to be used. Then a comparison of the performances of the two codes was needed, e.g. to correctly calculate the efficiencies. To do this, the selection described in section 3.3.1 was implemented in the new framework, and run on the same set of netscan events as for the old one. It turned out that the overlap of the two sets of selected events amounted to 96%, the difference arising from the fact that the selection requested a matching with the target tracker, and upgrades in the target tracker reconstruction code sometimes translated in slight changes of the electronic track parameters.

Together with the reproduction of the old selection, also an improvement study was started in the new framework, mostly finalized to the selection of many-prong (rare) charm decays. The selection is mainly based on the track multiplicity count at reconstructed vertices, and on some additional criteria aiming to track validation, as the optimization of the TT matching criteria and on the tuning of other quality parameters such as the number of gaps allowed in a track. Preliminary results show an increase in the relative number of decays with a number of prongs equal to or greater than 4, but with a still significant loss in efficiency, thus the work must be considered in progress.

## 3.4 Manual check

The events that passed the selections described above are considered charm candidates. Nevertheless, there is the possibility that a selected event is background. The main sources of background are:

wrong track elements or vertices association by recontruction software: the candidate track does not exist or does not come from a decay vertex;

the charm candidate is in fact a photon conversion;

the secondary vertex is given by the interaction in the emulsions of one of the hadrons produced in the neutrino interaction.

At present, to distinguish fake from real decays, an eye check of the event is still needed.

Thus, events selected with the above procedure as charm candidates are manually checked to validate the hypotesis. The manual scanning also allows, if needed, to measure the parameters of tracks and vertices with the maximum resolution allowed by the emulsions. On the other hand, the eye check of a large number of events requires a huge amount of work from a human operator that performs the measurements. On average the scanning of one event takes about twenty minutes.

The first goal of the manual check is to verify that the selected candidate track actually exists and originates form a decay vertex. The manual check procedure starts from the predicted vertex plate, i.e. the plate that is supposed to contain the decay. From netscan the parameters of the candidate track (position and angle) are known, so that the track can be searched for in the predicted plate. Once it has been found, it is followed until it disappears. This can happen for two reasons: the first one is that it has reached its origin vertex, the second one is that the most upstream face of emulsion plate has been reached and the track was a passing through with respect to the current plate. In the latter case, the track is searched for in the further upstream plate, and so on until the vertex plate is reached. If the candidate track reveals to be passing through the vertex plate too, the event is discarded.

If the selected track disappears within the plate, there is still the possibility that the event is background. This is the case, first of all, if the predicted track in fact goes to the primary vertex: this can happen if, for example, the last track segment was not detected, so that the distance with respect to the primary vertex was artificially enhanced. This is the second source of background for importance. Passing through tracks that the selection was not able to eliminate and events in the tail of distance together amount to about 50% of the background.

A second possibility is that the selected track indeed goes to a secondary vertex, but this is an interaction vertex, or a $\gamma$ conversion point. The former represent about 25%, while the latter represent 13% of the background. Photon conversions are relatively easy to identify on the basis of the small opening angle of the two tracks. The rejection of secondary hadronic interactions demands a close inspection of the vertex, which, in the emulsionists jargon has to be *white*, i.e. no evidence for nuclear fragments, typical of hadronic scattering on nuclei, has to be seen.

Finally, the number of prongs at the decay vertex has to fulfill the obvious conditions for a decay vertex: odd number of outgoing tracks for charged decays, even for neutrals.

### 3.4.1 Netscan measured data

As mentioned in section 3.1, the data analyzed in this thesis correspond to a sample of 27,073 $1\mu$ located events. The netscan data for these events were analysed with the charm selection agorithm described in section 3.3.1, including the recovery for short decays. The charm candidates selected were 841. These events were manually checked, and 533 showed up to be charm events, thus giving a selection purity of 63%.

The results of the manual check of the confirmed charm events are stored in an electronic database, containing parameters of the parent track, number of decay prongs, parameters of the decay products, and positions of interaction and decay vertices. This sample is used for the analysis decribed in chapter 4.

## 3.5 Efficiencies

The evaluation of the netscan method efficiency is still in progress. A first estimate of the efficiency for every step of the full chain has been performed in the frame of a study of production of *neutral* charmed hadrons [72], which is now under way. Since the sources of inefficiencies are in common, we have adapted that estimate to the case of charged particle decays.

The global efficiency can be subdivided in several components: first, we have the scan back location efficiency, up to vertex location, which has nothing to do with netscan, and was already evaluated in the frame of the oscillation search. It is found to be 40%.

The netscan efficiency $\varepsilon_{\text{NETSCAN}}$ can be divided in two terms:

$\varepsilon_{\text{GEO}}$ ($\sim 90\%$) gives the geometric acceptance of the netscan fiducal volume, and slightly depends on the kind of charmed hadron produces, because of different lifetimes and different angles of the decay products;

$\varepsilon_{\text{REC}}$ ($\sim 90\%$) reflects the performance of the filtering and tracking algorithms described in section 3.2.2.

Then, in summary, $\varepsilon_{\text{NETSCAN}} = 85\%$.

Then the charm selection efficiency $\varepsilon_{\text{SEL}}$ must be considered, which measures the efficiency of the selection criteria applied to define the candidates, the most sensitive one being the request of TT matching, which can be measured directly from our data as descibed below. On average, $\varepsilon_{\text{SEL}} = 65\%$.

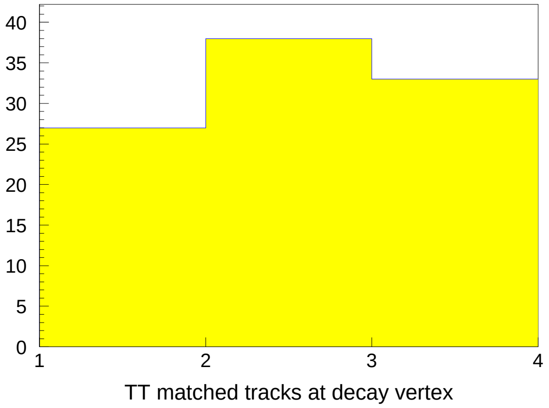

FIGURE 3.9 – Number of TT matched decay tracks for charm decys into three prongs.

The overall average efficiency for charm selection with netscan is $\varepsilon = \varepsilon_{\text{NETSCAN}} \cdot \varepsilon_{\text{SEL}} = 55\%$.

For what concerns the selection, it comes out that the condition that mostly determines the efficiency is the request of TT matching. The effect of this request can be measured using our sample of 108 events with a three prong decay. Figure 3.9 shows for these events the distrubution of the number of TT matched tracks. Since only tracks falling into the acceptance of the target tracker are included, the probability of 1, 2 or 3 matches is given by a binomial distribution of the form

$$P_\alpha(k) = \begin{pmatrix} 3 \\ k \end{pmatrix} \alpha^k (1-\alpha)^{3-k} \quad k = 0, ..., 3 \tag{3.6}$$

where $\alpha$ is the unknown macthing efficiency that we want to determine, and is the free parameter of the fit. At fixed $k$, the number $P_\alpha(k)$ represents in fact the probability that $k$ out of 3 tracks are matched if the matching efficiency is $\alpha$, where $k$ can range from 0 to 3.

Note that in our data the probability of 0 matched track is not measured, since with no matched track the charm event cannot be identified. The result of the fit is a matching efficiency $\alpha = 0.69 \pm 0.08$. Therefore, the requirement of at least 1 TT matched track, turns out in a loss of $1-\alpha = 31\%$ of the charm decays in 1 charged prong, while the loss for

3 and 5 prongs decay is very small ($\sim (1-\alpha)^3$ and $(1-\alpha)^5$). The complete evaluation of the efficiency will then include small corrections taking into account the finite acceptance of the TT as a function of the angular distibution of the particles from the decay.

## 3.6 Outlook

We have seen that the selection procedure described above which searches for charm events in a sample of events analyzed with the netscan technique has an efficiency of 55% and a purity of 63%. The fraction of background events contained in the sample is then quite large, so that a manual validation of the candidates is mandatory.

The optimization of the charm selection is going on. Many features of the analysis can be improved: in fact, work is now in progress for what concerns the alignment, the multiple scattering treatment, the track and vertex fitting, and the filtering of background tracks.

An improvement of the performances of the reconstruction and selection programs will be very useful, allowing to reduce the load of manual scan, which is at present the bottleneck of the analysis. The ultimate goal would be to reach a level of purity of the sample and a quality of the recontruction of the event topology such to avoid completely the manual scan.

Preliminary tests of new algorithms now under developement indicate that a purity larger than 85%, combined with an efficiency for charm selection of the order of 50%, is within reach.

# CHAPTER 4

# Measurement of charmed hadron fractions

The aim of the measurement here described is to determine the relative fractions of charged charmed hadrons (i.e. $D^+$, $D_s^+$, $\Lambda_c$) produced in charged current interactions of $\nu_\mu$ with the CHORUS emulsions target, as a part of a more general study of neutrino induced charm production. The final aim of the measurement will be an improvement on the determination of $V_{cd}$, $m_c$, strange content of the nucleon, which are fundamental numbers of the Standard Model.

The most relevant properties of charmed hadrons were summarized in table 1.2 on page 23. As already mentioned in section 1.4, the most recent direct measurement available up to now of the production rates comes from E531 and dates back to 1988. The E531 experiment, as CHORUS, used a target of nuclear emulsions. The target was followed by electronic detectors to measure momentum and charge of hadrons and muons. The sample amounted to 121 identified decays of charmed hadrons (including $D^0$'s).

As discussed in chapter 3, for the CHORUS second phase of analysis a new emulsion scanning method called netscan has been developed, which allows with a very high efficiency the identification of decays of charmed hadrons in emulsion (as well as that of other particles with a similar lifetime, e.g. the $\tau$ lepton). Since the selections used to isolate charm decays have a purity of about 60%, an event per event eye check on the selected ones is performed to eliminate backgrounds. The chain netscan–manual check guarantees the full topological identification of the decay of the charmed hadron, as well as a very precise measurements of all track angles and vertex positions. This means that decay length and all the relevant angles are known.

The electronic part of the detector is used to measure the kinematics of the event, even though the information that we have at our disposal is not complete. In fact, the limitations on acceptance, momentum resolution and efficiency of the hadron spectrometer (see section 2.8) make impossible, in most of the cases, to reconstruct the momentum of the decaying particle. The kinematic information used is then limited to muon momenta and hadronic energy.

The present analysis is limited by the currently available statistics: 167 decays of charged hadrons were analyzed. In the future CHORUS expects to have more than 10 times the current statistics, from the completion of the netscan of the presently located events, and also from the location of new events.

The measurement is based on a fit of some of the available kinematic distributions, where the free parameters are the relative fractions of $D^+$, $D_s^+$ and $\Lambda_c$, while the production mechanism is left fixed. In fact, what distinguishes $D^+$ from $D_s^+$ from $\Lambda_c$ is the lifetime $c\tau$, while we are able to measure the decay length $l_{\text{decay}} = \beta\gamma c\tau$, from which the momentum cannot be deconvoluted directly because it is not known event by event. However, also the decay angle $\theta_{\text{decay}}$ is known, and the product $l_{\text{decay}}\,\theta_{\text{decay}}$ is correlated to $c\tau$[1]. Then, simultaneously fitting $l_{\text{decay}}$ and $\theta_{\text{decay}}$ makes the measurement less sensitive to the smearing of lifetimes induced by the particle's momentum.

The distributions obtained from the experimental data set are compared with the corresponding ones coming form a Monte Carlo simulation of neutrino interactions in which a $c$ quark is produced, which subsequently fragments into a hadron and then decays. From Monte Carlo, the contributions of $D^+$, $D_s^+$ and $\Lambda_c$ can of course be considered separately.

The assumption that we make is that the shapes of the Monte Carlo distributions are correct: then the relative fraction of every charged charmed hadron in the data set can be measured, for example by means of the $\chi^2$ minimization. Of course this is a simplifying assumption, and we shall discuss in the following how to overcome.

---

[1] If $p_\perp$ is a decay product's transverse momentum, $\theta_{\text{decay}} \simeq p_\perp/p$, and if $n$ particles were produced in the decay of a parent of mass $M$ and momentum $P$, roughly $p_\perp/p \simeq (M/n)/(P/n) = M/P$. Thus, $\beta\gamma = (P/E)\cdot(E/M) = 1/\theta_{\text{decay}}$, hence $l_{\text{decay}}\,\theta_{\text{decay}} \simeq l_{\text{decay}}/\beta\gamma = c\tau$

The first part of this chapter describes the data set, while in section 4.2 the Monte Carlo contents and the cuts applied to simulate the reconstruction process are reported. Then a brief discussion is dedicated to the background sources, and the number of expected background events is estimated. The details of the fitting procedure are given in section 4.5.

## 4.1 The data set

The data sample used comes from the application of the selection procedures described in section 3.3 to 27,000 events analyzed with netscan, corresponding to 18% of the total number of $1\mu$ events located in the first phase of the oscillation analysis.

Out of the initial 27,000 events, 841 were selected as charm candidates and consequently sent to the manual check. 533 events resulted to be actual charm decays, translating in a selection purity of 63%. For what concerns the number of prongs (i.e. the number of charged decay products, the only visible in emulsions), 240 events contain a decay into an odd number of prongs, thus originated by a charged particle. They are subdivided as follows: 126 events are 1 prong, 108 are 3 prong and 6 are 5 prong decays.

The eye check is needed not only to confirm the decay, but also to improve the quality of the measurement of vertex and tracks parameters. Not all the confirmed charms have yet been completely measured.

Out of the 240 charged decays stored in the confirmed charm database, 167 events are measured at manual scanning and contain the complete electronic detector information. For these events, primary and secondary vertex positions are measured in emulsion, as well as charm and all charged daughters' slopes. The other relevant kinematic quantities (such as energy release in calorimeter and muon momenta measured by the spectrometer) are given by the electronic detector response.

Table 4.1 summarizes the data flow. Also reported is the subdivision of the events per number of prongs, both for the complete charm sample and for the final fully reconstructed sample.

## 4.2 Event simulation

The information extracted from the data sample just described has to be compared to the response of a Monte Carlo simulation in order to extract the fraction of different charmed

| **Netscanned events** | **27,073** |
|---|---|
| Events that passed the selection for charm search | 841 |
| Confirmed charm events | 533 |
| (neutrals) | (293) |
| **Confirmed charged charm events** | **240** |
| 1 prong | 126 |
| 3 prong | 108 |
| 5 prong | 6 |
| **Fully measured charged charm events** | **167** |
| 1 prong | 85 |
| 3 prong | 78 |
| 5 prong | 4 |

Table 4.1 – The charm data flow.

hadrons from the data.

The data could in principle contain also background, so that measurements should be compared to the simulation of charm production plus the simulation of the background. The expected background is discussed in section 4.4, where we shall see that there are few expected events in the sample.Though simulated, the background is not included in the analysis.

### 4.2.1 Monte Carlo contents

Our Monte Carlo describes charm production via deep inelastic scattering on a target with the proton/neutron relative fraction corresponding to the emulsion one, following the model described in section 1.2.1 for non isoscalar targets (for the CHORUS nuclear emulsions, $\left\langle A^{\frac{1}{3}} \right\rangle \simeq 2.4$).

Although, as discussed in section 1.3, charm production also happens in quasielastic and diffractive processes on top of deep inelastic scattering, quasielastic and diffractive production are not included in our simulation yet. The inclusion is in progress, but since these processes are relatively rare, we do not expect them to seriously affect our analysis.

In fact, a 4 GeV cut on the minimum hadronic energy of the events, present in our data, suppresses the quasielastic production of $\Lambda_c$, which is characterized by low momentum since the baryon produced has momentum “similar” to that of the nucleon, which is at rest in the laboratory frame. A study of very short decays is currently under way in CHORUS, which provided so far a sample of 70 events from which those having the quasielastic topology could be isolated. Rescaling to our sample, and taking into account the 4 GeV cut, a contribution of about 3 events is expected from quasielastic production.

For what concerns diffractive production, in a dedicated search for dimuons performed on a sample corresponding to 300,000 charged current events, CHORUS has observed the diffractive production of 1 $D_s^{*+}$ through the observation in emulsion of the decay chain $D_s^+ \to \tau^+ \bar{\nu}_\tau$, $\tau^+ \to \mu^+ \bar{\nu}_\mu$ (the path of the $D_s^{*+}$ is of course not detectable) [53]. Rescaling this number to our sample, taking into account all the efficiencies, we expect a contribution of 6 events.

Our simulation of deep inelastic $\nu_\mu$ charged current interactions comes from JETTA [73], the standard CHORUS event generator. It is based on the LEPTO [74] package to simulate $\nu_\mu$ charged current interactions, and JETSET [75, 76] for quark hadronization and decays of short lived particles, with some peculiar modifications for CHORUS, and can describe neutrino interactions with $q^2 > 2$ GeV$^2/c^2$.

In JETTA, the nucleon structure functions are parametrized according to GRV94LO [36, 37], and the nuclei have a Fermi motion parametrized by $dn/dE_{\text{kin}} \propto \sqrt{E_{\text{kin}}}$, with a maximum kinetic energy of 27 MeV.

For what concerns heavy quark production, the slow rescaling is not implemented, however to take into account the charm mass threshold effect, the CC cross section for the production of a light quark is multiplied by the factor $(M + m_c + m_{\text{rem}} + m_d)^2/W^2$, where $M$ is the nucleon mass, $m_c$ and $m_d$ are the charm and down masses, and $m_{\text{rem}}$ is the target remnant.

The charm quark hadronization is parametrized according to the Peterson fragmentation function [43], and the charmed hadrons produced are $D^0$, $D^+$, $D_s^+$, $\Lambda_c$, the same fragmentation being used for all of them. The transverse momentum distribution was parametrized as $dn/dp_\perp \propto \mathrm{e}^{-\beta p_\perp^2}$. The starting values of the relative fractions of charmed hadrons produced in the $c$ quark hadronization are taken from a reanalysis of the E531 data [47].

Neutrinos reaching CHORUS from the CERN WBB are simulated by GBEAM [77, 78]. The response of the electronic detector is given by a GEANT3 [79] based simulation of the CHORUS detector (EFICASS), whose output is sent to the same reconstruction program as real data[2].

### 4.2.2 Simulation of the reconstruction chain

The Monte Carlo sample initially consists of 10,000 $\nu_\mu$ charged current interactions with vertex in bulk emulsion, in which a charmed hadron is produced at the primary vertex.

The event reconstruction chain consists of several steps. As reminded in section 3.2, netscan is applied to the events that had been located in phase 1, so a first set of cuts is applied to reproduce the scan back selection. When cuts refer to quantities that are measured in emulsion, the Monte Carlo truth is used[3], while in the other cases – i.e. when

---

[2] In this analysis, the CHORAL-02-20-06 version of the reconstruction program was used.

[3] A simulation of the tracks in emulsion and of the netscan procedure is under way, and could not be used for this analysis. However, the very high resolution on angle and position that is achieved in manual measurements allows to safely use Monte Carlo true quantities instead of the reconstructed ones.

the measurement comes from the electronic detectors – reconstructed quantities are used. The cuts referring to the selection for scan back (explained in detail in section 3.2) are:

primary vertex is reconstructed in emulsion;

a muon with negative charge must be reconstructed in the spectrometer, and the measured momentum must satisfy $P_\mu < 30$ GeV;

$\theta_\mu < 400$ mrad, where $\theta_\mu$ is the angle between muon direction and beam axis;

total energy released in the calorimeter $E_{\mathrm{HAD}}$ must be greater than 4 GeV.

Other cuts are applied to simulate the netscan procedure's geometrical acceptances:

secondary vertex must lie in the netscan fiducial volume, as described in section 3.2;

at least one daughter track must satisfy $-400 < \theta_{y,z} < 400$ mrad, where $\theta_y$ and $\theta_y$ are the angles between track and beam direction (conventinally taken as $x$) in the $\langle xy \rangle$ and $\langle xz \rangle$ planes;

Other ones must be applied in order to reproduce the selection criteria (for a detailed explanation of each of the following cuts, see section 3.3):

impact parameter of the daughter track with respect to the primary vertex must satisfy $IP > \sqrt{3^2 + (2\sigma_\theta \Delta x)^2}\,\mu$m, where $\sigma_\theta = \sqrt{0.00305^2 + (0.0194 \cdot \theta)^2}$ rad, and $\Delta x$ is the vertex depth;

at least two tracks matched with a target tracker reconstructed track must be present, going to two distinct vertices, the condition for TT matching being $\Delta\theta_{\mathrm{TT}} < 3.44\sqrt{(0.00546)^2 + (0.0194 \cdot \theta_{\mathrm{t}})^2}$ rad;

kink angle must be bigger than 10 mrad.

After all cuts are applied, the original 10,000 reduce to 4,801 events, 3,110 of them being $D^0$'s. The remaining 1,692 events are subdivided in 952 $D^+$, 354 $D_s^+$ and 385 $\Lambda_c$. Table 4.2 shows in detail how many events survive each step.

The available statistics is still limited, and a new huge production is in preparation for the phase 2. However, our Monte Carlo sample is in a ratio 10:1 with respect to the data sample size, thus the statistical error on Monte Carlo is still three times smaller than that on data.

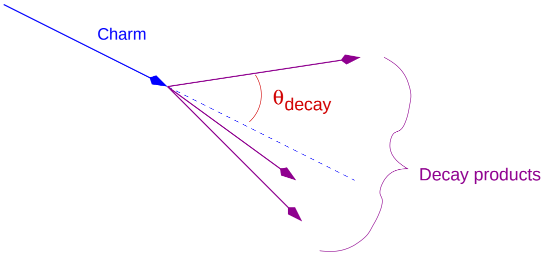

Figure 4.1 – Definition of the angle $\theta_{\text{decay}}$ in the case of multiprong decays.

## 4.3 First comparison Monte Carlo – Data

As a starting point, a comparison between data and Monte Carlo with the original charmed hadron fractions has been performed. For what concerns the topological branching ratios (i.e. what fractions of decays are in 1, 3, 5 prongs), data show a discrepancy with respect to the simulation. Table 4.3 reports the fractions of data and Monte Carlo events going in 1, 3, 5 prongs: the simulation shows a defect of 1 prong decays, and a corresponding excess of 3 prong decays with respect to the charm data set.

The discrepancy is enhanced by the fact that we expect lower efficiency for 1 prong than for 3 prong charm decays. At present, this discrepancy is a $3\sigma$ effect. However, given the fact that from existing measurements the topological branching ratios of $D^+$, $D_s^+$, $\Lambda_c$ are known with quite large uncertainties, we shall not use the number of prongs of the decay to distinguish among the charmed hadrons. Because of this, and also because of our limited statistics, 1, 3, and 5 prongs are put together and analyzed all at once.

The decay is first of all charcaterized by its length $l_{\text{decay}}$, which is measured in emulsion as the distance between interaction and decay vertex. This is expected to be a good separating quantity, because $D^+$, $D_s^+$ and $\Lambda_c$ have quite different proper lifetimes.

Then a decay angle $\theta_{\text{decay}}$ is considered, which corresponds to the kink angle for 1 prong decays, and is defined as the maximum angle between the charmed hadron and a decay product for multiprong decays (see figure 4.1).

The angle $\theta_{\text{decay}}$ is related to $l_{\text{decay}}$ by the (approximate) relation $l_{\text{decay}}\theta_{\text{decay}} \sim c\tau \sim$ 317 $\mu$m ($D^+$), 140 $\mu$m ($D_s^+$), 61 $\mu$m ($\Lambda_c$).

The distributions of decay length and $\theta_{\text{decay}}$ after the selections are shown in figure 4.2. The gross features of the distributions are reproduced (and the optimzation of simulation-

| **Initial MC sample** | **10,000** |
|---|---|
| Events surviving scan back cuts | 6,221 |
| Events surviving netscan cuts | 5,139 |
| Events surviving selection cuts | 4,801 |
| $(D^0)$ | (3,110) |
| **Final MC sample** | **1,691** |
| $D^+$ | 952 (56.3%) |
| $D_s^+$ | 354 (20.9%) |
| $\Lambda_c$ | 385 (22.8%) |

Table 4.2 – The Monte Carlo data flow.

| | 1 Prong | 3 Prong | 5 Prong |
|---|---|---|---|
| Data | 85 (50.9%) | 78 (46.7%) | 4 (2.4%) |
| MC | 671 (39.8%) | 932 (55.3%) | 82 (4.9%) |

Table 4.3 – Topological branching ratios (only odd prongs) for data and simulation.

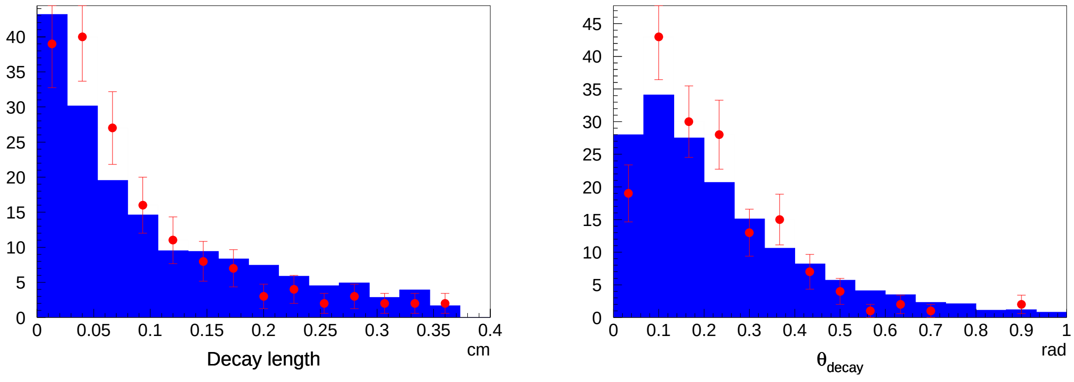

(a) (b)

FIGURE 4.2 – (a) decay length and (b) $\theta_{\text{decay}}$ comparison between Monte Carlo and data (represented in the plots by the histogram and the red dots respectively) after the kinematic selections.

data agreement is the goal of the present analysis, as will be described).

The small $l_{\text{decay}}$ region, an even more significantly the small $\theta_{\text{decay}}$ one, show an excess of Monte Carlo events. This feature is explained by a non flat behaviour of the netscan efficiency, with a loss in the kinematic regions close to the limit sensitivity of the method. i.e. for very short and/or small angle decays: in fact, when the impact parameter $l_{\text{decay}} \cdot \theta_{\text{decay}}$ is too small, it is difficult to detect the decay. As described in section 3.3.1, the charm selection from which our sample comes contains an angle dependent cut on the impact parameter, which on average corresponds to 10 $\mu$m, the minimum detectable distance being about 3 $\mu$m. It was then decided to apply more stringent cuts on these two variables, both on Monte Carlo and data, in order to cover all the angular range of the tracks in the small impact parameter region. Requiring

$l_{\text{decay}} > 20\ \mu$m;

$\theta_{\text{decay}} > 30$ mrad.

we are confident that the efficiency becomes independent of $l_{\text{decay}}$ and $\theta_{\text{decay}}$. Table 4.4 shows the number of Monte Carlo and data events surviving the fiducial cuts, while table 4.5 gives the topological branching fractions after the fiducial cuts: no great changes in the fraction behaviour happened.

| | |
|---|---|
| Monte Carlo events surviving fiducial cuts | 1,279 |
| $D^+$ | 812 (63.5%) |
| $D_s^+$ | 275 (21.5%) |
| $\Lambda_c$ | 192 (15.0%) |
| Data events surviving fiducial cuts | 137 |

Table 4.4 – Monte Carlo and data samples after fiducial cuts.

| | 1 Prong | 3 Prong | 5 Prong |
|---|---|---|---|
| Data | 68 (49.6%) | 66 (48.2%) | 3 (2.2%) |
| MC | 487 (38.1%) | 733 (57.3%) | 59 (4.6%) |

Table 4.5 – Topological branching ratios for data and Monte Carlo after fiucial cuts are applied.

Figures 4.3 and 4.4 then show decay length and angle distributions after these cuts are applied, for both Monte Carlo and data (top left plots). Also shown are the distributions separated for $D^+$, $D_s^+$ and $\Lambda_c$ to highlight the differences. Note that all the Monte Carlo distributions shown are normalized to the number of data events, to allow a direct comparisons of the shapes.

The starting Monte Carlo contains $D^+$, $D_s^+$ and $\Lambda_c$ in fractions taken from [47]. The agreement with data is already satisfactory, while distributions for $D^+$, $D_s^+$ and $\Lambda_c$ separately are different from those of data. This indicates that we are sensitive to the relative fractions.

Other kinematic variables have been considered, such as the hadronic energy of the event, i.e. the reconstructed energy release in the calorimeter $E_{\text{HAD}}$. This quantity is directly tied to the specific production mechanism, in fact baryons produced in quasielastic scattering show on average smaller hadronic energy (see section 1.3.1). The $E_{\text{HAD}}$ distributions (again after the fiducial cuts have been imposed on $l_{\text{decay}}$ and $\theta_{\text{decay}}$) are shown in figure 4.5.

Also the angle $\Phi$ between charm and primary muon in the plane transverse to the beam axis (as illustrated in figure 4.7) was taken into account. It is expected to peak at 180°, because a deep inelastic scattering can be considered a "two body" interaction, in the sense that it happens on a parton. Then, in the centre of mass frame, charm and muon recoil against each other, and in the laboratory frame transverse momenta are centre of mass momenta. The trend remains, despite the hadronization process. Since the above considerations hold for the three of our charged particles, we do not expect high hadron separation from this variable, but, as evident from figure 4.6, it provides a furhter confirmation of the good agreement between Monte Carlo and data, and moreover the separation capability between charged charm hadron decays and *background* is expected to be solid (see the following section).

Among others, we also considered the visible energy, defined as the sum of hadronic energy and muon energies as measured by the spectrometer, and the absolute angle $\alpha_{\text{charm}-\mu}$ between charm and primary muon.

The differences of data and simulated distributions separately for $D^+$, $D_s^+$, $\Lambda_c$ have been tested for all the variables considered so far, and the most sensitive ones have been chosen. In fact, some variables are correlated (e.g. hadronic and visible energy) and, moreover, as is going to be illustrated in the following, due to the limited statistics it was not possible to include all the kinematic variables here mentioned in the analysis: only three of them have been chosen for the fit. The remainig ones were in any case useful to

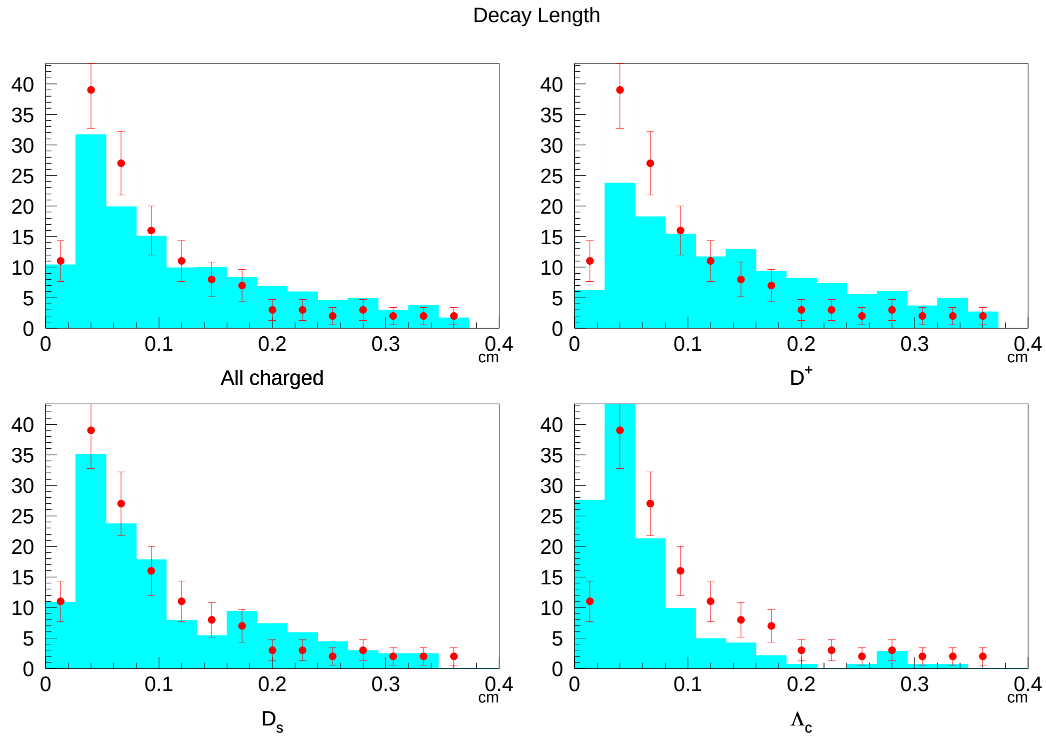

Figure 4.3 – Decay length distribution for Monte Carlo (histogram) and data (red dots). The entries of all Monte Carlo histograms are normalized to the number of data events. The top left plot contains the three Monte Carlo distributions of $D^+$, $D_s^+$ and $\Lambda_c$ superimposed.

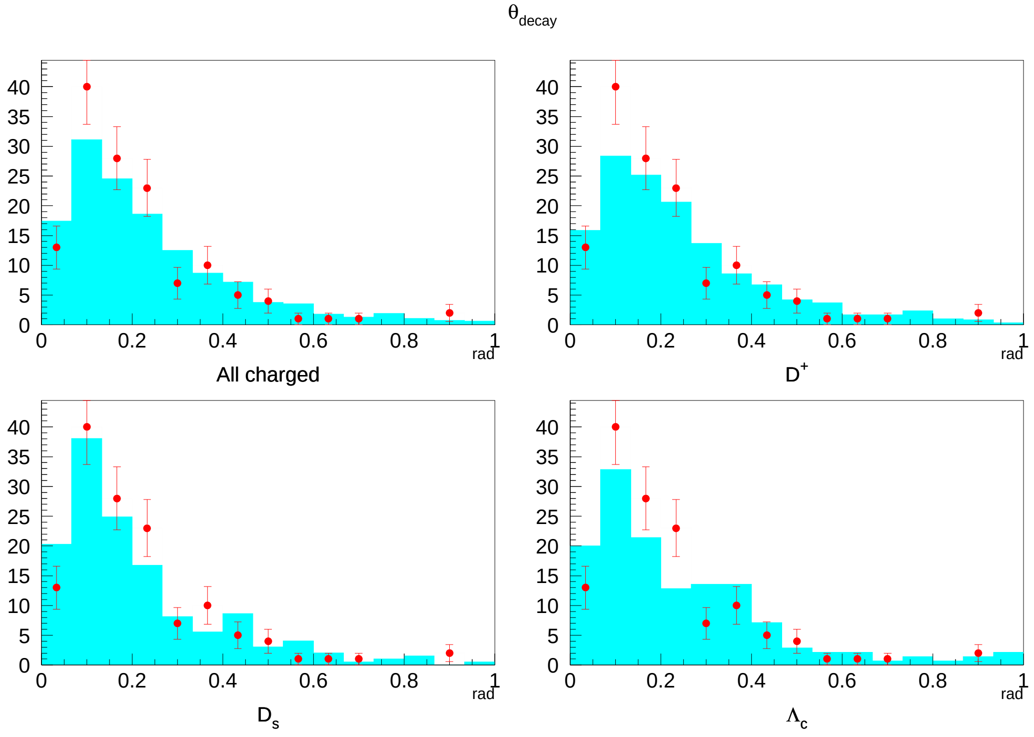

Figure 4.4 – $\theta_{\mathrm{decay}}$ distribution for Monte Carlo (histogram) and data (red dots). The entries of all Monte Carlo histograms are normalized to the number of data events. The top left plot contains the three Monte Carlo distributions of $D^+$, $D_s^+$ and $\Lambda_c$ superimposed. For the definition of $\theta_{\mathrm{decay}}$, see the text.

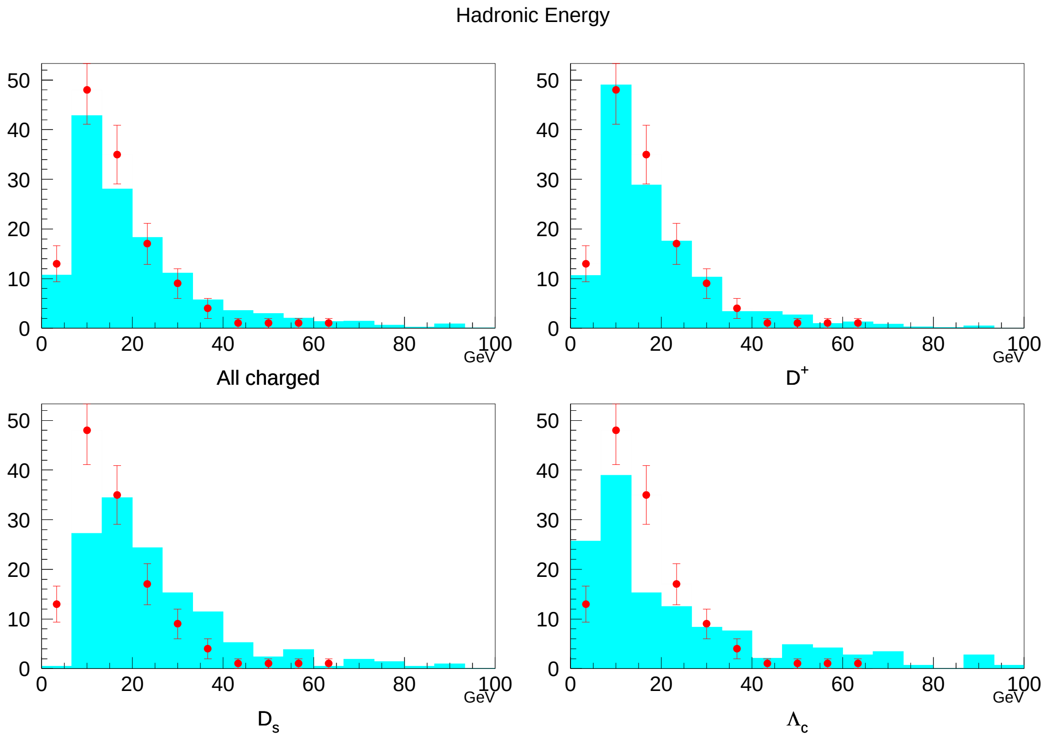

Figure 4.5 – Hadronic energy distribution for Monte Carlo (histogram) and data (red dots). The entries of all Monte Carlo histograms are normalized to the number of data events. The top left plot contains the three Monte Carlo distributions of $D^+$, $D_s^+$ and $\Lambda_c$ superimposed.

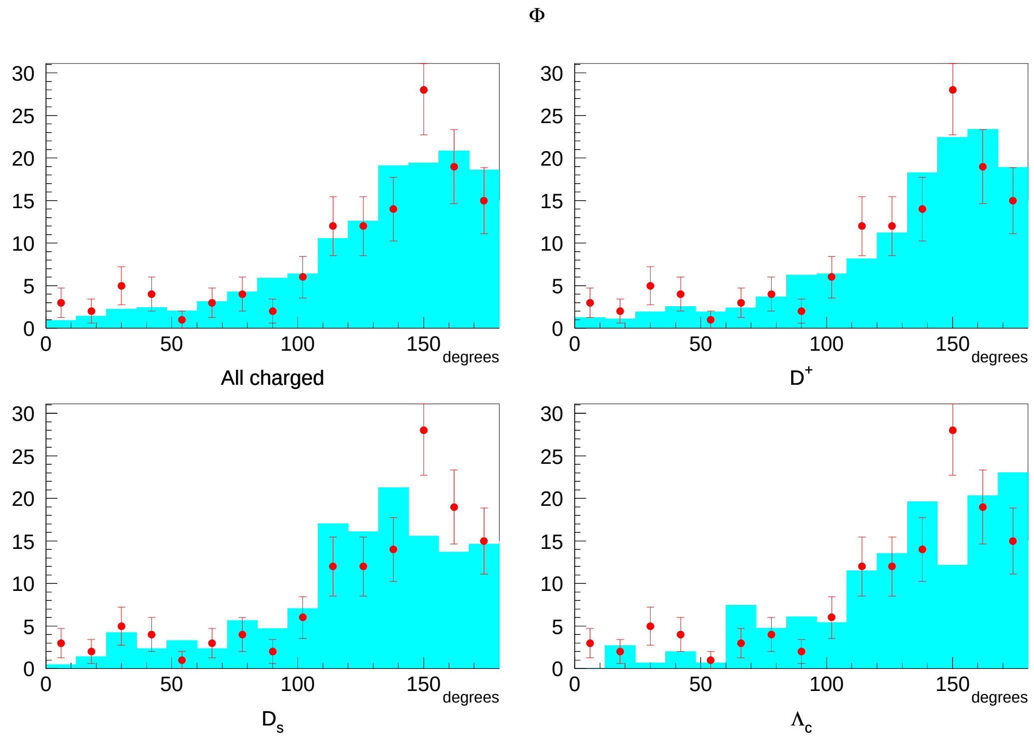

Figure 4.6 – Angle Φ distribution for Monte Carlo (histogram) and data (red dots). The entries of all Monte Carlo histograms are normalized to the number of data events. The top left plot contains the three Monte Carlo distributions of $D^+$, $D_s^+$ and $\Lambda_c$ superimposed. For the definition of Φ, see the text.

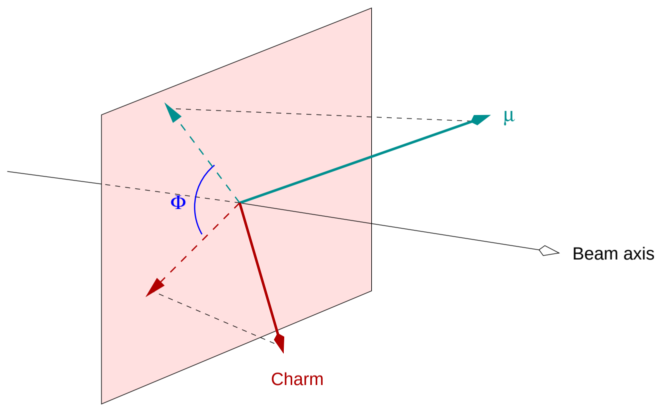

FIGURE 4.7 – Definition of the angle Φ.

confirm the good agreement of data and simulation, and were also used for further cross checks.

## 4.4 Background estimation

In principle, also background can be present in the data. The background estimation was performed for the oscillation search (see for example [80]), and because of the similar topology of $\tau$ and charm decays, the main sources are shared.

The charm into 1 prong decays are faked by 1 prong interactions, mainly elastic scattering of pions and kaons, with invisible nuclear recoil. In the emulsionists' jargon, a white kink is a 1 prong nuclear interaction of a hadron, without any heavily ionizing track or other evidence of nuclear breakup. The small angle cut is expected to reduce this background because large kink angle corresponds to high $Q^2$, making invisible recoil unlikely.

As well, 3 prong decays are faked by 3 prong pion scattering with invisible recoil, which mainly happens via the diffractive production of $a_1(1260)$, a hadronic resonance decaying in $\rho\pi$.

Contributions from non charmed hadrons' decays (pions, kaons, $\Sigma$'s) are expected to be less important.

### 4.4.1 White kinks

We want to give here an estimate of the number of white kink events expected in the charm sample analyzed, and also to produce distributions of the kinematic variables which were plotted in the previous section for charm events, to be eventually included in the fit to have a cross check of the expected number of white kinks.

A Monte Carlo simulation has been performed of about 14,000 $\nu_\mu$ charged current events in which a charged pion (randomly chosen among the on average 3.6 pions of the event) undergoes a white kink. Then the kinematic cuts are applied, which were described for the charm analysis, treating the pion before it scatters as the charmed hadron, and the scattered pion as the charm decay product.

The interaction length $\lambda_{\text{WK}}$ for a pion produced in $\nu_\mu$ neutral current had been measured in CHORUS [80], because such an event constitutes a background to $\tau$ decays without muon also in the oscillation search. The value $\lambda_{\text{WK}} = 7.6$ m of [80] is then assumed, which is much greater than the 4 mm scanned, so that white kinks are simulated with a flat distribution in the netscan fiducial volume.

In CHORUS, also detailed studies of the pion transverse momentum distribution in white kink have been carried out: the one used [81] is shown in figure 4.8, while the momentum modulus of the outgoing pion is assumed to be equal to that of the ingoing one, since we are dealing with an elastic scattering.

The number of expected events in our sample of charm events is given by

$$N_{\text{WK}} = \frac{N_{\text{sel}}}{N_{\text{CC}}} \frac{l_{\text{fid}}}{\lambda_{\text{WK}}} N_{\text{loc}} \, \varepsilon \, \langle n_\pi \rangle \tag{4.1}$$

where

$N_{\text{CC}}$ is the total number of simulated charged current events with a white kink after the scan back cuts on muon angle and momentum have been applied (6,308);

$N_{\text{sel}}$ is the number of simulated events that survive the kinematic and fiducial cuts described in section 4.2.2 (1,279);

$l_{\text{fid}}$ is a fiducial length used in the simulation: white kinks were simulated with a flat distribution between 0 and $l_{\text{fid}}$. The value $l_{\text{fid}} =$ 6 mm was used;

$\lambda_{\text{WK}} = 7.6$ m is the already mentioned white kink interaction length;

$N_{\text{loc}}$ is the number of located events that originated, after netscan reconstruction and selection, the present charm sample (27,073);

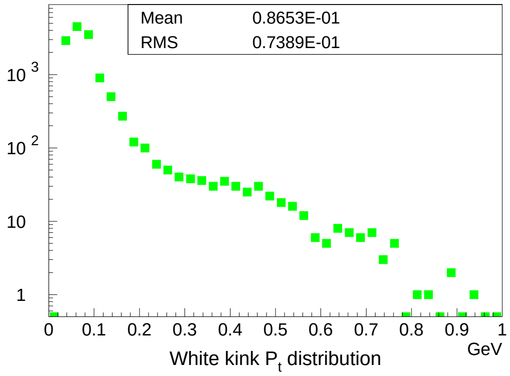

Figure 4.8 – The transverse momentum distribution used in the white kink simulation.

$\varepsilon = 45\%$ is the efficiency of charm selection with netscan on 1 prong events;

$\langle n_\pi \rangle$ is the average number of charged pions per event (3.6).

The calculation gives $N_{\rm WK} = 7$ events. This number must of course be referred to the total sample of charged charm, i.e. to 240 events. Since we just used 167 events, in our sample we then expect $7 \cdot 167/240 = 4.9$ events.

Figure 4.9 shows the distributions for white kink events after all cuts are applied. To allow a comparison, the corresponding distributions for charm data were superimposed. Because of the big $\lambda_{\rm WK}$, the decay length distribution is almost flat (the fall at large $\lambda_{\rm WK}$ is due to the fact that some long decays happen outside the volume because of the pion angle). $\theta_{\rm kink}$ is instead peaked at very small values, because of the small $Q^2$ in the scattering.

Few checks on the distributions, and the evaluation of the error on the 4.9 expected events are still going on.

### 4.4.2 The $a_1(1260)$ resonance

This source of background was already estimated in CHORUS [82] in the frame of the $\tau \to 3$ prong analysis. Using the cross sections that can be found in the literature an interaction length of 50 m was extrapolated. Then the number of expected events in our

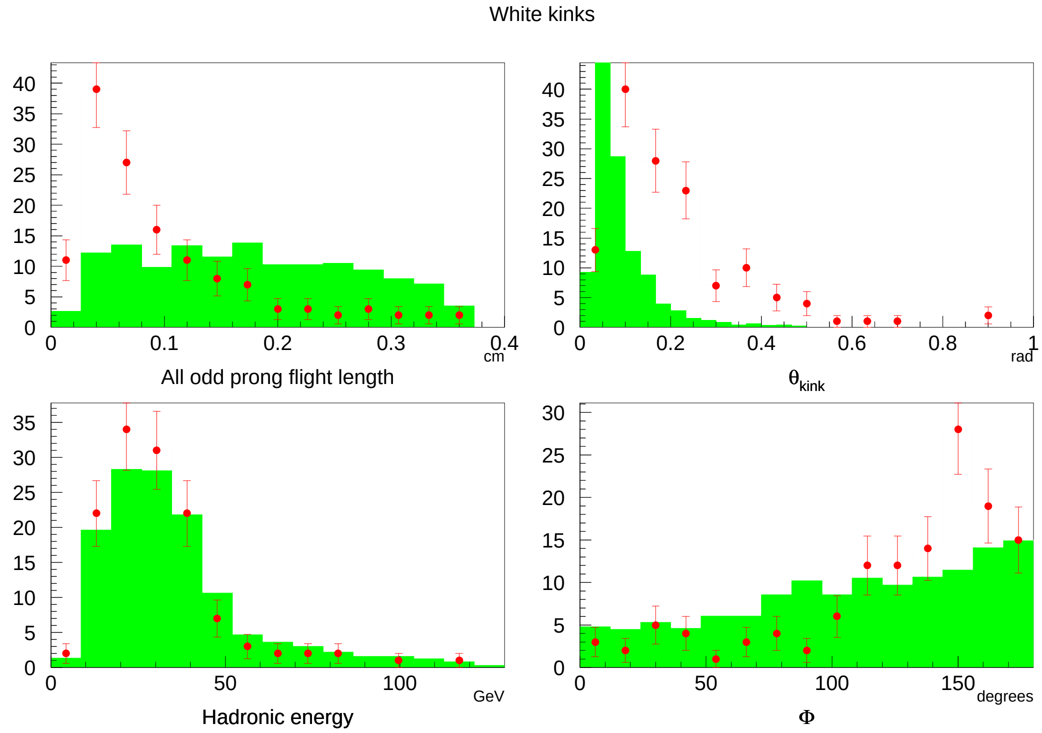

FIGURE 4.9 – Distributions of decay length, $\theta_{\mathrm{kink}}$, hadronic energy and angle $\Phi$ for a pion, produced in a $\nu_\mu$ charged current interaction, which undergoes a white kink (histogram). Superimposed are the corresponding distributions for charm data events (red dots).

sample can be estimated as

$$N_{a_1(1260)} = \frac{l_{\text{scan}}}{\lambda_{\text{int}}} N_{\text{loc}}\, \varepsilon_{\text{loc}} \tag{4.2}$$

where

$l_{\text{scan}}$ is the track length scanned per event, corresponding to 4 mm (see section 3.2.1), times the average number of charged pions (regardless the sign), i.e. 3.6;

$\lambda_{\text{int}}$ is the estimated interaction length (50 m);

$N_{\text{loc}}$ is defined as in equation 4.1 (27,073);

$\varepsilon_{\text{loc}}$ is the scan back location efficiency, 50%.

The calculation gives 2.9, that scaled to our sample gives expected 2 background events from $a_1(1260)$ interactions, which were neglected.

## 4.5 Fitting procedure

Our analysis, because of the small statistics, will fit only the relative precentages of charmed hadrons in the sample. What we assume is that the production mechanisms of $D^+$, $D_s^+$ and $\Lambda_c$, as well as the detector response, are reproduced well enough by the Monte Carlo. The fit then will determine the combination of simulated $D^+$, $D_s^+$ and $\Lambda_c$ distributions that best reproduces the measured one.

### 4.5.1 Choice of variables and binning

We have shown several variables that provide a good separation of the three species, but unfortunately the number of events is limited, both for the real data sample and for the simulated one.

What we are going to do is to select some of the kinematic variables shown, which will determine our phase space, and perform a $\chi^2$ fit of the Monte Carlo distributions to that of data. We also tried the option of a likelihhod minimization (which gave results compatible with that of the $\chi^2$), but the first option was adopted because it is easier to keep under control the behaviour of the fit.

In order to have a statistical error on the content $n$ of a cell (whose dimensions are determined by the binning chosen for the single distributions) that can be approximated with $\sqrt{n}$, about a dozen of events should be contained in each cell.

The bigger is the phase space (i.e. the number of variables considered), the smaller will be the number of events that fall in a single cell once its dimensions (i.e. the binning of the single variable's distribution) are fixed. On the one hand, one could try to enlarge the cell size, but this would imply that the differences in the three charmed hadron distributions are depleted. On the other hand, one can reduce the number of variables considered. Then a compromise must be found that mantains a suitable cell size and a significative set of variables.

Of course, the higher the number of variables that can be used, the more precise will be the analysis of the sample. The best result is obtained considering "combined" distributions, i.e. building the probability that a hadron decays with a particular decay length *and* with a particular hadronic energy, and so on.

According to the discussion in section 4.3, we choose $l_{\text{decay}}$, $\theta_{\text{decay}}$ and $E_{\text{HAD}}$: decay length and $\theta_{\text{decay}}$ are intrinsic characteristics of the particle type, and hadronic energy offers a good separation of $D^+$, $D_s^+$ and $\Lambda_c$ distributions, while the agreement of Monte Carlo and data is at the same time remarkable. For example, dividing the three of them in 2 bins, we have $2^3 = 8$ cells, in which our 137 events can be suitably arranged. For example, the binning

$$\begin{array}{lll} \Delta^{(1)} l_{\text{decay}} = \{0.02, 0.06\} & \Delta^{(2)} l_{\text{decay}} = \{0.06, \infty\} & (\text{cm}) \\ \Delta^{(1)} \theta_{\text{decay}} = \{0, 0.14\} & \Delta^{(2)} \theta_{\text{decay}} = \{0.14, \infty\} & (\text{rad}) \\ \Delta^{(1)} E_{\text{HAD}} = \{0, 15\} & \Delta^{(2)} E_{\text{HAD}} = \{15, \infty\} & (\text{GeV}) \end{array}$$

satisfies this necessity.

Another possible choice is to limit the fit to only two variables: as discussed before, the product $l_{\text{decay}}\,\theta_{\text{decay}}$ is correlated to the mean life $c\tau$ which is an intrinsic characteristic of each particle. Thus, if the analysis must be done on two variables only, the most convenient choice is that of $l_{\text{decay}}$ and $\theta_{\text{decay}}$. In this second case, a binning which satisfies the request of having at least ten events in each cell can be of the type

$$\begin{array}{llll} \Delta^{(1)} l_{\text{decay}} = \{0.02, 0.05\} & \Delta^{(1)} l_{\text{decay}} = \{0.05, 0.10\} & \Delta^{(3)} l_{\text{decay}} = \{0.10, \infty\} & (\text{cm}) \\ \Delta^{(1)} \theta_{\text{decay}} = \{0, 0.10\} & \Delta^{(1)} \theta_{\text{decay}} = \{0.10, 0.17\} & \Delta^{(3)} \theta_{\text{decay}} = \{0.17, \infty\} & (\text{rad}) \end{array}$$

i.e. a division of each distribution in 3 cells, for a total of $3^2 = 9$ cells.

### 4.5.2 Construction of the probability distribution

Once che division in cells has been fixed, the experimental content of each cell is compared with the Monte Carlo generated content. Focusing e.g. on the choice of three variables divided in 2 bins, the number of simulated events that fall into each cell for each particle type, $N^{ijk}(D^+, \Delta^{(i)} l_{\rm decay}, \Delta^{(j)}\theta_{\rm decay}, \Delta^{(k)} E_{\rm HAD})$, $N^{ijk}(D_s^+, \Delta^{(i)} l_{\rm decay}, \Delta^{(j)}\theta_{\rm decay}, \Delta^{(k)} E_{\rm HAD})$, $N^{ijk}(\Lambda_c, \Delta^{(i)} l_{\rm decay}, \Delta^{(j)}\theta_{\rm decay}, \Delta^{(k)} E_{\rm HAD})$, $i = 1, 2, 3,\ j = 1, 2,\ k = 1, 2$ is evaluated.

Then the three normalized "probabilities" for an event falling in the cell $\{i, j, k\}$ to be $D^+$, $D_s^+$ or $\Lambda_c$ can be defined as

$$P_{D^+}(i,j,k) \equiv n^{ijk}_{D^+} = N^{ijk}(D^+, \Delta^{(i)} l_{\rm decay}, \Delta^{(j)}\theta_{\rm decay}, \Delta^{(k)} E_{\rm HAD})\,/\,N_{D^+} \tag{4.3}$$

$$P_{D_s^+}(i,j,k) \equiv n^{ijk}_{D_s^+} = N^{ijk}(D_s^+, \Delta^{(i)} l_{\rm decay}, \Delta^{(j)}\theta_{\rm decay}, \Delta^{(k)} E_{\rm HAD})\,/\,N_{D_s^+} \tag{4.4}$$

$$P_{\Lambda_c}(i,j,k) \equiv n^{ijk}_{\Lambda_c} = N^{ijk}(\Lambda_c, \Delta^{(i)} l_{\rm decay}, \Delta^{(j)}\theta_{\rm decay}, \Delta^{(k)} E_{\rm HAD})\,/\,N_{\Lambda_c} \tag{4.5}$$

where $N_{D^+}$, $N_{D_s^+}$, $N_{\Lambda_c}$ are the total number of $D^+$, $D_s^+$, $\Lambda_c$ in the Monte Carlo sample.

The same binning is applied also to the white kink background distributions which, normalized to the expected number of events, are subtracted from the data.

### 4.5.3 The $\chi^2$ minimization

For simplicity, we keep on considering the [three variables – 2 × 2 × 2] cells choice. The function to minimize is defined as (using just one index $i$ running over all of the 8 cells):

$$\chi^2(\alpha,\beta) = \sum_{i=1}^{N_{\rm bin}} \frac{\left[n^i_{\rm MC}(\alpha,\beta) - n^i_{\rm DATA}\right]^2}{\sigma_i^2(\alpha,\beta)} \tag{4.6}$$

where

$N_{\rm bin}$ is the number of bins used;

$n^i_{\rm DATA}$ is the content of the i-th cell of the distribution of charm data after background subtraction;

$N_{\rm DATA}$ is the total number of data events, $N_{\rm DATA} = \sum_i n^i_{\rm DATA}$. Correspondingly, the total number of Monte Carlo events is indicated as $N_{\rm MC}$;

$n^i_{\rm MC}(\alpha,\beta) = N_{\rm DATA}\left(\alpha\, n^i_{D^+} + \beta\, n^i_{D_s^+} + (1-\alpha-\beta)\, n^i_{\Lambda_c}\right)$ is the theoretical content of the i-th cell, normalized to $N_{\rm DATA}$, for each value of the parameters $\alpha$, $\beta$. Its square root also represents the error on the i-th cell's content;

$n^i_{D^+}$ is the content of the i-th cell of the $D^+$ Monte Carlo distribution normalized to the total number of $D^+$'s in the Monte Carlo sample, and analogous definitions for $n^i_{D_s^+}$ and $n^i_{\Lambda_c}$ as from equations 4.3—4.5;

$\sigma_i^2(\alpha,\beta)$ is the variance of the i-th cell, and is given by the sum of two contributions, $\sigma_{n_i}^2 + \Delta n_i$, where the first is the fluctuation of the expected content of the cell (which fluctuated to give the observed content), $\sigma_{n_i}^2 = \sqrt{(n^i_{\mathrm{MC}})^2}$, and the latter is the uncertainty on the expected content of the cell due to finite Monte Carlo statistics, $\Delta n_i = n^i_{\mathrm{MC}}/K$, where $K = N_{\mathrm{MC}}/N_{\mathrm{DATA}}$. Then $\sigma_i^2(\alpha,\beta) = n^i_{\mathrm{MC}}\,(1+1/K)$, which reduces to $\sigma_i^2(\alpha,\beta) \equiv \sigma_{n_i}^2$ in the limit of infinite Monte Carlo statistics.

$\alpha$ and $\beta$ are the fit parameters to be obtained from the minimization, that directly represent the fraction of $D^+$ and $D_s^+$ in the data, while the fraction of $\Lambda_c$ is given by $(1-\alpha-\beta)$.

As mentioned, that of the $\chi^2$ minimization is not the only possible choice. For example, the minimization of a likelihood function could be performed instead. In that case, one minimizes

$$\mathcal{L} = \sum_i \log f(x^i, \lambda) \tag{4.7}$$

where $f(x,\lambda)$ is the probability density for the variable $x$, depending on the set of parameters $\lambda$. The probability is constructed as

$$P_i = \alpha\frac{n^i_{D^+}}{N_{D^+}} + \beta\frac{n^i_{D_s^+}}{N_{D_s^+}} + (1-\alpha-\beta)\frac{n^i_{\Lambda_c}}{N_{\Lambda_c}} \tag{4.8}$$

with the normalized distributions constructed as in the case of the $\chi^2$ function. Thus the problem of cell size in defining the probability is there as well.

This option was tried, and gave results compatible with that of the $\chi^2$ minimization for what concerns both the values of the parameters and the errors, but the $\chi^2$ technique was adopted because it allows an easier control of the behaviour of the fit.

### 4.5.4 Results of the fit

The best values for $\alpha$ and $\beta$, as well as the error on the parameters, are determined by a MINUIT [83] based minimization of the function 4.6. The way the function to be minimized is defined, automatically imposes that the sum of the $D^+$, $D_s^+$ and $\Lambda_c$ contributions be equal to the number of charm events observed.

As previously discussed, the fit has been performed for various choices of variables and cell sizes. The different choices were made aiming at a subdivision of the events in a configuration which maximised the difference between the three particles.

After a study of the various distributions, we decided to focus on the fit of the $2\times 2\times 2$ division for $l_{\text{decay}}$, $\theta_{\text{decay}}$ and $E_{\text{HAD}}$, and the $3\times 3$ division for $l_{\text{decay}}$ and $\theta_{\text{decay}}$. Then, many fits were tried just varying the edges of the cells. The resulting $\chi^2$ is always good: between 8 and 11 both for the $2\times 2\times 2$ fit, and the $3\times 3$ fit.

For the same cell division, we also computed the $\chi^2$'s resulting from a separate comparison with each of the three particles. The resulting $\chi^2$'s are much larger than the number of degrees of freedom. For example, typical $\chi^2$'s for one of the $2\times 2\times 2$ divisions tried are:

$$\chi^2_{D^+} = 28.2 \qquad \chi^2_{D_s^+} = 31.0 \qquad \chi^2_{\Lambda_c} = 51.1$$

This results evidentiates the sensitivity of the data to the different combinations of the three contributions.

Before giving the results of the fit for $\alpha$ and $\beta$, we shall note that the level of sensitivity obviously reflects on the size of the errors on the fitted parameter. However, small errors may also be artificially obtained because of a particular statistical fluctuation for some specific choice of the size of the cells.Therefore, we have also repeated the fits for relatively small variations of the cell size, and we have verified that the dispersion of the values of $\alpha$ and $\beta$ from the different fits was consistent with the size of the error.

As a final result we quote, both for the values of $\alpha$ and $\beta$, and for their errors, an average of the result of the various fits performed. The values obtained are:

$$\alpha = 0.47 \pm 0.11 \qquad \beta = 0.09 \pm 0.07$$

The parameters $\alpha$ and $\beta$ correspond to the fractions of $D^+$ and $D_s^+$ respectively. The fraction of $\Lambda_c$ is obtained requiring the sum of the fractions to be equal to 1, i.e. $f(\Lambda_c) \ = 1-\alpha-\beta = 0.44$. The error on $f(\Lambda_c)$ can then be obtained from the error on $\alpha$ and $\beta$ and the correlation between them. The correlation is computed for each fit by the MINUIT program, and is always relatively high. To have a different evaluation of the error on $f(\Lambda_c)$, without relying also for it on an average of errors and their correlation, we simply varied $f(\Lambda_c)$ around the central value of 0.44, and evaluated the new $\chi^2$. The error on $f(\Lambda_c)$ is then given by the variation which corresponds to $\Delta\chi^2 = 1$.

The final result is:

$$f(D^+) = (47 \pm 11)\% \qquad f(D_s^+) = (9 \pm 7)\% \qquad f(\Lambda_c) = (44 \pm 12)\%$$

The error obtained for $f(\Lambda_c)$ is of the same order of magnitude of those on $f(D^+)$ and $f(D_s^+)$.

### 4.5.5 Comparison with the E531 result

The best measurement presently available for the fractions of charmed hadrons produced in neutrino interactions comes from FNAL E531, which was discussed in section 1.4.2. We are now going to compare our results with those of E531. These were obtained from a sample of 121 charm decays, in which 57 neutral decays were included, thus E531 observed 64 decays of charged charmed hadrons. Our sample amounted to 167 charged charm events, i.e. about twice the E531 statistics, but in our case the fractions were determined on a statistical basis, while E531 could determine the type of charmed hadron produced event by event because it could reconstruct the hadron's invariant mass. Table 4.6 compares the result of our analysis with that of E531.

| | E531 | CHORUS fit |
|---|---|---|
| $D^+$ (%) | $61 \pm 10$ | $47 \pm 11$ |
| $D_s^+$ (%) | $9 \pm 6$ | $9 \pm 7$ |
| $\Lambda_c$ (%) | $30 \pm 11$ | $44 \pm 12$ |

TABLE 4.6 – Comparison of the fractions of charmed hadons obtained in this analysis with those coming from E531. The original fractions of E531 have been scaled to the number of charged decays in their sample, and the error is the symmetrization of the original one rescaled so that the relative error on the fraction remains unchanged.

A first look at table 4.6 shows that the values of the measured fractions are similar for the two experiments, and the errors are of the same size. However, before making any conclusion for this comparison, the following issues have to be taken into account:

the average neutrino energies of the two experiments were different (22 GeV for E531, 27 GeV for CHORUS);

on the CHORUS data the cuts $p_\mu < 30$ GeV and $E_{\text{HAD}} > 4$ GeV were applied;

the E531 data are corrected to take into account kinematic cuts, acceptances and efficiencies that differently affect the three charmed hadrons. Our data are not yet corrected for possible differences in efficiency on the three species, though they are likely not to be very large;

the errors from our fit are purely statistical. The main contribution to systematic uncertainties on $l_{\text{decay}}$ and $\theta_{\text{decay}}$ is expected to come from the parametrization of the production mechanisms, and, in our specific case, by the fact that quasielastic and diffractive production are not included in the simulation. An estimate of the systematics can be obtained considering that, as mentioned in section 4.2.1, we expect 6 events from diffractive production and 3 events from quasielastic production in our sample of charged charm events. Thus a systematic uncertainty corresponding to about ten events can be considered as an upper limit.

The above considerations limit the precision of the comparison, still, our conclusion is that our preliminary measurement is consistent with that of E531. This, together with the good agreement of the data with our simulation, increases the confidence in the quality of our data.

## 4.6 Outlook

The errors we have quoted on the charmed hadron fractions in section 4.5.4 are of the same order of magnitude of those obtained by E531.

Only 13% of the $1\mu$ located events has been used in this analysis, so that the statistics can be improved of a factor 8 completing the analysis of the available sample.

Moreover, the 30 GeV cut on muon momentum, introduced to reduce the scanning load in phase 1, is going to be released and new events are going to be located. CHORUS then expects an improvement of more than a factor 10 in statistics in the near future.

The analysis shows that the statistical sensitivity to the fractions is good, so that the expected increase in the statistics will allow a very significant improvement of the precision of this measurement.

The increased statistics will also allow to analyse more kinematic variables, and to fit simultaneously fractions and production mechanism, thus extending the study to other parameters of the neutrino charm physics.

Our Monte Carlo simulation is being improved too: work is in progress to include the quasielastic and diffractive production, and to include effects that could be significant, such as slow rescaling. Also the Monte Carlo statistics is going to be improved with a new huge production specific for charm studies, which is already forseen.

# Summary and conclusions

The CHORUS experiment, originally designed to study neutrino oscillations, is also suitable to study charm physics thanks to its target of 800 Kg of nuclear emusions, where all the electroweak decays of charmed particles can be directly identified. CHORUS was the first experiment to develope fully automtic scanning techniques, and has now the chance to become the first high statistics emulsion experiment in charm physics.

In fact, a new fast scanning techniqe has been developed, the netscan, which allows to study the complete topology of the decay in a fully automatic way, provided the vertex position is known. Once the vertex is located, all the track segments in a volume around it are picked up: about 10,000 segments per event are scanned. The very high scanning performance needed for this kind of analysis is provided by the Ultra Track Selector, a hardware video image processor interfaced to a CCD camera, that can perform the netscan of one event in about 10 minutes.

Currently, CHORUS has a sample of about 144,000 $\nu_\mu$ charged current interactions whose vertex has been located in emulsion. About 70,000 events have already been analyzed with netscan. The output of netscan, consisting in raw track segments, is passed through the reconstruction algorithms for background rejection and tracking, and at the end of this process on average 40 tracks per event are found.

Because of the background tracks still present in the event after this step, a selection for charm candidates has been developed, which uses the information on the impact parameter and basically relies on the target tracker measurement for the validation of the reconstructed vertices of the event. The purity of the selection is 63%, thus candidates are checked in manual scanning to validate the hypothesis of being charm decays, and to measure with high accuracy the parameters of tracks and vertices. So far, the selection has been applied to a sample of 27,000 netscan events, and after the eye check of the candidates, 533 charm decays were found.

The analysis described in this thesis uses the 167 charged decays contained in the sample, which are measured at manual scanning and have the complete information of the electronic detector. From this data we have extracted the fractions of charged charmed hadrons, $D^+$, $D_s^+$ and $\Lambda_c$, composing the data sample. The analysis was based on the difference in lifetimes of these three particles, which reflects in a different decay path. Also other characteristics of the charmed particles, such as the decay angle and the hadronic energy associated to their production, were taken into account.

The distributions of the same kinematic quantities are computed from a sample of Monte Carlo events, which separately reproduces the $D^+$, $D_s^+$ and $\Lambda_c$ production. The *shapes* of the simulated distributions are used to determine the composition of the corresponding distribution for the data by means of a $\chi^2$ minimization: this gives the combination of the separate $D^+$, $D_s^+$ and $\Lambda_c$ contributions that best fits the data.

The result of our analysis is

$$D^+ = (47 \pm 11)\% \qquad D_s^+ = (9 \pm 7)\% \qquad \Lambda_c = (44 \pm 12)\%$$

The determination of the fractions of charmed hadrons in which the $c$ quark fragments is important in view of the measurement of fundamental quantities of the charm physics such as $V_{cd}$, $m_c$, $\kappa$. In fact, even charm experiments that can only detect muonic decays need to take them from external measurements in order to unfold the charm production cross section from the dimuon cross section. The best existing measurement is due to FNAL E531, and comes from less than half of our current statistics but is done on an event by event basis since the invariant mass of the decaying hadron could be measured.

Our present result compares well to that of E531, and the statistical error have similar sizes. The result, therefore, proves the sensitivity of our data to the fractions of charmed hadrons produced in the $\nu$ interaction.

With the final CHORUS statistics, expected to become in one year more that a factor 10 larger, it will be possible to reduce drastically the statistical error, and to extend the analysis to other characteristics of the event. The refinement of the Monte Carlo simulation is also under way, with the inclusion of all the production mechanisms, and a huge production is forseen, then allowing to precisely evaluate the sources of systematic error.

Much work is in progress on other items too: the netscan is going on on currently located events, as well as the location of new samples of events, and we expect to terminate the scanning in a few months. The developement of new selections for charm events is also under way, aiming to reach a purity sufficient to avoid the manual check.

# Bibliography

[1] E. Fermi, Nuovo Cimento **11** (1934), 1–19.

[2] E. Fermi, Z. Phys. **88** (1934), 161–177.

[3] F. Reines and C.L. Cowan, Phys. Rev. **92** (1953), 830–831.

[4] G. Danby *et al.*, Phys. Rev. Lett. **9** (1962), 36–44.

[5] M.L. Perl *et al.*, Phys. Rev. Lett. **35** (1975), 1489–1492.

[6] K. Kodama *et al.*, Phys. Lett. **B 504** (2001), 218–224.

[7] S. Fukuda *et al.*, Phys. Rev. Lett. **86** (2001), 5651–5655.

[8] Q.R. Ahmad *et al.*, Phys. Rev. Lett. **87** (2001), 071301.

[9] W.K.H. Panofsky, in "14th International Conference on High Energy Physics", Vienna, 1968, pp. 23–29.

[10] M. Breidenbach *et al.*, Phys. Rev. Lett. **23** (1969), 935–939.

[11] E.D. Bloom *et al.*, Phys. Rev. Lett. **23** (1969), 930–934.

[12] M. Gell-Mann, Phys. Lett. **8** (1964), 214–215.

[13] G. Zweig, in "Developments in the quark theory of hadrons", D.B. Lichtenberg and S.P. Rosen eds., vol. 1, North Holland Publ. Co., Amsterdam, 1964, pp. 22–101.

[14] S.L. Glashow, Nucl. Phys. **22** (1961), 579–588.

[15] S. Weinberg, Phys. Rev. Lett. **19** (1967), 1264–1266.

[16] A. Salam and J.C. Ward, Phys. Lett. **13** (1964), 168–171.

[17] P.W. Higgs, Phys. Lett. **12** (1964), 132–133.

[18] P.W. Higgs, Phys. Rev. Lett. **13** (1964), 508–509.

[19] N. Cabibbo, Phys. Rev. Lett. **10** (1963), 531–532.

[20] M. Kobayashi and T. Maskawa, Prog. Theor. Phys. **49** (1973), 652–657.

[21] D.E. Groom *et al.*, Eur. Phys. J. **C15** (2000), 1–878.

[22] G. B. Gelmini and M. Roncadelli, Phys. Lett. **B99** (1981), 411.

[23] F.J. Yndurain, “Quantum chromodynamics: an introduction to the theory of quarks and gluons”, Springer, New York, 1983.

[24] G. Sterman *et al.*, Rev. Mod. Phys. **67** (1995), 157–248.

[25] D.J. Gross and F. Wilczek, Phys. Rev. **D8** (1973), 3633–3652.

[26] D.J. Gross and F. Wilczek, Phys. Rev. Lett. **30** (1973), 1343–1346.

[27] H.D. Politzer, Phys. Rev. Lett. **30** (1973), 1346–1349.

[28] R.P. Feynman, Phys. Rev. Lett. **23** (1969), 1415–1417.

[29] L. Maiani, Cambridge Monogr. Part. Phys. Nucl. Phys. Cosmol. **1** (1991), 278–349.

[30] J.D. Bjorken, Phys. Rev. **179** (1969), 1547–1553.

[31] Y.L. Dokshitzer, Sov. Phys. JETP **46** (1977), 641–653.

[32] V.N. Gribov and L.N. Lipatov, Sov. J. Nucl. Phys. **15** (1972), 438–450.

[33] V.N. Gribov and L.N. Lipatov, Sov. J. Nucl. Phys. **15** (1972), 675–684.

[34] G. Altarelli and G. Parisi, Nucl. Phys. **B126** (1977), 298.

[35] H.L. Lai *et al.*, Eur. Phys. J. **C12** (2000), 375–392.

[36] M. Gluck, E. Reya and A. Vogt, Z. Phys. **C67** (1995), 433–448.

[37] M. Gluck, E. Reya and A. Vogt, Eur. Phys. J. **C5** (1998), 461–470.

[38] R.M. Barnett, Phys. Rev. Lett. **36** (1976), 1163–1166.

[39] R.M. Barnett, Phys. Rev. **D14** (1976), 70.

[40] P. Astier *et al.*, Phys. Lett. **B486** (2000), 35–48.

[41] N. Ushida *et al.*, Phys. Lett. **B206** (1988), 375.

[42] B. Andersson, G. Gustafson and B. Soderberg, Z. Phys. **C20** (1983), 317.

[43] C. Peterson, D. Schlatter, I. Schmitt and P.M. Zerwas, Phys. Rev. **D27** (1983), 105.

[44] P. Vilain *et al.*, Eur. Phys. J. **C11** (1999), 19–34.

[45] S.A. Rabinowitz *et al.*, Phys. Rev. Lett. **70** (1993), 134–137.

[46] M. Aguilar-Benitez *et al.*, Phys. Lett. **B135** (1984), 237.

[47] T. Bolton, hep-ex/9708014, 1997.

[48] M.K. Gaillard, S.A. Jackson and D.V. Nanopoulos, Nucl. Phys. **B102** (1976), 326.

[49] M.K. Gaillard and C.A. Piketty, Phys. Lett. **B68** (1977), 267.

[50] O. Melzer, Ph.D. thesis, Universiteit van Amsterdam, The Nederlands, 2001.

[51] A.E. Asratyan *et al.*, Z. Phys. **C58** (1993), 55.

[52] T. Adams *et al.*, Phys. Rev. **D61** (2000), 092001.

[53] P. Annis *et al.*, Phys. Lett. **B435** (1998), 458–464.

[54] H. Abramowicz *et al.*, Z. Phys. **C15** (1982), 19.

[55] A.O. Bazarko *et al.*, Z. Phys. **C65** (1995), 189–198.

[56] E. Eskut *et al.*, Nucl. Instr. and Meth. **A 401** (1997), 7.

[57] G. Acquistapace *et al.*, CERN-ECP-95-014.

[58] S. Peraire, M. Ross and J.M. Zazula, Talk given at 5th European Particle Accelerator Conference (EPAC 96), Sitges, Spain, June 10-14, 1996.

[59] B. Van de Vyver and P. Zucchelli, Nucl. Instr. and Meth. **A385** (1997), 91–99.

[60] P. Lendermann *et al.*, Nucl. Instr. and Meth. **A344** (1994), 143–148.

[61] P. Annis *et al.*, Nucl. Instr. and Meth. **A367** (1995), 367–371.

[62] P. Annis *et al.*, Nucl. Instr. and Meth. **A412** (1998), 19–37.

[63] F. Bergsma *et al.*, Nucl. Instr. and Meth. **A 357** (1995), 243–248.

[64] J.W.E. Uiterwijk *et al.*, Nucl. Instr. and Meth. **A409** (1998), 682–686.

[65] S. Buontempo *et al.*, Nucl. Instr. and Meth. **A 349** (1994).

[66] D. Acosta *et al.*, Nucl. Instr. and Meth. **A308** (1991), 481–508.

[67] E. Di Capua *et al.*, Nucl. Instr. and Meth. **A 378** (1996), 221–232.

[68] M. G. van Beuzekom *et al.*, Nucl. Instr. and Meth. **A427** (1999), 587–606.

[69] M. vander Donckt, Ph.D. thesis, Université Libre de Bruxelles, Belgium, 1999.

[70] A. Artamonov and P. Gorbounov, CERN-PPE/97-029, 1998.

[71] T. Nakano, Ph.D. thesis, University of Nagoya, Japan, 1997.

[72] A.M. Güler, Ph.D. thesis, Middle East Technical University, Ankara, Turkey, 2000.

[73] P. Zucchelli, Ph.D. thesis, Università degli Studi di Ferrara, Italy, 1994.

[74] G. Ingelman *et al.*, DESY 96-057, 1996.

[75] T. Sjøstrand, Comput. Phys. Commun. **82** (1995), 74–89.

[76] T. Sjøstrand, CERN-TH-7112-93 (1993).

[77] S. Sorrentino, CERN-PPE/98-005, 1998.

[78] S. Sorrentino, Ph.D. thesis, Università di Napoli “Federico II”, Italy, 1998.

[79] Application Software Group, CERN Program Library Long Writeups W5013, 1993.

[80] E. Eskut *et al.*, Phys. Lett. **B497** (2001), 8–22.

[81] F. Cassol, CERN-PPE/98-002, 1998.

[82] N. Armenise *et al.*, CERN Geneva - CERN-SPSC-90-42 (90/12,rec.Feb.91) 65 p.

[83] F. James and M. Roos, Comput. Phys. Commun. **10** (1975), 343–367.

# Acknowledgements

Desidero ringraziare per primo il mio relatore, professor Pier Ferruccio Loverre, che con grande competenza, attenzione, pazienza, mi ha supportato (e sopportato) durante svolgimento di questo lavoro.

I wish to thank the helpfulness of all the CHORUS collaborators, ed in particolare di quelli del gruppo di Roma, in compagnia dei quali è stato un piacere lavorare;

I am also grateful to prof. Kimio Niwa, for welcoming me to his laboratory in Nagoya University, and many thanks go to all the members of the F-Ken for their kindness and hospitality. In particular, my acknowledgements to Koichi Kodama, Masahiro Komatsu, Kouji Narita and Osamu Sato, whose patient explanations and suggestions were precious.

Also priceless was the help of Murat Güler, who has never failed to answer at length to my questions, even if it was night (there...).

Un grazie di cuore a Bart Van De Vyver, per le mille volte in cui ha risposto alle mie disperate richieste di aiuto, spesso evitando di indirizzarmi i vari improperi che conosce in lingua italiana.

Ringrazio ovviamente i miei familiari ed amici (umani, felini e canini) per il loro costante appoggio, e perché a forza di chiedermi “ma quando finisci” (questo solo gli umani), mi hanno davvero spronato a farlo il prima possibile...

In particolare, nel settore umani, tutta la mia gratitudine e il mio amore vanno a Gerardo Morsella, grazie al quale tutto è più facile, e più divertente.

Un saluto a Penni, panteretta pantofolaia, che ora va scorrazzando in un mare di erba gatta.